POLITECNICO
MILANO 1863

SCUOLA DI INGEGNERIA INDUSTRIALE
E DELL'INFORMAZIONE

Lumped-parameter models for the simulation of cardiovascular congenital diseases

Tesi di Laurea Magistrale in
Aeronautical Engineering - Ingegneria Aeronautica

Author: **Giulio Valenti**

Student ID: 976842
Advisor: Prof. Luca Dedè
Co-advisors: Andrea Tonini; Paolo Ferrero, MD; Prof. Alfio Quarteroni
Academic Year: 2022-23

Abstract

The objective of this study is to investigate some congenital heart defects by modeling them through a 0D lumped-parameters model. The starting reference model corresponds to a healthy adult male. The considered defects are the patent foramen ovale, partial anomalous pulmonary venous return, atrial septal defect and ventricular septal defect. The foramen is implemented by using a valve model based on the Bernoulli formula. The resulting model is tested for various foramen radius to quantify the different impact it has on the cardiac circulation. The model predicts a decrease in the ratio between pulmonary and systemic flow for increasing defect size. To model partial anomalous pulmonary venous return, the pulmonary venous compartment is first divided into the four main pulmonary veins. Subsequently, these veins are detached from the left atrium and connected, in one case, to the atrium and, in the other case, to the superior vena cava. In both cases, the number of anomalous veins is progressively increased from zero to three. The model predicts an increased impact on cardiac circulation for an increasing number of anomalous veins. Furthermore, by comparing the two cases, the model predicts a lower impact in the superior vena cava, resulting in a reduced amount of already oxygenated blood erroneously returning to the pulmonary circulation. Finally, the two septal defects are modeled as resistances connecting the respective cardiac chambers. A model calibration involving septal defects is performed for three different clinical data sets. The calibration shows how various parameters representing the physical characteristics of the cardiocirculatory system are changed due to the alteration in blood circulation patterns over the years. In particular, an increase in pulmonary resistances and a decrease in the arterial pulmonary capacitance is observed in two patients with ventricular septal defect.

Keywords: Heart congenital defects, Lumped-parameter model, Patent foramen ovale, Partial anomalous pulmonary venous return, Atrial septal defect, Ventricular septal defect

Abstract in lingua italiana

L'obiettivo di questa trattazione è quello di studiare alcuni difetti congeniti del cuore, inserendili in un modello 0D a parametri-concentrati. Il modello di riferimento di partenza corrisponde ad un uomo adulto sano. I difetti considerati sono il forame ovale pervio, il ritorno venoso anomalo polmonare parziale, il difetto di setto interatriale e il difetto di setto interventricolare. Il forame viene implementato utilizzando un modello di valvola basato sulla formula di Bernoulli. Il modello risultante viene provato per diversi valori di raggio del forame per quantificare il diverso impatto che questo può comportare sulla circolazione cardiaca. I risultati mostrano una diminuzione del rapporto tra il flusso polmonare e il flusso sistemico incrementando le dimensioni del difetto. Per modelizzare il ritorno venoso anomalo polmonare parziale viene prima diviso il compartimento venoso polmonare nelle quattro principali vene polmonari. Successivamente queste vengono staccate dall'atrio sinsitro e collegate in un caso nell'atrio e nell'altro alla vena superiore cava. Per entrambi questi casi si aumenta progressivamente il numero di vene anomale da zero a tre. Per entrambi i casi di collegamento anomalo, a fronte di un aumento nel numero di vene anomale il modello prevede un incremento dell'impatto sulla circolazione cardiaca. Inoltre, confrontando i due casi, il modello prevede un minore impatto per collegamento alla vena superiore vena cava, quindi una ridotta quantità di sangue già ossigenato che erroneamente ritorna nella circolazione polmonare. Infine i due difetti di setto vengono modellati come due resistenze che collegano le rispettive camere cardiache. Una calibrazione del modello comprendente i difetti di setto è eseguita per tre diversi set di dati clinici. La calibrazione mostra come diversi parametri, rappresentanti le caratteristiche fisiche del sistema cardiocircolatorio, siano cambiate a causa dell'alterazione nella circolazione sanguigna a cui questo sistema è sottoposto nel corso degli anni.
In particolare si nota un aumento delle resistenze polmonari e una diminuzione della capacità dell'arteria polmonare in due pazienti che presentano il difetto di setto interventricolare.

Parole chiave: Difetti congeniti cuore, Modello parametri-concentrati, Forame ovale pervio, Ritorno venoso anomalo polmonare parziale, Difetto setto interatriale, Difetto setto interventricolare

Contents

Introduction

Congenital heart defects represent a category that includes numerous diseases that vary widely from each other. Even when considering a single specific disease within this category, its impact on the body can vary significantly. The human body is extremely complex, no individual is equal to anyone else in the world and there are a multitude of factors that influence the body structure and development. The body adapt in response to abnormal factors and tries to cope with it by restructuring itself, thus increasing the absolute uniqueness of every patient.

Tools that give doctors a clearer picture of the patient-specific situation and that can glimpse/predict how the body will respond to a medication treatment/surgery can greatly support the decisions making and final outcome for the patient. In this study a few congenital heart defects, namely the atrial and ventricular septal defects, the patent foramen ovale and the partial anomalous pulmonary venous return have been studied.

Starting from how they generally impact the body anatomy and physiology, we look for ways to model and implemented them in a 0D lumped-parameter model. The goal is to modify the base lumped-parameter model for a normal healthy male adult, introducing one at a time the studied congenital defects and observing whether the resulting model exhibits behaviors consistent with those of patients carrying that specific defect.

For all the considered defects we started from a 0D lumped-parameters model inspired by [1–3].

Studying the patent foramen ovale we used a Bernoulli valve model [4, 5] to simulate the foramen. This customized model correctly predicts a shunt phenomenon increase for larger foramen radius. In addition, it estimates a considerably small impact on the cardiocirculatory system.

For the modeling of the partial anomalous pulmonary venous return we start by first splitting the pulmonary venous system of the healthy reference model. Then, we reshape the lumped-parameter model by severing the resulting pulmonary veins from the left atrium and connecting them to the right atrium or its tributaries. We simulate two types of this disease, the first one in which the anomalous veins drain in the right atrium and the second one in which the anomalous pulmonary veins drain in the superior vena cava.

Superior vena cava lumped-parameters has been taken from [6, 7].
We increase the number of pulmonary veins from one to three in both types, the model correctly predict an increased impact on the cardiac circulation for more anomalous veins. The model also correctly predict a lower impact for the superior vena cava case with respect to the atrium case, in according with the pathological history of this disease.
Lastly, we introduce the ventricular and septal defects in the model as two resistances connecting the respective heart chambers as in [8–11].
Subsequently, we perform a model calibration on the resulting lumped-parameter model for three different septa defects patients, whom clinical data are provided by Dott. Paolo Ferrero (IRCCS Policlinico San Donato Hospital, Italy).
The first patient present an atrial septal defect, the second one is affected by a ventricular septal defect and its clinical data is measured in normal conditions and under vasodilatators administration. Finally the third one presents both septal defects.
The calibrated models successfully predicts almost all the available clinical data, the relative mean squared errors computed on these quantities are considerably small.
Different considerations and inquiring on the patients clinical conditions are made. In particular, in the two patients affected by the ventricular septal defect, the resulting pulmonary resistances are particularly high and the pulmonary arterial capacitance is significantly small.

1 | Anatomy and physiology

In this first chapter we review the anatomy and physiology of the heart and its congenital defects considered in this study.

1.1. Heart

The heart is an organ located between the lungs which function is to pump blood throughout the body. It contains four muscle chambers, atria and ventricles, stimulated by electrical impulses. Their contraction phase is called systole, the relaxation that follows dyastole. Right atrium and ventricle are usually collectively referred to as the right heart. In the same fashion their left counterparts are called left heart.
Left and right atria are positioned on the upper side of the heart and receive blood from the pulmonary and systemic veins, respectively. As the atria contract, the blood flows into the respective ventricle where it is pumped to the arteries.

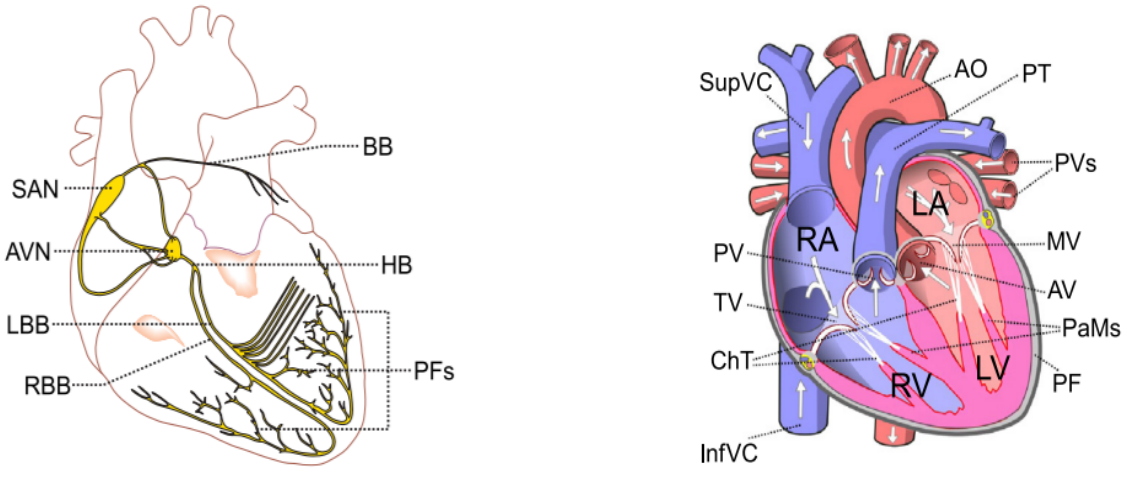

(a) (b)

Figure 1.1: Cardiac anatomy: (a) a sketch of its eletrical network system (picture elaborated from [12]); (b) a sketch of the heart internal structure along with its main components (picture elaborated from [13]). All abbreviations are defined in table 1.1

Table 1.1: List of abbreviations.

Cardiac anatomy		RBB	Right Bundle Branch
AO	Aorta	RV	Right Ventricle
AV	Aortic Valve	SAN	SinoAtrialNode
AVN	AtrioVentricular Node	SupVC	Superior Vena Cava
BB	Bachmann's Bundle	TV	Tricuspid Valve
HB	His Bundle		
InfVC	Inferior Vena Cava	**Cardiac cycle**	
LA	Left Atrium	AC	Atrial Contraction
LV	Left Ventricle	EDV	End Diastolic Volume
MV	Mitral Valve	ESV	End Systolic Volume
PF	Pericardial Fluid	IVC	IsoVolumetric Contraction
PT	Pulmonary Trunk	IVR	IsoVolumetric Relaxation
PV	Pulmonary Valve	SV	Stroke Volume
PVs	Pulmonary Veins	VE	Ventricular Ejection
RA	Right Atrium	VPF	Ventricular Passive Filling

Atria and ventricles contraction is regolated by the electrical conduction system sketched in Figure 1.1 (a). The electrical stimulation arises in the SinoAtrial Node (SAN), a special cardiac muscle region in the upper back wall of the Right Atrium (RA) near the Superior Vena Cava (SVC), from there the signal is immediately directed to the Left Atrium (LA) through different inter-atrial links like the Bachmann's Bundle (BB) to ensure an almost simultaneous atrial contraction.
Electrical transmission is also present from the SinoAtrial Node to the Atrio Ventricular Node (AVN) where it is holded till the end of the atrial contraction. Then, the impulse reaches the His Bundle (HB) and it splits between the Left Bundle Branch (LBB) and the Right Bundle Branch (RBB) to stimulate both ventricles.
Atria and ventricles are separated by a high density fibrous section called the Cardiac Skeleton (CK), it acts as an insulator between the upper and lower chamber to ensure that atrial and ventricular contractions happen in two distinct timeframes.

Into the fibrous rings of the Cardiac Skeleton there are 4 cardiac valves made of strong fibrous tissue that regulate the blood movement. The valves have thin but strong flaps called leaflets or cusps that can open when subjected to a pressure gradient or close to prevent backflow. Together with the other components depicted into the Figure 1.1 (b)

they facilitate the cyclic circulation of blood throughout the body.
The blood circulating in the body returns to the right atrium through the Inferior and Superior Vena Cava (InfVC, SupVC). Subsequently to the opening of the Tricuspid Valve (TV) the blood flows from the right atrium to the right ventricle.
When the ventricular contraction starts, the blood pressure in the right ventricle rise. This pressure increase opens the pulmonary valve (PV) and push the blood into the Pulmonary Trunk (PT). From there, the blood is carried through the pulmonary arteries to the lungs.
The flow that passes through the lungs, known as pulmonary circulation, undergoes an exchange in the capillaries surrounding the alveoli. Oxygen from the inhaled air diffuses through the thin capillary walls into the blood, while carbon dioxide from the blood diffuses into the alveoli to be exhaled. Subsequently, through the pulmonary veins (PVs), it returns to the left atrium (LA).
The oxygen replenished blood descends from the left atrium to the left ventricle (LV) through the Mitral Valve (MT) and then pumped into the Aorta (AO) through the Aortic Valve (AV).
From the aorta, the blood branches out into extensive vascular networks, coursing through the entire body where its oxygen content is utilized. This portion of the cardiovascular system that is responsible for delivering oxygenated blood from the heart to the body's tissues and returning deoxygenated blood back to the heart is called systemic circulation. Finally the systemic circulation venous system returns the blood to the right atrium, closing the loop.

The cyclic nature of the blood circulation needs the precise and controlled pumping and relaxation of the heart's four chambers. Initially, during the IsoVolumetric Relaxation (IVR) phase, the ventricular muscles relax following the contraction phase of the previous heartbeat. While all valves are closed, the ventricular volume is constant and the pressure decreases rapidly. When atrial pressures match the ventricular ones the opening of the atrioventricular valves (TV and MV) is triggered. This marks the beginning of the Ventricular Passive Filling (VPF) phase.
Subsequently, atrial systole starts, stimulated by the SinoAtrial Node. Atrial contraction (AC) propels additional blood towards the ventricles, giving them added preload, also known as 'atrial kick'.

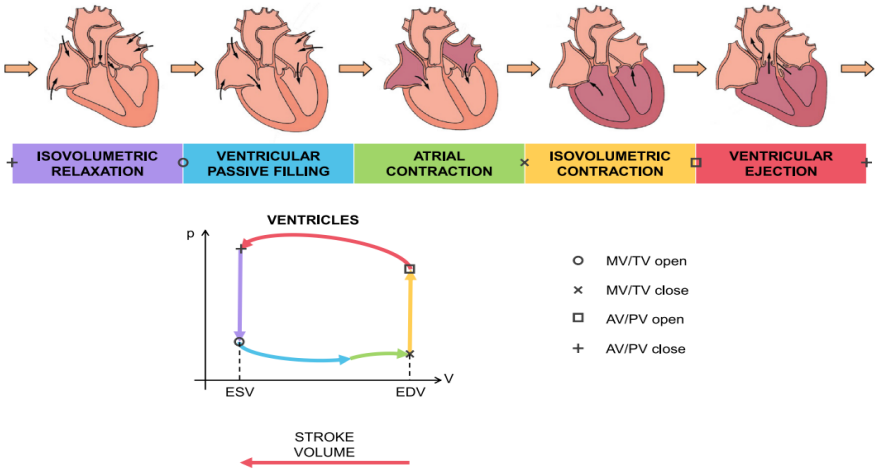

Figure 1.2: Cardiac cycle phases: on the top, a sketch of the blood flow direction, the valve status and the contraction of the 4 chambers (darker in color) throughout the different phases (pictures elaborated from [14]); on the bottom, the ventricular pressure-volume loops and the valves status legenda.

As said before the Atrio Ventricular Node regulates the electrical signal, allowing ventricular contraction only after the end of the atrial one. Upon ventricular contraction, pressure rises quickly, matching atrial pressure and closing the atrioventricular valves. Subsequently, ventricles contract, but all the cardiac valves are closed, therefore the volume is constant. This phase is called IsoVolumetric Contraction (IVC). Ventricles pressures quickly rise and exceed the respective arterial ones, causing the semilunar valves (PV and AV) opening and consequently the blood discharge through the arterias, namely the Ventricular Ejection (VE) phase (Figure 1.2).
During ventricular ejection, the volumes of the lower chambers diminish, consequently bringing the cardiac skeleton and the atrioventricular plane downward. Simultaneously, the atria fill, passively dilating in response to this downward motion. The atria filling capabilities are, in fact, highly related to the ventricles' distensibility.
Pressure-volume loops are historically used to visualize (and measure) the work done by a system. The typical pressure-volume loop of the ventricles is reported in the Figure 1.2 on the bottom, its squared configuration directly reflects the status of the valves and the two isovolumetric phases described above. As pointed out in the pressure-volume diagram the difference between the ventricular End Diastolic Volume (EDV) and End Systolic Volume (ESV) is the blood volume pumped out from each ventricle during a heartbeat, this quantity is called Stroke Volume (SV).
In this study, several congenital heart defects are introduced. These anomalies disrupt normal circulation, leading to abnormal blood flow. Such irregular movements, arising from an anatomical irregularity in the patient, are referred to as blood shunts.

Atria are separated by a wall called interatrial septum. Ventricles in the same fashion are divided by the interventricular septum; this partitioning is key to ensure the correct blood circulation.

The anatomy of these two septa is briefly reported to give a better foundation on the congenital defects discussed later on.

Interatrial septum starts to form on the first weeks of fetal development, when a strip of tissue called septum primum begins to grow downward from the upper ceiling of the atria (Figure 1.3.A). Initially this strip doesn't fill all the space between the two chambers (Figure 1.3.B), leaving an orifice called ostium primum (i.e. first opening). Septum primum continues to descend towards the endocardial cushions (part of the atrioventricular plane) but before reaching it, the tissue reopens in its uppers part forming another gap (Figure 1.3.C) called ostium secundum (i.e. second opening).

Subsequently, a second tissue called septum secundum begins to grow adjacent to the septum primum, covering the ostium secundum and leaving a small opening called the foramen ovale (Figure 1.3.D). This opening, that should close by itself the first year of life (Figure 1.3.E), often persists into adulthood, this condition is called patent foramen ovale (Figure 1.3.F) and will be discussed in the next section.

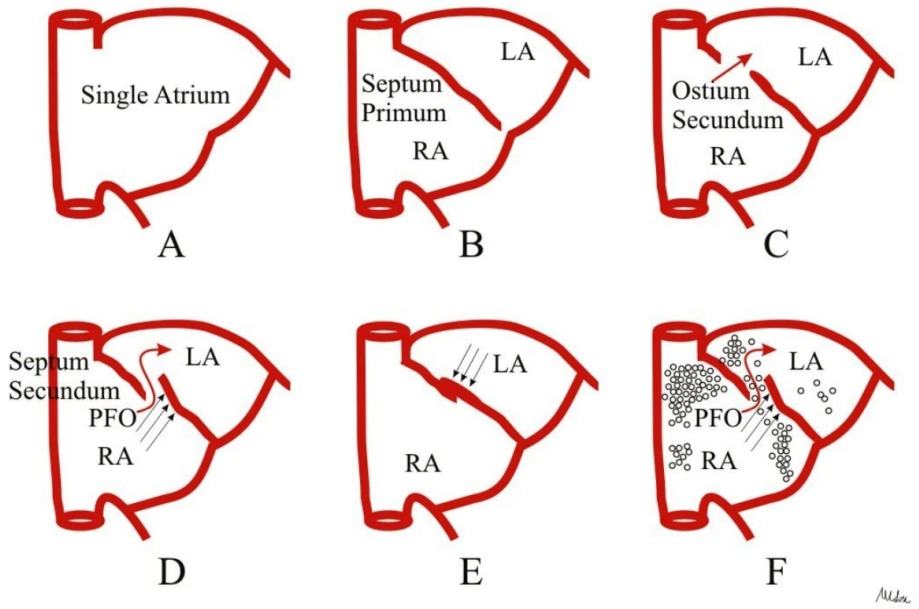

Figure 1.3: Interatrial septal development (A-E) and PFO condition (F), image taken from [15].

The interventricular septum, on the other hand, is a triangular wall of cardiac tissue composed by a muscular portion and a membranous portion (Figure 1.4). The muscular portion is the predominant one, it is thick and located in the lower part, near the apex of the heart. It can be further subdivided into three components: the inlet septum, trabecular septum, and infundibular septum.
The membranous part, however, is located near the base of the heart, or in other words, in the upper part of the interventricular septum.

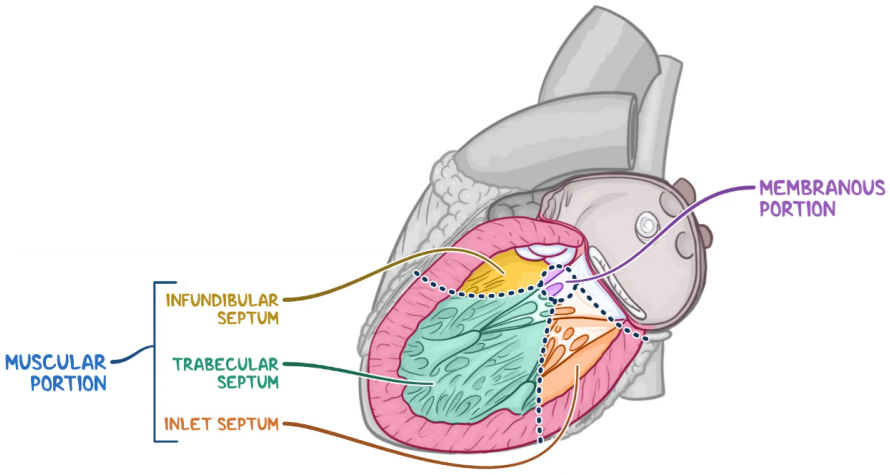

Figure 1.4: Interventricular septum anatomy (image taken from [16]).

1.2. Patent foramen ovale

Patent foramen ovale (PFO) is the most common congenital heart anomaly of fetal origin, present in one-quarter of the entire adult population.
The foramen ovale is a small flap-like opening in the fetus inter-atrial wall necessary to direct blood flow directly from the right to the left atrium, bypassing the pulmonary circulation. Indeed, lungs will not work till birth . The nutrients and the oxygen needed for the fetus development are provided by the mom's blood through the placenta.
Once the pulmonary circulation increases after birth, left atrium expands and its pressure increases because of the additional oxygenated blood flow received from the lungs. This increase in the left atrium pressure pushes the overhanging part of the septum primum against the septum secundum stimulating the fusion.
Often the fusion is incomplete, as a result the orifice is not sealed and the septum primum is still free to partially hang.
Given its shape it can only open into the left atrium when the pressure in the right atrium exceeds the left one, otherwise the septum primum would just press into the septum secundum closing the opening. The blood shunt, which is then mainly right to left, can be sometimes inverse due to ventricular dilatation. The foramen tissues are stretched mechanically by the dilatation, making the foramen orifice open. Now that the hole allows fluid leakage, in presence of adverse pressure gradient the blood moves from the left atrium to the right one resulting in a right to left shunt; this phenomenon is called regurgitation. Any condition that can make the right atrium pressure exceed the left one opens the foramen allowing blood leakage. Some examples of these conditions are pulmonary diseases such as pulmonary hypertension [17] or chronic obstructive pulmonary disease [18], use of positive end-expiratory pressure [19], pulmonary embolism after stroke [17], congestive heart failure [20] , onset of stroke after a Valsalva maneuver [21] and pulmonary stenosis [20].

Association between PFO and cryptogenic stroke, a condition characterized by strokes of unknown origin, has been demonstrated in young adults. (<55 years) [22].
PFO has also been described as one of the main facilitator for Paradoxical Embolism (PDE) [23]. The embolus generates in the systemic circulation, generally in the lower body, and travels back to the right heart. Normally it should be filtered by the lungs, but, in presence of a intra-cardiac shunt, it bypass the pulmonary circulation (Figure 1.5) and gets pushed from the right ventricle into the systemic circulation, causing arterial occlusion.

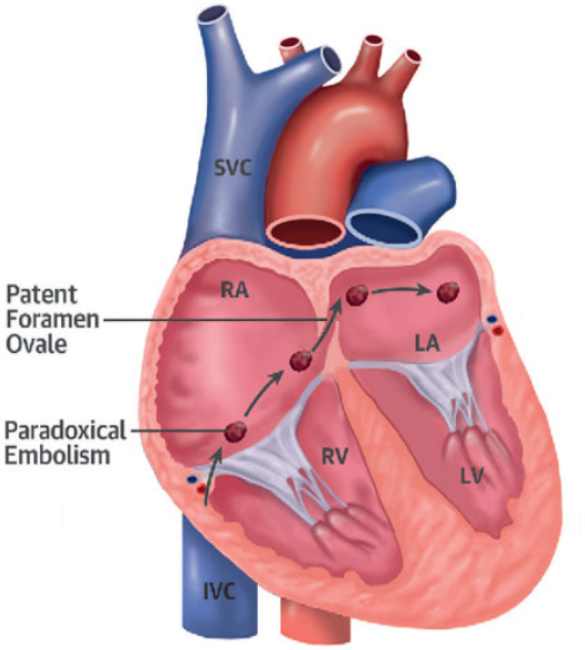

Figure 1.5: Paradoxical embolus passage through a patent foramen ovale (image elaborated from [24]).

1.3. Partial anomalous pulmonary venous return

Partial anomalous pulmonary venous return (PAPVR) is an uncommon congenital defect in which some, but not all, of the pulmonary veins are partially or completely connected to the right atrium or one of its venous tributaries.
The pulmonary veins originate from individual alveoli within the lungs as capillary vessels, from there after a complex merging network they combine into 4 main pulmonary veins, 2 from each lung, that normally discharge into the the left atrium.
The most frequent connection spots other than the right atrium are superior/inferior vena cava (Figure 1.6), innominate veins, brachiocephalic veins and azygos vein.
The pulmonary wedge pressure, from where the pulmonary veins arise, is usually higher than the right atrium (and its tributaries) one. Oxygenated blood is thus moved to the right heart and pumped again into the pulmonary circulation, the shunt is left to right.
PAPVR is highly variable depending on the number of anomalous veins, the type of connection (partial or complete drain) and the discharge site. By moving upwards through the systemic venous system the pressure is naturally higher. It results that the further from the right atrium is the attachment site the lower will be the pressure gradient between the lungs and the attachment spot itself, resulting in a shunt amount decrease.

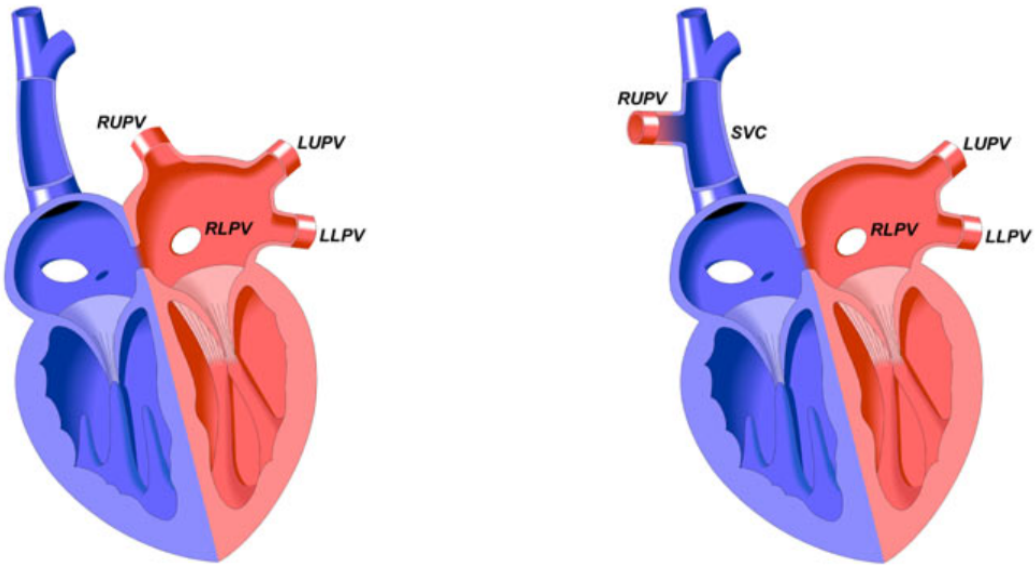

(a) (b)

Figure 1.6: Anomalous pulmonary vein example: (a) RUPV normally drains into the left atrium ; (b) RUPV completely drains into SVC. (picture elaborated from [25]). Legend defined in table 1.2.

Table 1.2: Venous system legend

SVC	Superior Vena Cava
RUPV	Right Upper Pulmonary Vein
RLPV	Right lower Pulmonary Vein
LUPV	Left Upper Pulmonary Vein
LLPV	Left Lower Pulmonary Vein

There is a classification of the anomalous pulmonary venous return according to the site of abnormal connection, Figure 1.7. For the sake of simplicity, in this study only two cases of supradiaphragmatic connections will be covered: the superior vena cava one (Figure 1.6.b) and the cardiac one (in particular directly into the right atrium).

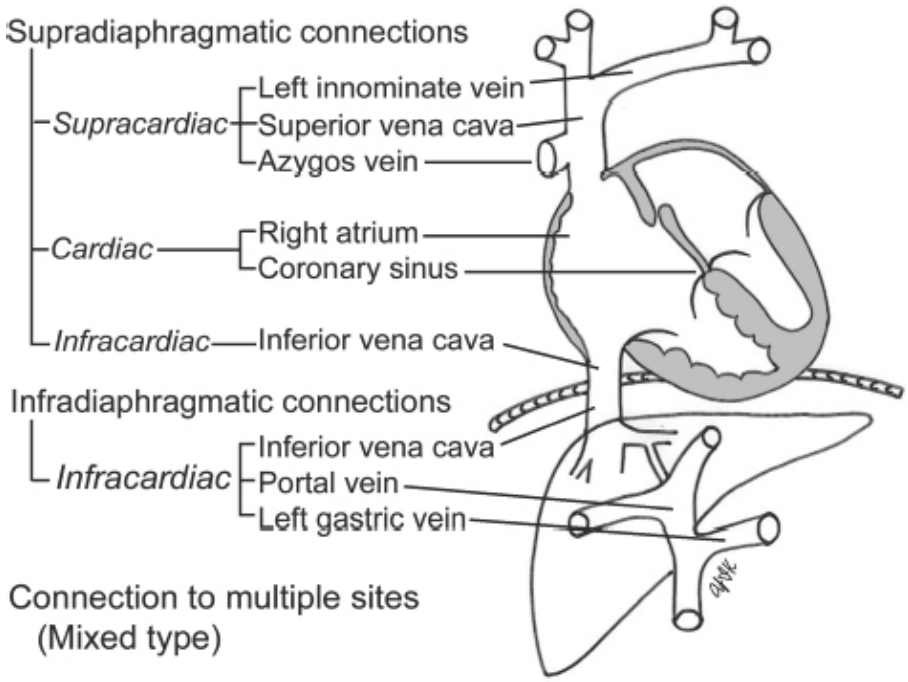

Figure 1.7: Partial anomalous pulmonary venous return classification (image taken from [26]).

1.4. Atrial septal defect

The atrial septal defect (ASD) is a congenital heart defect that occurs when the wall separating the two heart's upper chambers (atria) fail to close, resulting in a communicating orifice (Figure 1.8).
This hole allows an abnormal shunt, meaning an anomalous leak that shouldn't be happening. The defect can usually close by itself or, frequently, be found in early stages of life; sometimes though, it can go unnoticed leading to further problems and complications.
Depending on the size, the ASD can cause mild shortness of breath, palpitations and arrhythmia, pulmonary hypertension (PH) and even right-heart failure.
The blood, pushed by the pressure gradient between the two atria, can move through the hole. Usually left atrium pressure is higher leading to left-to-right shunt and consequently to right-heart, pulmonary circulation overload. The excessive amount of already oxygenated blood (coming from the left atrium) gets re-pumped into the pulmonary arteria, resulting in vessels hypertension and consequently triggering body adaptation. The pulmonary vessels thicken and narrow leading to an increase in the pulmonary vascular resistance.
Most of the times the defect can be closed by open-heart surgery or through catheterization. However, severe pulmonary hypertension and increased pulmonary resistance can make the procedure futile and even harmful. Association between high pulmonary resistance and post ASD-closure surgery deaths has been found [27].

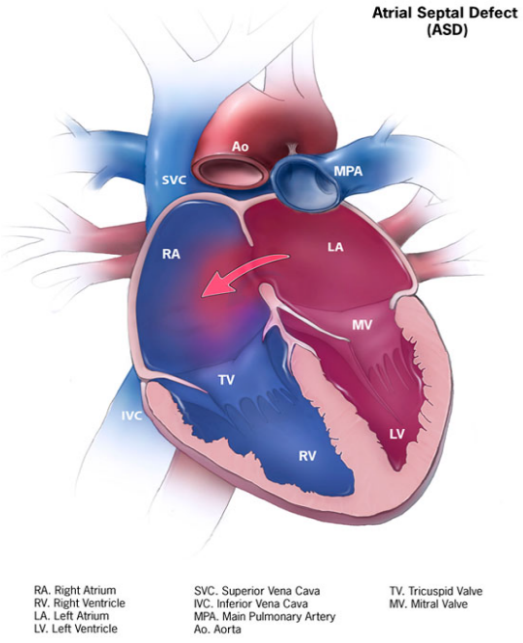

Figure 1.8: Atrial septal defect (picture taken from [28]).

1.5. Ventricular septal defect

The ventricular septal defect (VSD) is the most common congenital cardiac anomaly in children and second only to tricuspid aortic valves in adults. This defect is characterized by a hole in the wall (septum) that divide the ventricles.
The hole usually by itself without external help, occasionally it persists and lead to further problems.
Blood flows through the hole pushed by the pressure gradient between the two ventricles. The harm entity depends directly on its size. The opening ranges from being really small to cover the entire wall separating the ventricles, in this latter case the two lower chamber essentially work as a one common ventricle. Thus, symptoms and complications span from shortness of breath (expecially when exercising), hard breathing, frequent respiratory infections to aortic insufficiency, delayed growth and even to heart failure.
The shunted portion of blood is pushed by the ventricular contraction into the wrong circulation, either the pulmonary or the systemic one. Depending on the shunt direction one of two circulation gets less blood than it is supposed to, whereas the other one is overloaded, resulting in a structural strain.
Based on data collected from patients with a ventricular defect over the years, it was observed that this overload on the pulmonary circulation leads to pulmonary hypertension, triggering body's adaptation in an attempt to rebalance the flow quantities between the pulmonary and systemic circulations. The damages caused by the excessive amount of blood reaching the pulmonary artery and subsequent vessels result in injuries, inducing a proliferation of wall vascular cells such as smooth muscle cells, endothelial cells, fibroblasts, etc. This remodeling results in a thickening of the vessels, effectively increasing pulmonary vascular resistance [29].
Even though they affect the heart in the same way, there are different types of ventricular septal defects (Figure 1.9), including conoventricular VSD (a hole where portions of the ventricular septum should meet under the semilunar valves); perimembranous VSD (a hole in the upper ventricular septum); inlet VSD (a hole in the septum where blood enters the ventricles through the atrioventricular valves); and muscular VSD (a hole in the lower muscular portion of the septum), which is the most common of the four.

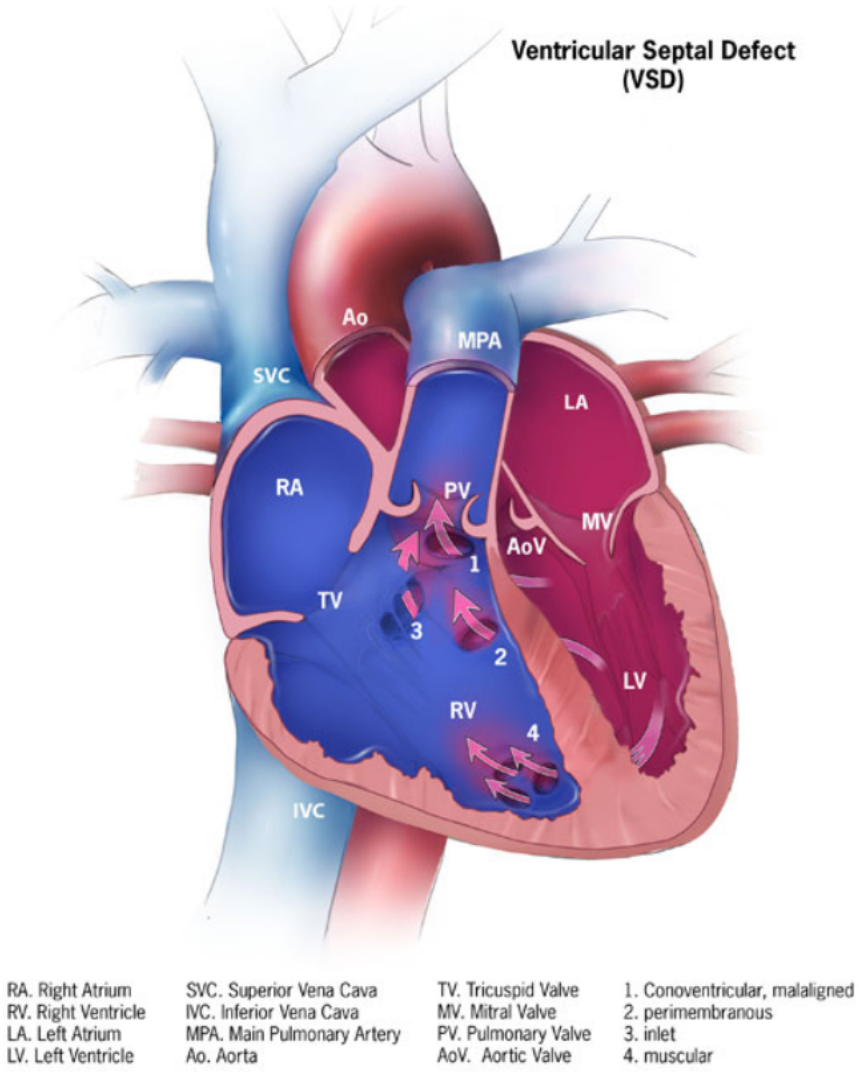

Figure 1.9: Ventricular septal defect classification (picture taken from ([30]).

2 | Mathematical Models and Numerical Methods

We present in this chapter the mathematical models used in this study. Firstly, we review the lumped-parameter model (section 2.1) used to simulate the cardiac circulation and subsequently modified to account for the different congenital heart defects.
These disease-customized models are addressed using different methods.
For the defects for which we had real patient data available for this condition, we performed a calibration with the L-BFGS-B algorithm (Section 2.4) aimed to minimize a loss function based on the available clinical data. Throughout the calibration process, our approach was enhanced by employing Sobol' indices (section 2.5) to pinpoint parameters affecting significantly available patient data and allowing L-BFGS-B to vary only the identified parameters.
Minimization of the loss function requires the resolution of the model ODEs system, this was made by approximating its solution using the Dormand-Prince method (Section 2.2),
.
For the other considered congenital defects, the ode15s solver from MATLAB is employed. This solver implements a method based on the Backward Differentiation Formula (BDF).(Section 2.3).

2.1. Lumped-parameter mathematical model

The cardiovascular circulatory system was simulated through a zero dimensional (0D) mathematical model that exploits the similarities between blood vessels and an electrical circuit. Using this model it's possible to estimate important physiological data of the patient without using invasive measuring systems.

In this model the circulatory system components are split in different compartments characterized by lumped parameters that sums up the related physical quantities.

For the blood the current represents its flow rate and the electrical potential its pressure. For the vessels the electric resistance is used to simulate the viscous resistance of blood flow and the resistance of vessel wall; the capacitance reflects the vessel compliance, i.e. its dilatation ability, storing blood and a portion of the kinetic energy of the flow as transient elastic potential energy, which is then released during the diastolic phase, allowing for a more continuous flow; the inductance, finally, represents the effect of inertia or resistance to changes in blood flow.

There are multiple choices on the number and types of the system compartments: depending on the purpose and available resources (computational and data-wise) the system can be constructed in different ways.
We developed a computational model inspired by previous ones present in literature [1–3], using 0D time varying elastance models for each of the four heart chambers (Equations 2.2), 0D (R, L, C) models for the systemic and pulmonary circulations, considering their arterial and venous compartments along with the addition of their capillaries that, only in the pulmonary system, are further divided into the oxygenated and non-oxygenated ones [31], and, finally, 0D non-ideal diode for the cardiac valves .
Elastance model's characteristic times and lumped parameters are respectively reported in Table 2.1 and Table 2.2.

Table 2.1: Cardiac phases characteristic times.

Acronym	Full Name	Value	Units
t_{LA}^{C}	Left atrial contraction instant	$0.75 \times T_{HB}$	s
T_{LA}^{C}	Left atrial contraction duration	$0.1 \times T_{HB}$	s
t_{LA}^{R}	Left atrial relaxation instant	$t_{LA}^{C} + T_{LA}^{C}$	s
T_{LA}^{R}	Left atrial relaxation duration	$0.8 \times T_{HB}$	s
t_{RA}^{C}	Right atrial contraction instant	$0.8 \times T_{HB}$	s
T_{RA}^{C}	Right atrial contraction duration	$0.1 \times T_{HB}$	s
t_{RA}^{R}	Right atrial relaxation instant	$t_{RA}^{C} + T_{RA}^{C}$	s
T_{RA}^{R}	Right atrial relaxation duration	$0.7 \times T_{HB}$	s
t_{LV}^{C}	Left ventricular contraction instant	$0 \times T_{HB}$	s
T_{LV}^{C}	Left ventricular contraction duration	$0.265 \times T_{HB}$	s
t_{LV}^{R}	Left ventricular relaxation instant	T_{LV}^{C}	s
T_{LV}^{R}	Left ventricular relaxation duration	$0.4 \times T_{HB}$	s
t_{RV}^{C}	Right ventricular contraction instant	$0 \times T_{HB}$	s
T_{RV}^{C}	Right ventricular contraction duration	$0.3 \times T_{HB}$	s
t_{RV}^{R}	Right ventricular relaxation instant	T_{RV}^{C}	s
T_{RV}^{R}	Right ventricular relaxation duration	$0.4 \times T_{HB}$	s

Table 2.2: Model parameters abbreviations.

Acronym	Full Name	Units of measure
E_{LA}^{A}	Left atrial active elastance	$mmHg\ ml^{-1}$
E_{LA}^{B}	Left atrial passive elastance	$mmHg\ ml^{-1}$
V_{LA}^{0}	Left atrial unstressed volume	ml
E_{LV}^{A}	Left ventricular active elastance	$mmHg\ ml^{-1}$
E_{LV}^{B}	Left ventricular passive elastance	$mmHg\ ml^{-1}$
V_{LV}^{0}	Left ventricular unstressed volume	ml
E_{RA}^{A}	Right atrial active elastance	$mmHg\ ml^{-1}$
E_{RA}^{B}	Right atrial passive elastance	$mmHg\ ml^{-1}$
V_{RA}^{0}	Right atrial unstressed volume	ml
E_{RV}^{A}	Right ventricular active elastance	$mmHg\ ml^{-1}$
E_{RV}^{B}	Right ventricular passive elastance	$mmHg\ ml^{-1}$
V_{RV}^{0}	Right ventricular unstressed volume	ml
R_{AR}^{SYS}	Systemic arterial resistance	$mmHg\ s\ ml^{-1}$
C_{AR}^{SYS}	Systemic arterial capacitance	$ml\ mmHg^{-1}$
L_{AR}^{SYS}	Systemic arterial inductance	$mmHg\ s^2\ ml^{-1}$
R_{C}^{SYS}	Systemic capillary resistance	$mmHg\ s\ ml^{-1}$
C_{C}^{SYS}	Systemic capillary capacitance	$ml\ mmHg^{-1}$
R_{VEN}^{SYS}	Systemic venous resistance	$mmHg\ s\ ml^{-1}$
C_{VEN}^{SYS}	Systemic venous capacitance	$ml\ mmHg^{-1}$
L_{VEN}^{SYS}	Systemic venous inductance	$mmHg\ s^2\ ml^{-1}$
R_{AR}^{PUL}	Pulmonary arterial resistance	$mmHg\ s\ ml^{-1}$
C_{AR}^{PUL}	Pulmonary arterial capacitance	$ml\ mmHg^{-1}$
L_{AR}^{PUL}	Pulmonary arterial inductance	$mmHg\ s^2\ ml^{-1}$
R_{C}^{PUL}	Oxygenated pulmonary capillary resistance	$mmHg\ s\ ml^{-1}$
C_{C}^{PUL}	Oxygenated pulmonary capillary capacitance	$ml\ mmHg^{-1}$
R_{SH}	Non-oxygenated pulmonary capillary resistance	$mmHg\ s\ ml^{-1}$
C_{SH}	Non-oxygenated pulmonary capillary capacitance	$ml\ mmHg^{-1}$
R_{VEN}^{PUL}	Pulmonary venous resistance	$mmHg\ s\ ml^{-1}$
C_{VEN}^{PUL}	Pulmonary venous capacitance	$ml\ mmHg^{-1}$
L_{VEN}^{PUL}	Pulmonary venous inductance	$mmHg\ s^2\ ml^{-1}$
R_{min}	Minimal valve resistance	$mmHg\ s\ ml^{-1}$
R_{max}	Maximal valve resistance	$mmHg\ s\ ml^{-1}$

The chambers are modeled with 0-dimensional elastance relationships [32]:

$$p_i(t) = p_{ex}(t) + E_{ch}(t)(V_{ch} - V_{0,ch}) \tag{2.1}$$

where $p_i(t)$ is the considered chamber pressure, $p_{ex}(t)$ represents the external (to the heart) pressure exerted by the surrounding organs and respiration, $V_{ch}(t)$ is the cardiac volume of the chamber and $V_{0,ch}$ refers to the blood unstressed volume of such chamber. In this study the external pressure is set to zero for simplicity , $p_{ex}(t) = 0$.
The elastance $E_{ch}(t)$ is computed as the sum of a constant value E_B called passive elastance and a sinusoidal oscillating term, which amplitude E_A, is called active elastance [1]. Both E_A and E_B depend on the considered chamber.

$$E_{ch}(t) = E_A e(t) + E_B \tag{2.2}$$

A normalized, time-varying and periodic function $e(t)$ regulates the elastance oscillating behaviour during the heartbeat, for ventricles this term is computed as:

$$e_v(t) = \begin{cases} \frac{1}{2}\left[1 - cos\left(\pi \frac{t}{T_{vc}}\right)\right] & \text{if } 0 \leqslant t \leqslant T_{vc} \\ \frac{1}{2}\left[1 + cos\left(\pi \frac{t-T_{vc}}{T_{vr}}\right)\right] & \text{if } T_{vc} < t \leqslant T_{vc} + T_{vr} \\ 0 & \text{if } T_{vc} + T_{vr} < t \leqslant T_{HB} \end{cases} \tag{2.3}$$

Whit just a time translation it can be obtained the atria version of this term :

$$e_a(t) = \begin{cases} \frac{1}{2}\left[1 + cos\left(\pi \frac{t+T_{HB}-t_{ar}}{T_{ar}}\right)\right] & \text{if } 0 \leqslant t \leqslant t_{ar} + T_{ar} - T_{HB} \\ 0 & \text{if } t_{ar} + T_{ar} - T_{HB} < t \leqslant t_{ac} \\ \frac{1}{2}\left[1 - cos\left(\pi \frac{t-t_{ac}}{T_{ac}}\right)\right] & \text{if } t_{ac} < t \leqslant t_{ac} + T_{ac} \\ \frac{1}{2}\left[1 + cos\left(\pi \frac{t-t_{ar}}{T_{ar}}\right)\right] & \text{if } t_{ac} + T_{ac} < t \leqslant T_{HB} \end{cases} \tag{2.4}$$

Here, the subscript ‘v’ denotes the ventricles, and ‘a’ the atria, T_{HB} is the duration of a heartbeat. The following subscript, ‘c’ or ‘r’, refer to contraction or relaxation, respectively. ‘t_{xx}’ represents the chamber phase (contraction/relaxation) starting time, whereas ‘T_{xx}’ is the phase duration.

For each RLC compartment the pressure and flow rate equations can be computed (Equations 2.5).

$$\begin{aligned} L\frac{dQ_o}{dt} + R \cdot Q_o &= P_i - P_o, \\ C\frac{d(P_i - p_{ex})}{dt} &= Q_i - Q_o \end{aligned} \tag{2.5}$$

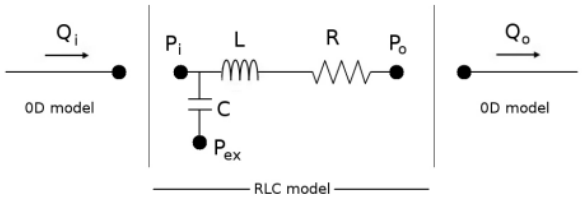

Figure 2.1: Single compartment circuit representation, legend i:input, o:output. Image taken from [1]

Finally, each cardiac valve resistance $R_{TV}(p_{RA}, p_{RV})$, $R_{PV}(p_{RV}, p_{AR}^{PUL})$, $R_{MV}(p_{LA}, p_{LV})$, $R_{AV}(p_{LV}, p_{AR}^{SYS})$ depend on its Pre-valve and Post-valve pressures according to the following relationship:

$$R_i(p_1, p_2) = \begin{cases} R_{min} & \text{if } p_1 > p_2 \\ R_{max} & \text{if } p_1 \leq p_2 \end{cases} \quad \text{for i} \in \{MV, AV, TV, PV\}, \tag{2.6}$$

where p_1 and p_2 represent the upstream and downstream pressures with respect to the flow direction, whereas R_{min} and R_{max} are the minimum and maximum resistance of the valves.

In an ideal valve, R_{min} would be 0 to simulate complete opening and perfect blood passage. R_{max}, on the other hand, would be infinitely large $(+\infty)$ to model a complete closure of the leaflets.

In reality there is dissipation of mechanical energy in the first scenario and some blood leakage (called 'valve regurgitation') in the second one.

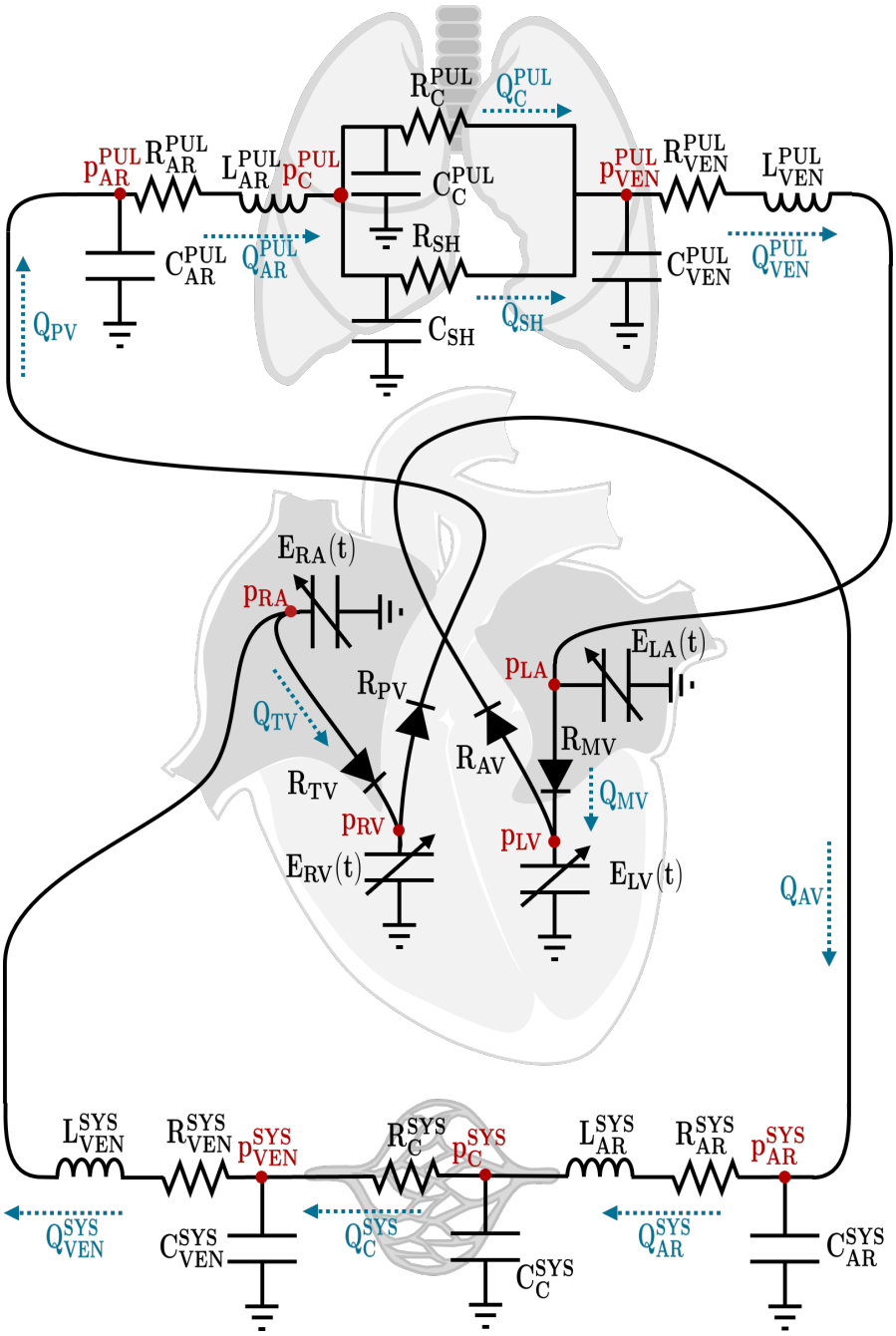

Figure 2.2: Lumped-parameter cardiocirculatory model. The system unkwnown pressures and flow rates are in red and blue, respectively, whereas the model parameters are in black. Image taken from [31]

The resulting system of ODEs associated with the lumped-parameters system is obtained by setting the continuity equations of flow rates at the circuit nodes and of pressure in the vessels. By solving this system it can be obtained the numerical solution of the temporal trend within one heartbeat of the system unknowns: the 4 chambers volumes

$V_{RA}(t)$, $V_{LA}(t)$, $V_{RV}(t)$, $V_{LV}(t)$, the systemic and pulmonary arterial, capillary and venous pressures $p^{SYS}_{VEN}(t)$, $p^{PUL}_{VEN}(t)$, $p^{SYS}_{AR}(t)$, $p^{PUL}_{AR}(t)$, $p^{SYS}_{C}(t)$, $p^{PUL}_{C}(t)$, and the systemic and pulmonary arterial and venous blood fluxes $Q^{SYS}_{VEN}(t)$, $Q^{PUL}_{VEN}(t)$, $Q^{SYS}_{AR}(t)$, $Q^{PUL}_{AR}(t)$.

$$
\begin{cases}
C^{SYS}_{VEN}\dfrac{dp^{SYS}_{VEN}}{dt} = Q^{SYS}_{AR} - Q^{SYS}_{VEN} & C^{PUL}_{VEN}\dfrac{dp^{PUL}_{VEN}}{dt} = Q^{PUL}_{AR} - Q^{PUL}_{VEN} \\
\dfrac{L^{SYS}_{VEN}}{R^{SYS}_{VEN}}\dfrac{dQ^{SYS}_{VEN}}{dt} = -Q^{SYS}_{VEN} - \dfrac{p_{RA} - p^{SYS}_{VEN}}{R^{SYS}_{VEN}} & \dfrac{L^{PUL}_{VEN}}{R^{PUL}_{VEN}}\dfrac{dQ^{PUL}_{VEN}}{dt} = -Q^{PUL}_{VEN} - \dfrac{p_{LA} - p^{PUL}_{VEN}}{R^{PUL}_{VEN}} \\
\dfrac{dV_{RA}}{dt} = Q^{SYS}_{VEN} - Q_{TV}(p_{RA}, p_{RV}) & \dfrac{dV_{LA}}{dt} = Q^{PUL}_{VEN} - Q_{MV}(p_{LA}, p_{LV}) \\
\dfrac{dV_{RV}}{dt} = Q_{TV}(p_{RA}, p_{RV}) - Q_{PV}(p_{RV}, p^{PUL}_{AR}) & \dfrac{dV_{LV}}{dt} = Q_{MV}(p_{LA}, p_{LV}) - Q_{AV}(p_{LV}, p^{SYS}_{AR}) \\
C^{PUL}_{AR}\dfrac{dp^{PUL}_{AR}}{dt} = Q_{PV}(p_{RV}, p^{PUL}_{AR}) - Q^{PUL}_{AR} & C^{SYS}_{AR}\dfrac{dp^{SYS}_{AR}}{dt} = Q_{AV}(p_{LV}, p^{SYS}_{AR}) - Q^{SYS}_{AR} \\
\dfrac{L^{PUL}_{AR}}{R^{PUL}_{AR}}\dfrac{dQ^{PUL}_{AR}}{dt} = -Q^{PUL}_{AR} - \dfrac{p^{PUL}_{VEN} - p^{PUL}_{AR}}{R^{PUL}_{AR}} & \dfrac{L^{SYS}_{AR}}{R^{SYS}_{AR}}\dfrac{dQ^{SYS}_{AR}}{dt} = -Q^{SYS}_{AR} - \dfrac{p^{SYS}_{VEN} - p^{SYS}_{AR}}{R^{SYS}_{AR}} \\
C^{SYS}_{C}\dfrac{dp^{SYS}_{C}}{dt} = Q^{SYS}_{AR} - Q^{SYS}_{C}(p^{SYS}_{C}, p^{SYS}_{VEN}) & \dfrac{dp^{PUL}_{C}}{dt} = \dfrac{Q^{PUL}_{AR} - Q_{SH}(p^{PUL}_{C}, p^{PUL}_{VEN}) - Q^{PUL}_{C}(p^{PUL}_{C}, p^{PUL}_{VEN})}{(C^{PUL}_{C} + C_{SH})}
\end{cases}
\tag{2.7}
$$

From the unknowns a lot other quantities can be computed, such as the atrial and ventricular pressures $p_{RA}(t)$, $p_{LA}(t)$, $p_{RV}(t)$, $p_{LV}(t)$, the blood fluxes through the cardiac valves $Q_{TV}(t)$, $Q_{MV}(t)$, $Q_{PV}(t)$, $Q_{AV}(t)$, the fluxes across the capillaries $Q^{SYS}_{C}(t)$, $Q^{PUL}_{C}(t)$, $Q_{SH}(t)$ and a lot more useful quantities. Some of these important clinical quantities are listed in the Table 2.3.

Given the substantial physical variability among patients, it is also possible to calculate the indexed version of these clinical quantities by dividing them by the Body Surface Area BSA, making them more standardized and comparable across individuals with different body sizes.

Table 2.3: Computable patient quantities

Acronym	Full Name	Calculation	Units
V_{LA}^{MAX}	Left Atrial Maximal Volume	$\max(V_{LA})$	ml
LV_{SV}	Left Ventricular Stroke Volume	$\max(V_{LV}) - \min(V_{LV})$	ml
CO	Cardiac Output	$LV_{SV} \times \frac{HR}{1000}$	l/min
LV_{EDV}	Left Ventricular End Diastolic Volume	$\max(V_{LV})$	ml
LV_{ESV}	Left Ventricular End Systolic Volume	$\min(V_{LV})$	ml
LV_{EF}	Left Ventricular Ejection Fraction	$\frac{LV_{SV}}{LV_{EDV}} \times 100$	%
P_{LA}^{MAX}	Left Atrial Maximal Pressure	$\max(P_{LA})$	$mmHg$
P_{LA}^{MIN}	Left Atrial Minimal Pressure	$\min(P_{LA})$	$mmHg$
P_{LA}^{MEAN}	Left Atrial Mean Pressure	$\frac{\int_{T_{HB}} P_{LA}\, dt}{T_{HB}}$	$mmHg$
P_{LV}^{MAX}	Left Ventricular Maximal Pressure	$\max(P_{LV})$	$mmHg$
P_{LV}^{MIN}	Left Ventricular Minimal Pressure	$\min(P_{LV})$	$mmHg$
V_{RA}^{MAX}	Right Atrial Maximal Volume	$\max(V_{RA})$	ml
RV_{SV}	Right Ventricular Stroke Volume	$\max(V_{RV}) - \min(V_{RV})$	ml
RV_{EDV}	Right Ventricular End Diastolic Volume	$\max(V_{RV})$	ml
RV_{ESV}	Right Ventricular End Systolic Volume	$\min(V_{RV})$	ml
RV_{EF}	Right Ventricular Ejection Fraction	$(1 - \frac{RV_{ESV}}{RV_{EDV}}) \times 100$	%
P_{RA}^{MAX}	Right Atrial Maximal Pressure	$\max(P_{RA})$	$mmHg$
P_{RA}^{MIN}	Right Atrial Minimal Pressure	$\min(P_{RA})$	$mmHg$
P_{RA}^{MEAN}	Right Atrial Mean Pressure	$\frac{\int_{T_{HB}} P_{RA}\, dt}{T_{HB}}$	$mmHg$
P_{RV}^{MAX}	Right Ventricular Maximal Pressure	$\max(P_{RV})$	$mmHg$
P_{RV}^{MIN}	Right Ventricular Minimal Pressure	$\min(P_{RV})$	$mmHg$
SAP_{MAX}	Systolic Systemic Arterial Pressure	$\max(P_{AR}^{SYS})$	$mmHg$
SAP_{MIN}	Diastolic Systemic Arterial Pressure	$\min(P_{AR}^{SYS})$	$mmHg$
SAP_{MEAN}	Mean Systemic Arterial Pressure	$\frac{\int_{T_{HB}} P_{AR}^{SYS}\, dt}{T_{HB}}$	$mmHg$
SCP_{MEAN}	Mean Systemic Capillary Pressure	$\frac{\int_{T_{HB}} P_{C}^{SYS}\, dt}{T_{HB}}$	$mmHg$
SVP_{MEAN}	Mean Systemic Venous Pressure	$\frac{\int_{T_{HB}} P_{VEN}^{SYS}\, dt}{T_{HB}}$	$mmHg$
PAP_{MAX}	Systolic Pulmonary Arterial Pressure	$\max(P_{AR}^{PUL})$	$mmHg$
PAP_{MIN}	Diastolic Pulmonary Arterial Pressure	$\min(P_{AR}^{PUL})$	$mmHg$
PAP_{MEAN}	Mean Pulmonary Arterial Pressure	$\frac{\int_{T_{HB}} P_{AR}^{PUL}\, dt}{T_{HB}}$	$mmHg$
PWP_{MAX}	Maximal Pulmonary Wedge Pressure	$\max(P_{VEN}^{PUL})$	$mmHg$
PWP_{MIN}	Minimal Pulmonary Wedge Pressure	$\min(P_{VEN}^{PUL})$	$mmHg$
PWP_{MEAN}	Mean Pulmonary Wedge Pressure	$\frac{\int_{T_{HB}} P_{VEN}^{PUL}\, dt}{T_{HB}}$	$mmHg$
$shunt$	Shunt Fraction	$\frac{\int_{T_{HB}} Q_{SH}\, dt}{(T_{HB})} \times \frac{1000}{60} \times 100$	%

2.2. Dormand-Prince method

The Dormand-prince method belongs to the embeeded Runge-Kutta family of methods for the numerical solution of ordinary differential equations.

Runge-Kutta methods aim to find the numerical solution of the initial value problem:

$$\frac{dy(t)}{dt} = f(t, y), \qquad y(t_0) = y_0 \tag{2.8}$$

And have the general formula:

$$\begin{aligned} y_{n+1} &= y_n + h \sum_{i=1}^{s} b_i k_i, \\ k_i &= f\left(t_n + c_i h, y_n + h \sum_{j=1}^{s} a_{ij} k_j\right), \quad i = 1, ...s \end{aligned} \tag{2.9}$$

$y(t)$ is the unknown function of the problem, its rate of change $\frac{dy(t)}{dt}$ is a function f depending on time t and of $y(t)$ itself.
$y_n(t)$ is the numerical solution at each step (n) of size h of the method, computed along $[t_0, t_f]$, namely the considered time frame (in this study context the heartbeat period).

For each time instant t_n the new numerical solution $y_{n+1}(t)$ is computed using the previous solution at that point $y_n(t)$ and a weighted combination of coefficients k_i .
These coefficients use the problem f to give an evaluation of the function y derivatives in the time step proximity.
Information is gathered from specific points within the time interval determined by the method step size h. Evaluating the derivatives of the function at various intermediate points (fractions of h), allows the method to capture the behavior of the function more accurately within the given interval.

The characteristics of the different Runge-Kutta methods depend on the parameters set a_{ij}, b_j, c_i, usually arranged together in a mnemonic device, known as Butcher tableau (Table 2.4).

The parameters summed up in the Butcher tableau decide the computation (a_{ij}, c_i) and

c_1	a_{11}	a_{12}	$\dots$	$a_{1,s-1}$	$a_{1,s}$
c_2	a_{21}	a_{22}	$\dots$	$a_{2,s-1}$	$a_{2,s}$
c_3	a_{31}	a_{32}	$\dots$	$a_{3,s-1}$	$a_{3,s}$
$\vdots$	$\vdots$	$\vdots$	$\ddots$	$\vdots$	$\vdots$
c_s	a_{s1}	a_{s2}	$\dots$	$a_{s,s-1}$	$a_{s,s}$
	b_1	b_2	$\dots$	b_{s-1}	b_s

Table 2.4: Butcher tableau for Runge-Kutta methods

the weight (b_j) of the coefficients k_i.
If, for instance, the parameters a_{ij} are zero for every $j \geq i$, only data from the previous steps (n or below) is used for the evaluation of the new y_{n+1}, making the method explicit.

The embedded Runge-Kutta methods are designed to produce an estimate of the local truncation error of a single Runge–Kutta step, and as a result, allow to control the error by adapting the step size h.

This is achieved by combining two methods (Table 2.5): the standard one b_i with convergence order p (Equation 2.9) and a second one b_i^* with lower convergence order p-1:

$$y_{n+1}^* = y_n + h \sum_{i=1}^{s} b_i^* k_i \tag{2.10}$$

c_1	a_{11}	a_{12}	$\dots$	$a_{1,s-1}$	$a_{1,s}$
c_2	a_{21}	a_{22}	$\dots$	$a_{2,s-1}$	$a_{2,s}$
c_3	a_{31}	a_{32}	$\dots$	$a_{3,s-1}$	$a_{3,s}$
$\vdots$	$\vdots$	$\vdots$	$\ddots$	$\vdots$	$\vdots$
c_s	a_{s1}	a_{s2}	$\dots$	$a_{s,s-1}$	$a_{s,s}$
	b_1	b_2	$\dots$	b_{s-1}	b_s
	b_1^*	b_2^*	$\dots$	b_{s-1}^*	b_s^*

Table 2.5: Butcher tableau for Embedded Runge-Kutta methods

Dormand-Prince uses 6 estimations of the function f to calculate fourth and fifth order accurate solutions (Table 2.6 , Equations 2.11).

0							
$\frac{1}{5}$	$\frac{1}{5}$						
$\frac{3}{10}$	$\frac{3}{40}$	$\frac{9}{40}$					
$\frac{4}{5}$	$\frac{44}{45}$	$-\frac{56}{15}$	$\frac{32}{9}$				
$\frac{8}{9}$	$\frac{19372}{6561}$	$-\frac{25360}{2187}$	$\frac{64448}{6561}$	$-\frac{212}{729}$			
1	$\frac{9017}{3168}$	$-\frac{355}{33}$	$\frac{46732}{5247}$	$\frac{49}{176}$	$-\frac{5103}{18656}$		
1	$\frac{35}{384}$	0	$\frac{500}{1113}$	$\frac{125}{192}$	$-\frac{2187}{6784}$	$\frac{11}{84}$	
	$\frac{35}{384}$	0	$\frac{500}{1113}$	$\frac{125}{192}$	$-\frac{2187}{6784}$	$\frac{11}{84}$	0
	$\frac{5179}{57600}$	0	$\frac{7571}{16695}$	$\frac{393}{640}$	$-\frac{92097}{339200}$	$\frac{187}{2100}$	$\frac{1}{40}$

Table 2.6: Butcher tableau for Dorman-Prince method

$$
\begin{aligned}
k_1 &= f(t_n, y_n), \\
k_2 &= f\left(t_n + \tfrac{1}{5}h, y_n + \tfrac{1}{5}k_1\right), \\
k_3 &= f\left(t_n + \tfrac{3}{10}h, y_n + \tfrac{3}{40}k_1 + \tfrac{9}{40}k_2\right), \\
k_4 &= f\left(t_n + \tfrac{4}{5}h, y_n + \tfrac{44}{45}k_1 - \tfrac{56}{15}k_2 + \tfrac{32}{9}k_3\right), \\
k_5 &= f\left(t_n + \tfrac{8}{9}h, y_n + \tfrac{19372}{6561}k_1 - \tfrac{25360}{2187}k_2 + \tfrac{64448}{6561}k_3 - \tfrac{212}{729}k_4\right), \\
k_6 &= f\left(t_n + h, y_n + \tfrac{9017}{3168}k_1 - \tfrac{355}{33}k_2 + \tfrac{46732}{5247}k_3 + \tfrac{49}{176}k_4 - \tfrac{5103}{18656}k_5\right), \\
k_7 &= f\left(t_n + h, y_n + \tfrac{35}{384}k_1 + \tfrac{500}{1113}k_3 + \tfrac{125}{192}k_4 - \tfrac{2187}{6784}k_5 + \tfrac{11}{84}k_6\right).
\end{aligned}
\tag{2.11}
$$

The difference between the two solutions (Equation 2.12) is taken as the error (of the fourth-order solution) by the method to compute the new adapted step size h_{opt} (Equation 2.13).

$$
e_{n+1} = y_{n+1} - y^*_{n+1} \tag{2.12}
$$

$$h_{opt} = h \cdot \left(\frac{\varepsilon h}{2 \cdot |e_{n+1}|} \right)^{\frac{1}{5}} \tag{2.13}$$

In conclusion, the Dormand-Prince method, an embedded (and explicit) method, strategically chooses coefficients to minimize errors in the fifth-order solution. Despite its seven-stage structure, it uses only six evaluations per step. It's noteworthy that k_2 remains unused in the solutions computation, a direct outcome of the specific coefficient selection.

2.3. Backward differentiation formula

The backward differentiation formula is a family of implicit methods for the numerical integration of initial value problems (Equation 2.8).

$$\frac{dy(t)}{dt} = f(t, y), \qquad y(t_0) = y_0 \tag{2.14}$$

$$\sum_{k=0}^{s} a_k \cdot y_{n+k} = h\beta f(t_{n+s}, y_{n+s}) \tag{2.15}$$

They, in turn, belong to the broader family of the linear multistep methods.
Runge-Kutta methods (reviewed in Section 2.2) involve taking intermediate steps to achieve a higher order, but they discard all previous information before proceeding to the next step.
In contrast, multistep methods aim to enhance efficiency by retaining and utilizing information from previous steps instead of discarding it. As a result, multistep methods consider several preceding points and derivative values in their computations.

Ode15s provided by MATLAB® is one of the two solvers used in this study, it implements a variable step, variable order Backward Differentiation Formula (BDF) method that ranges from order 1 to 5 [33].

$$\begin{aligned}
&y_{n+1} - y_n = hf(t_{n+1}, y_{n+1}) \\
&y_{n+2} - \frac{4}{3}y_{n+1} + \frac{1}{3}y_n = \frac{2}{3}hf(t_{n+2}, y_{n+2}) \\
&y_{n+3} - \frac{18}{11}y_{n+2} + \frac{9}{11}y_{n+1} - \frac{2}{11}y_n = \frac{6}{11}hf(t_{n+3}, y_{n+3}) \\
&y_{n+4} - \frac{48}{25}y_{n+3} + \frac{36}{25}y_{n+2} - \frac{16}{25}y_{n+1} + \frac{3}{25}y_n = \frac{12}{25}hf(t_{n+4}, y_{n+4}) \\
&y_{n+5} - \frac{300}{137}y_{n+4} + \frac{300}{137}y_{n+3} - \frac{200}{137}y_{n+2} + \frac{75}{137}y_{n+1} - \frac{12}{137}y_n = \frac{60}{137}hf(t_{n+5}, y_{n+5})
\end{aligned} \tag{2.16}$$

The Equations 2.16 are nonlinear, it is a consequence of the implicit nature of the Backward Differentiation Formulas employed.

The solution at the next time step is implicitly embedded in the equation, necessitating the use of iterative methods to solve for it.
The order of the BDF equation, dictates the complexity of the nonlinear system. Higher-order BDFs involve more terms of the previous solution, resulting in more intricate nonlinear equations. This intricacy, however, comes with a significant benefit.
Higher-order BDFs are particularly advantageous in handling stiff problems, where rapid changes in some components of the system require smaller time steps for stability.
The adaptive nature of the ode15s method allows it to dynamically adjust the order of the BDF method on each iteration, based on the stiffness of the system.
To solve these nonlinear equations, ode15s utilizes iterative approaches, such as the Newton-Raphson.

$$\mathbf{x}_{n+1} = \mathbf{x}_n - \mathbf{J}^{-1}(\mathbf{x}_n)\mathbf{F}(\mathbf{x}_n) \tag{2.17}$$

Where $\mathbf{x}_{n+1}$ is the new solution approximation, $\mathbf{x}_n$ is the current step solution approximation, $\mathbf{F}$ is the problem function and $\mathbf{J}$ its Jacobian matrix. This iterative method starts from an initial guess and look for the vector solution $\mathbf{x}$ of the root problem (Equation 2.18) until a convergence criteria is achieved.

$$\mathbf{F}(\mathbf{x}) = \mathbf{0} \tag{2.18}$$

In each iteration it refines the root position $\mathbf{x}_{n+1}$ using the direction given by the inverse Jacobian matrix of the problem function.

2.4. L-BFGS-B

We calibrated the lumped-parameter model for different clinical data sets using an optimization method.
Employing a loss function L, we quantified numerically the discrepancy between the model output data and the in vivo clinical measurements at our disposal.

$$L(\mathbf{p}) = \frac{\mathbf{1}}{\mathbf{N}} \sum_{\mathbf{i=1}}^{\mathbf{N}} \left(\frac{\mathbf{q_i(p)} - \mathbf{d_i}}{\mathbf{d_i}} \right)^{\mathbf{2}} \tag{2.19}$$

where N is the number of available clinical data and d_i the value of the i-th clinical data. q_i is the value of the model output related to the i-th clinical data, computed with a lumped-parameters configuration $\mathbf{p}$
Through the minimization of this loss function, the method actively seeks a lumped-parameters configuration that reproduces the patient data as close as possible.
The optimization, achieved by loss minimization means, was executed using the Quasi-Newton method L-BFGS-B implemented in Scipy [34].
This is a Limited memory ('L-') and Bounded ('-B') version of the Broyden, Fletcher, Goldfarb, Shanno (BFGS) algorithm.
BFGS is an iterative method for solving unconstrained nonlinear optimization problems, it improves the descent direction, usually determined by the gradient, by preconditioning the gradient itself with information on the loss function curvature.
This curvature information is provided by the inverse of the loss function Hessian matrix. Calculating the precise Hessian matrix, which involves second-order partial derivatives of the loss function with respect to each variable, can be computationally demanding and impractical, especially in high-dimensional optimization problems.
Instead, BFGS uses an approximation B_k for the inverse Hessian matrix and iteratively improves it by considering the differences between successive positions s_k and their corresponding gradients y_k.

$$B_{k+1} = B_k + \frac{y_k y_k^T}{y_k^T s_k} - \frac{B_k s_k s_k^T B_k}{s_k^T B_k s_k} \tag{2.20}$$

While the standard BFGS method stores a complete $n \times n$ matrix, L-BFGS-B represents this inverse Hessian approximation implicitly by maintaining a limited set of vectors.

This memory-saving strategy not only reduces the computational cost but also allows L-BFGS-B to store information from multiple previous steps, effectively extending its "memory" to consider a more extensive history of iterations.
Additionaly, L-BFGS-B employs bound constraints on variables. Each problem variable x_i can be constrained in a box with a lower bound l_i and an upper bound u_i. The approach involves identifying both fixed and free variables at each step through a straightforward gradient method. Subsequently, the L-BFGS method is applied exclusively to the free variables, increasing the overall efficiency of the process.
The algorithm outline is reported in Table 2.7.
It initializes by computing the gradient of the loss function at the current point. The algorithm maintains information from the last m iterations, tracking differences in positions (s_k) and corresponding gradients (y_k). It employs a first cycle to calculate a search direction q and updates it iteratively using coefficients α_i, computed from stored s_i and y_i. These coefficients α_i measure how much the previous stages gradients should weight on the corrections made on the descent direction.
Subsequently, it computes an initial approximation of the inverse Hessian B_k^0 and determines the initial descent direction z. The second cycle refines z by adjusting it with coefficients β_i calculated again from the stored gradients.
Finally, it computes the descent direction p_k, calculate the next step solution x_{k+1}, and adjusts the inverse Hessian approximation for the next iteration (Equation 2.20). The algorithm repeats these steps until a convergence criterion is met.

Table 2.7: L-BFGS-B Optimization Algorithm

For $k = 1, 2, \ldots,$ max_iter
  Compute the gradient $g_k = \nabla f(x_k)$
  Last m states stored as:
    $s_k = x_{k+1} - x_k$
    $y_k = g_{k+1} - g_k$
    $\rho_k = 1/(y_k^T s_k)$
  Initialize $q = g_k$
  For $i = k, k-1, \ldots, k-m+1$
    Compute $\alpha_i = \rho_i s_i^T q$
    Update $q = q - \alpha_i y_i$
  Compute an initial approximation of the inverse Hessian $B_k^0 = \frac{s_{k-1} y_{k-1}}{y_{k-1}^T y_{k-1}}$
  Compute the initial direction of descent $z = B_k^0 q$
  For $i = k-m, k-m+1, \ldots, k-1$
    Compute $\beta_i = \rho_i y_i^T z$
    Update $z = z + (\alpha_i - \beta_i) s_i$
  Compute the direction of descent $p_k = -z$
  Update $x_{k+1} = x_k + \alpha_k p_k$;
  Update B_{k+1}^0 using BFGS update formula
  Store the current iteration for future use
  Check for convergence
  If convergence is reached, break the loop

2.5. Sobol' indices

Sobol indices are a technique used in a global sensitivity analysis to quantify the relative impact of different input features in a mathematical or computational model.
These indices provide information on how variations in each input variables affect the different model's outputs.
Operating in a probabilistic framework, each model output Y variance is decomposed into portions which can be attributed to the different model features.
If, for instance, by fixing one input variable the variance of a model output significantly decrease, it means that its influence on the output computation was quite big.
Variance-based sensitivity measures are particularly convenient: they assess sensitivity throughout the entire input space, they are capable of handling non-linear responses, and they can quantify the impact of interactions in systems that are non-additive.

To simplify the notation and maintain generality, the equations that follow will assume that the input variables are uniformly distributed in the interval $[0, 1]$. Consequently, the input set's support is considered to be $D_X = [0, 1]^M$.

It is assumed that the inputs are distributed independently and uniformly within the unit hypercube $X_i \in [0, 1]$ for $i = 1, 2, \ldots, d$.

Initially, each output Y can be decomposed:

$$Y = f_0 + \sum_{i=1}^{d} f_i(X_i) + \sum_{i<j}^{d} f_{ij}(X_i, X_j) + \cdots + f_{1,2,\ldots,d}(X_1, X_2, \ldots, X_d) \tag{2.21}$$

where f_0 is constant, f_i is a function of X_i and f_{ij} is a function of X_i and X_j.
A condition of this Sobol' decomposition is that the integrals of the summands with respect to their own variables $f_{i_1,\ldots,i_s}$ vanish:

$$\int_0^1 f_{i_1,\ldots,i_s}(X_{i_1,\ldots,i_s}) dX_{ik} = 0 \quad if \quad 1 \leq k \leq s \tag{2.22}$$

This implies that all the functional terms involved in this decomposition are orthogonal.
The terms of the functional decomposition can now be expressed as conditional expected values (Equations 2.23).

$$
\begin{aligned}
&f_0 = \mathbb{E}(Y), \\
&f_i(X_i) = \mathbb{E}(Y|X_i) - f_0, \\
&f_{ij}(X_i, X_j) = \mathbb{E}(Y|X_i, X_j) - f_0 - f_i - f_j
\end{aligned}
\tag{2.23}
$$

Subsequently by assuming that $f(\mathbf{X})$ is square-integrable the decomposition (Equation 2.21) can be squared and integrated (Equation 2.24).

$$
\int f^2(\mathbf{X})\, d\mathbf{X} - f_0^2 = \sum_{s=1}^{d} \sum_{i_1 < \cdots < i_s}^{d} \int f_{i_1,\ldots,i_s}^2 \, d\mathbf{X}_{i_1} \ldots d\mathbf{X}_{i_s} \tag{2.24}
$$

Here, the left-hand side denotes the sought variance of one model model output Y, whereas the right hand side terms are variance terms, now decomposed for different sets of the model inputs $\mathbf{X}$:

$$
\begin{aligned}
&Var(Y) = \sum_{i=1}^{d} V_i + \sum_{i=1}^{d} V_{ij} + \cdots + V_{12\ldots d}, \\
&V_i = Var_{Xi}(\mathbb{E}_{\mathbf{X}\sim i}(Y|X_i)), \\
&V_{ij} = Var_{Xij}(\mathbb{E}_{\mathbf{X}\sim ij}(Y|X_i, X_j)) - V_i - V_j,
\end{aligned}
\tag{2.25}
$$

The notations $X_{\sim i}$ indicates the set of all input variables $\mathbf{X}$ except X_i.
The resulting decomposition shows how the total variance of each model output $Var(Y)$ is the sum of variance terms attributable to each input, as well as the variance interaction effects between them.

Following this variance decomposition first and higher order Sobol' indices are naturally defined:

$$
S_{i_1,\ldots,i_s} = \frac{V_{i_1,\ldots,i_s}}{Var(Y)} \tag{2.26}
$$

The index with respect to one input variable S_i is called the first-order Sobol' index and represents its effect on the model output studied Y.
Multiple-term indices S_{ij} are called higher order Sobol' indices and measure the effect on the model output of the input interactions. Specifically, second-order indices (S_{ij}) account for pairwise interactions, third-order indices (S_{ijk}) consider interactions among triplets, and so forth. The impact of these interactions cannot be decomposed into contributions

of single variables.
Measuring the total impact of a single model input would require to sum all the sobol'indices in which it is involved:

$$S_{T_i} = S_i + \sum_{\substack{j=1 \\ j \neq i}}^{N} S_{ij} + \sum_{\substack{j,k=1 \\ j \neq i, k \neq i, j<k}}^{N} S_{ijk} + \cdots + S_{1\ldots N} \tag{2.27}$$

This procedure would require the explicit computation of all the Sobol' indices up to the order N, where N is the number of model inputs. The implication is that this calculation becomes overly expensive in terms of computational resources as the number of variables N becomes significantly large.
For this reason, the formula for Total-effect Sobol indices S_{T_i} is reformulated into a more practical expression (Equation 2.28).

$$S_{T_i} = 1 - \frac{Var_{\mathbf{X}_{\sim i}}(\mathbb{E}_{Xi}(Y|\mathbf{X}_{\sim i}))}{Var(Y)} \tag{2.28}$$

Now the total index is computed starting from a variance term due to all the model variables excluding the analyzed variable X_i. By subtracting this quantity to 1 what remains is the whole output sensitivity fraction for which the input X_i is responsible.

3 | Modelling of congenital diseases

In this section we review the customization procedure made on the base lumped-parameters model to account for the studied congenital defects.

3.1. PFO implementation: Bernoulli valve model

We modeled the foramen as a valve model based on the Bernoulli formula [4, 5]. The relation between pressure gradient Δp and flow q through an open valve can be approximated by the Bernoulli equation.

$$\Delta p = R^B_{PFO} q|q| + L_{PFO} \frac{dq}{dt} \tag{3.1}$$

Poiseuille viscous losses (proportional to flow rate q) are small and have thus been neglected [35].

The parameter R^B_{PFO} is called Bernoulli resistance and governs pressure gradients related to convective acceleration and dynamic pressure losses caused by the diverging flow past the valve.

$$R^B_{PFO} = \frac{\rho}{2A^2_{eff}} \tag{3.2}$$

where ρ is the considered liquid density and A_{eff} is the effective open area of the valve orifice.
In this study context we consider for blood a density $\rho = 1.06 g/cm^3$.
The parameter L is called Bernoulli inertance and accounts for the blood acceleration effects.

$$L_{PFO} = \frac{\rho\, l_{eff}}{A_{eff}} \tag{3.3}$$

where l_{eff} is the valve effective length and it is estimated in the foramen context as the septum primum and septum secundum overlap.
A_{eff} is considered to be variable in time depending on the valve dynamics.

$$A_{eff}(t) = [A_{eff,max} - A_{eff,min}]\,\zeta(t) + A_{eff,min} \tag{3.4}$$

where $\zeta(t)$ is an index representing the valve dynamic. It ranges from a minimum of 0, when the valve is completely closed, to a maximum of 1 when the valve is completely open.
The orifice effective area ranges between $A_{eff,min}$ and $A_{eff,max}$. These two bound values can be further expressed as

$$\begin{aligned} A_{eff,min} &= M_{reg} A_{ann} \\ A_{eff,max} &= M_{ste} A_{ann} \end{aligned} \tag{3.5}$$

A_{ann} is the area of the annulus containing the foramen.
M_{reg} is called regurgitation factor and allow the model to account for the regurgitation phenomenon explained in Section 1.2.
M_{ste} is called stenosis factor and account for orifice narrowing due to valve constriction. For simplicity this parameter has been set to 1, ignoring the stenosis effects.

Although the valve dynamic is known to be influenced by a number of complex factors, such as the vortex dynamics, the most important one appears to be the pressure gradient Δp across the valve [36–38].

$$\begin{aligned} \frac{d\zeta}{dt} &= (1-\zeta)\, K_{vo}\, (\Delta p - \Delta p_{open}) \quad if \;\; \Delta p \geq 0 \\ \frac{d\zeta}{dt} &= \zeta\, K_{vc}\, (\Delta p - \Delta p_{close}) \qquad\quad if \;\; \Delta p < 0 \end{aligned} \tag{3.6}$$

The valve opening and closure starts when the pressure gradient exceeds a threshold values, respectively Δp_{open} and Δp_{close}.

Both these threshold parameters are set to zero for simplicity.
K_{vo} (valve opening) and K_{vc} (valve closure) are rate coefficients (units: $mmHg^{-1}s^{-1}$) that regulate the valve dynamic speed.

The foramen parameters used, taken from [5], are summed up in the Table 3.1.

Table 3.1: Foramen model parameters

Parameter	Value	Unit of measure
l_{eff}	8.0	mm
K_{vo}	64.5	$mmHg^{-1}s^{-1}$
K_{vc}	96.8	$mmHg^{-1}s^{-1}$
Δp_{open}	0	$mmHg$
Δp_{close}	0	$mmHg$
M_{reg}	0.01	-
M_{ste}	1	-

Using data on foramen typical dimensions [39], three scenario with increasing orifice radius have been considered , Table 3.2.

Table 3.2: Foramen radius

Radius	Value	Unit of measure
r_{small}	5.0	mm
r_{medium}	9.0	mm
r_{large}	13.0	mm

The Bernoulli model for the foramen has been added to the 0D lumped-parameters model (Figure 3.1). The shunt is defined as positive for blood moving from the right atrium to the left atrium.
The equations of the model affected by the foramen implementation are those that govern the behavior of atrial volumes. Their modified version is reported below.

$$\begin{cases} \dfrac{dV_{RA}}{dt} = Q_{VEN}^{SYS} - Q_{TV}(p_{RA}, p_{RV}) - Q_{PFO}(p_{RA}, p_{LA}) \\ \dfrac{dV_{LA}}{dt} = Q_{VEN}^{PUL} - Q_{MV}(p_{LA}, p_{LV}) + Q_{PFO}(p_{RA}, p_{LA}) \end{cases} \tag{3.7}$$

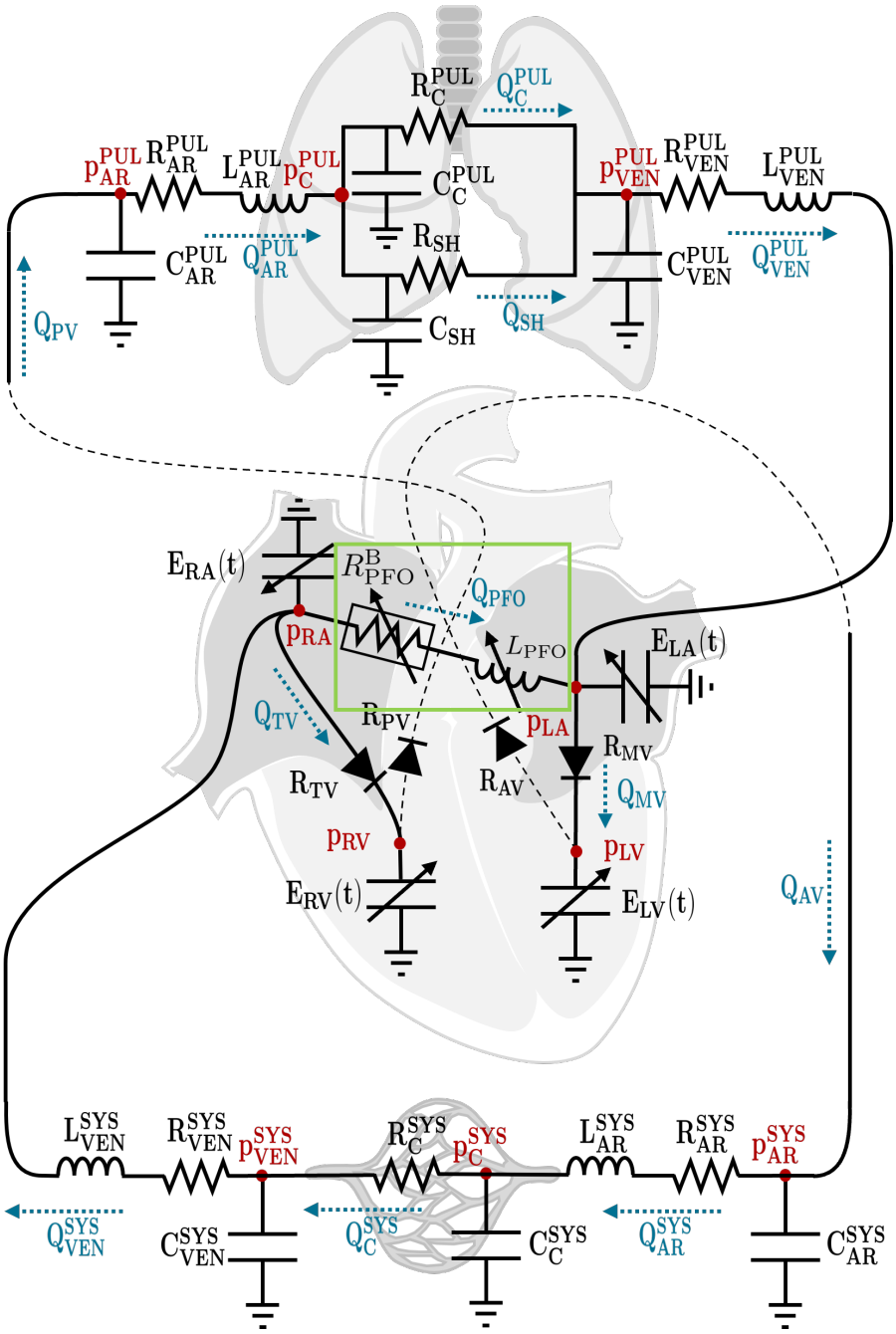

Figure 3.1: Patent foramen ovale (PFO) addition to the 0D lumped-parameters model. The new PFO compartment is highlighted with a green box. The systemic and pulmonary arterial compartments were dashed for a better readability.

The lumped-parameters used for the foramen simulation were calibrated to produce clinical outputs into a healthy range for a male adult, Table 3.3.

Table 3.3: Healty male adult lumped-parameters

Parameter	Value	Unit of measure
E_{LA}^{A}	0.38	$mmHg\ ml^{-1}$
E_{LA}^{B}	0.27	$mmHg\ ml^{-1}$
V_{LA}^{0}	2.3085	ml
E_{LV}^{A}	2.7	$mmHg\ ml^{-1}$
E_{LV}^{B}	6.9×10^{-2}	$mmHg\ ml^{-1}$
V_{LV}^{0}	3.5385	ml
E_{RA}^{A}	1.26×10^{-1}	$mmHg\ ml^{-1}$
E_{RA}^{B}	0.195	$mmHg\ ml^{-1}$
V_{RA}^{0}	3.5385	ml
E_{RV}^{A}	0.43	$mmHg\ ml^{-1}$
E_{RV}^{B}	4.1264×10^{-2}	$mmHg\ ml^{-1}$
V_{RV}^{0}	8.4067	ml
R_{AR}^{SYS}	0.5911	$mmHg\ s\ ml^{-1}$
C_{AR}^{SYS}	1.3315	$ml\ mmHg^{-1}$
L_{AR}^{SYS}	2.9643×10^{-4}	$mmHg\ s^2\ ml^{-1}$
R_{C}^{SYS}	2.17×10^{-2}	$mmHg\ s\ ml^{-1}$
C_{C}^{SYS}	2.7981×10^{-1}	$ml\ mmHg^{-1}$
R_{VEN}^{SYS}	3.596×10^{-1}	$mmHg\ s\ ml^{-1}$
C_{VEN}^{SYS}	$7.5 \times 10^{+1}$	$ml\ mmHg^{-1}$
L_{VEN}^{SYS}	2.0643×10^{-5}	$mmHg\ s^2\ ml^{-1}$
R_{AR}^{PUL}	0.0714	$mmHg\ s\ ml^{-1}$
C_{AR}^{PUL}	6.0043	$ml\ mmHg^{-1}$
L_{AR}^{PUL}	2.0643×10^{-5}	$mmHg\ s^2\ ml^{-1}$
R_{C}^{PUL}	1.7538×10^{-2}	$mmHg\ s\ ml^{-1}$
C_{C}^{PUL}	5.7803	$ml\ mmHg^{-1}$
R_{SH}	3.5174×10^{-1}	$mmHg\ s\ ml^{-1}$
C_{SH}	4.9043×10^{-2}	$ml\ mmHg^{-1}$
R_{VEN}^{PUL}	3.75×10^{-2}	$mmHg\ s\ ml^{-1}$
C_{VEN}^{PUL}	$1.1381 \times 10^{+1}$	$ml\ mmHg^{-1}$
L_{VEN}^{PUL}	2.0643×10^{-5}	$mmHg\ s^2\ ml^{-1}$
R_{min}	6.2872×10^{-3}	$mmHg\ s\ ml^{-1}$
R_{max}	$9.4168 \times 10^{+4}$	$mmHg\ s\ ml^{-1}$

The study of the foramen right to left shunt requires a condition that makes the right atrium pressure exceed the left one.
We achieved this right to left positive pressure gradient by simulating a constriction of the pulmonary artery. The right heart struggles more to pump blood into the pulmonary circulation, resulting in an increase in the right ventricle and right atrium pressures.
The vessel narrowing makes its radius change and consequently its related lumped parameters.
The pulmonary arterial parameters are modified following the vessel electrical analogy equations based on the Poiseuille steady-state flow [40].

$$\begin{aligned} R &= \frac{8\mu l}{\pi r^4} \\ C &= \frac{3\pi r^3 l}{2Eh} \\ L &= \frac{9\rho l}{4\pi r^2} \end{aligned} \tag{3.8}$$

Considering a radius ratio of $r/r_0 = 0.8$ between the constricted radius r and the reference healthy radius r_0, the arterial pulmonary base parameters from Table 3.3 greatly change, Table 3.4.

Table 3.4: Constricted pulmonary artery parameters

Parameter	**Value**	**Unit of measure**
R_{AR}^{PUL}	0.1743	$mmHg\ s\ ml^{-1}$
C_{AR}^{PUL}	3.074	$ml\ mmHg^{-1}$
L_{AR}^{PUL}	3.2254×10^{-5}	$mmHg\ s^2\ ml^{-1}$

3.2. PAPVR modelling: pulmonary venous compartment split

Partial anomalous pulmonary venous return is a congenital defect in which one or more pulmonary veins do not drain in the left atrium but are instead, incorrectly attached to the systemic venous system.
It results that the implementation of this disease requires the independent management of the different pulmonary veins. For this reason the pulmonary venous compartment of the healthy reference model (Table 3.3) has been decomposed into the four main pulmonary veins using formulas for parallel equivalent circuits. The original segment and the four resulting segments naturally share the same pressure at both the inlet (P_{VEN}^{PUL}) and outlet (P_{LA}) points.
The single pulmonary vein parameters results:

$$\frac{1}{R_{eq}} = \frac{1}{R_1} + \frac{1}{R_2} \cdots \frac{1}{R_N} \qquad R_{VEIN} = 4R_{VEN}^{SYS}$$

$$C_{eq} = C_1 + C_2 + \cdots + C_N \qquad C_{VEIN} = \frac{1}{4} C_{VEN}^{SYS}$$

$$\frac{1}{L_{eq}} = \frac{1}{L_1} + \frac{1}{L_2} \cdots \frac{1}{L_N} \qquad L_{VEIN} = 4L_{VEN}^{SYS}$$

The resulting pulmonary veins are therefore completely identical between each other; no considerations are made regarding their exact shape or their origin (left or right lung).
Following this decomposition, the veins can be detached from the left atrium and connected to the right atrium or its tributaries.
In this study, we consider cases in which the anomalous veins are directly connected to the right atrium or the superior vena cava.
In both of these scenarios, we examine cases with one, two or three anomalous veins, all connected to the same location (right atrium or superior vena cava).
Whether anomalous or not, the four pulmonary veins share the same origin pressure P_{VEN}^{PUL}, whereas their downstream pressure depends on where they are attached. Consequently, their capacitances can be considered once again in parallel and, therefore, reassembled together.
The customized models for the atrium case and the superior vena cava case are depicted in the respective figures 3.2, 3.3.
Although only the scenario with a single anomalous vein is shown in these figures, we have analogously modified the model for the cases with two and three anomalous veins.
In the atrium case each normal pulmonary vein blood flow $Q_{VEIN,i}^{PUL}$ is regulated by the

classical R-L equation. N_i is total number of normal veins.

$$\frac{L_{VEIN}^{PUL}}{R_{VEIN}^{PUL}} \frac{dQ_{VEIN,i}^{PUL}}{dt} = -Q_{VEIN,i}^{PUL} - \frac{p_{LA} - p_{VEN}^{PUL}}{R_{VEIN}^{PUL}} \tag{3.9}$$

Whereas each anomalous vein now drain in the right atrium a blood flow $Q_{VEIN,j}^{PUL}$, regulated by the following equation. N_j is total number of anomalous veins.

$$\frac{L_{VEIN}^{PUL}}{R_{VEIN}^{PUL}} \frac{dQ_{VEIN,j}^{PUL}}{dt} = -Q_{VEIN,j}^{PUL} - \frac{p_{RA} - p_{VEN}^{PUL}}{R_{VEIN}^{PUL}} \tag{3.10}$$

The left atrium receives only the blood from the normal veins, whereas the right atrium receives the blood from the systemic venous compartment and from the anomalous veins:

$$\begin{cases} \dfrac{dV_{LA}}{dt} = \displaystyle\sum_{i=1}^{N_i} Q_{VEIN,i}^{PUL} - Q_{MV}(p_{LA}, p_{LV}) \\ \dfrac{dV_{RA}}{dt} = Q_{VEN}^{SYS} + \displaystyle\sum_{j=1}^{N_j} Q_{VEIN,j}^{PUL} - Q_{TV}(p_{RA}, p_{RV}) \end{cases} \tag{3.11}$$

In the superior vena cava case the equation for each normal vein is the same as in the atrium case 3.9.
In contrast, now, the anomalous veins converge into the superior vena cava.

$$\frac{L_{VEIN}^{PUL}}{R_{VEIN}^{PUL}} \frac{dQ_{VEIN,j}^{PUL}}{dt} = -Q_{VEIN,j}^{PUL} - \frac{p_{SVC} - p_{VEN}^{PUL}}{R_{VEIN}^{PUL}} \tag{3.12}$$

Superior vena cava's pressure and flow rate are again regulated by the RLC equations:

$$\begin{cases} C_{SVC} \dfrac{dp_{SVC}}{dt} = Q_{VEN}^{SYS} + \displaystyle\sum_{j=1}^{N_j} Q_{VEIN,j}^{PUL} - Q_{SVC} \\ \dfrac{L_{SVC}}{R_{SVC}} \dfrac{dQ_{SVC}}{dt} = -Q_{SVC} - \dfrac{p_{RA} - p_{SVC}}{R_{SVC}} \end{cases} \tag{3.13}$$

The left atrial volume equation is the same as in the atrium case (Equation 3.11), whereas the right atrial one become:

$$\frac{dV_{RA}}{dt} = Q_{SVC} - Q_{TV}(p_{RA}, p_{RV}) \tag{3.14}$$

The parameters used for both cases in the PAPVR simulations are the ones contained in Table 3.1.

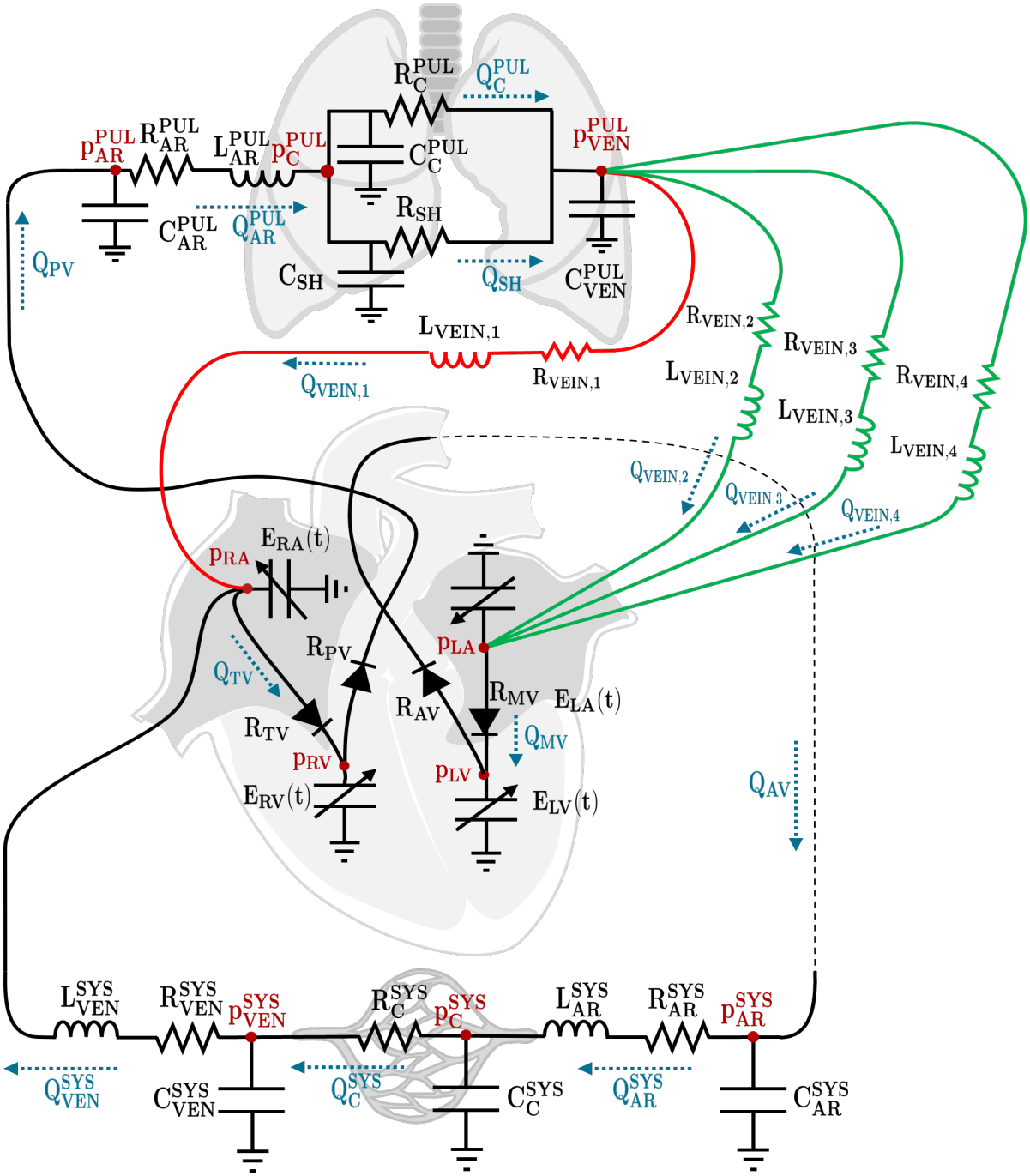

Figure 3.2: Partial anomalous pulmonary venous return (PAPVR) implemenation: anomalous connection to the right atrium. The systemic arterial compartment was dashed for a better readability. The correct veins are in green, whereas the anomalous ones are highlighted in red.

The lumped parameters of the superior vena cava are reported in Table 3.5 [6, 7].

Table 3.5: Superior vena cava lumped parameters

Parameter	Value	Unit of measure
R_{SVC}	1.68×10^{-2}	$mmHg\ s\ ml^{-1}$
C_{SVC}	1	$ml\ mmHg^{-1}$
L_{SVC}	1.5×10^{-3}	$mmHg\ s^2\ ml^{-1}$

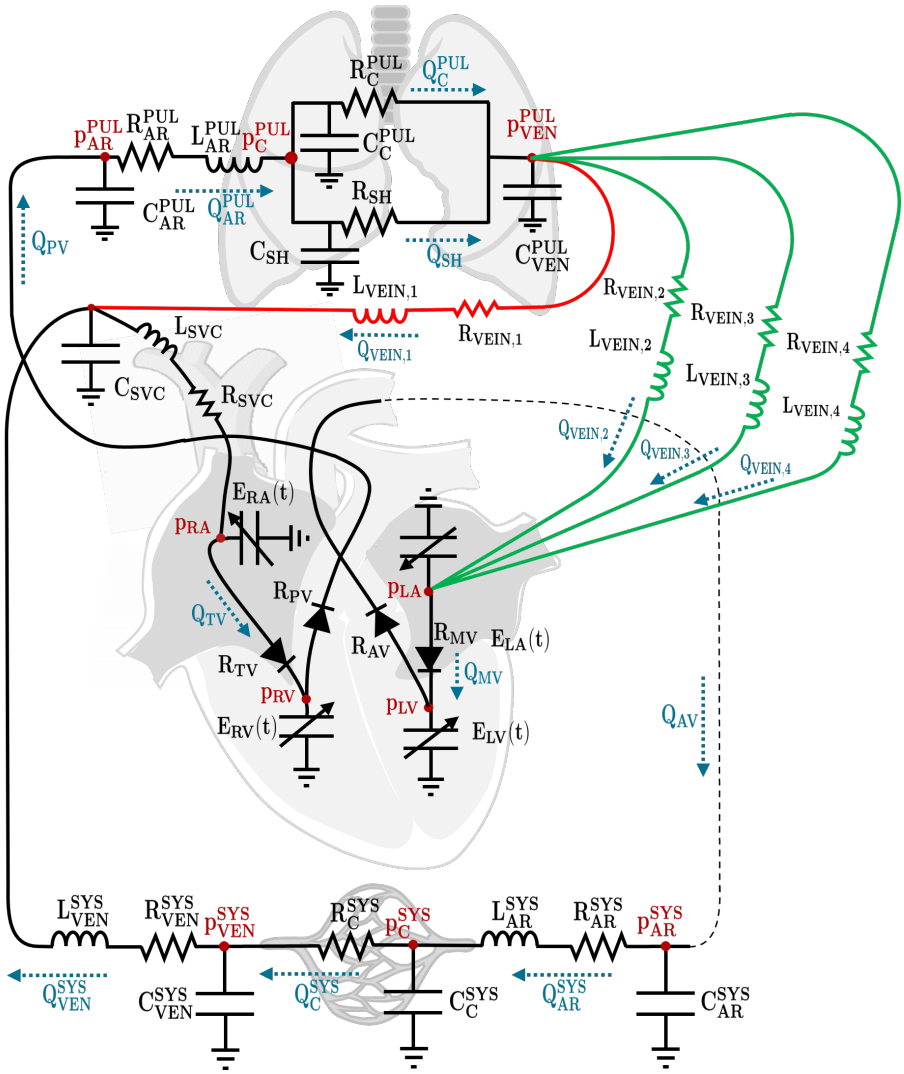

Figure 3.3: Partial anomalous pulmonary venous return (PAPVR) implemenation: anomalous connection to the superior vena cava. The systemic arterial compartment was dashed for a better readability. The correct veins are in green, whereas the anomalous ones are highlighted in red.

3.3. ASD/VSD: model calibration

The atrial and ventricular septal defects were modeled as two resistors that link respectively the two atria and the two ventricles.
We treid to use the resistance Equation 3.8 of the electrical-emodynamic analogy to estimate the defects resistance.
The resulting resistance however, were too small compared to values found in literature [8–11]. For example by considering a small atrial defect of radius $R_{ASD} = 3mm$, using the atrial septal thickness as vessel length $l = 2.5mm$, the resulting resistance would be $R_{ASD} = 3.71 \times 10^{-2}$. The physical implications of this small value of resistance would be an elevated blood shunt and, as a consequence, a pressure match between the two atria. This result is quite unrealistic for a small defect and therefore this formula was deemed as unreliable to estimate the septa defects resistance.
The lumped parameters of the model have been calibrated for three different patients hospitalized at IRCCS Policlinico San Donato in Milan Italy.
All the patients are adult males: the first one present an atrial septal defect (ASD), the second one a ventricular septal defect (VSD) and the third one has both septal defects ($ASD + VSD$).
The clinical data for the VSD patient were measured under standard conditions and during the administration of vasodilators ($VSD + VD$).

Table 3.6: Patients clinical data

Clinical data	*ASD*	*VSD*	*VSD + VD*	*ASD + VSD*	*Units of measure*
p_{RA}^{mean}	15	15	15	13	$mmHg$
p_{RV}^{max}	48	–	–	100	$mmHg$
p_{RV}^{min}	15	–	–	12	$mmHg$
PAP_{max}	50	88	90	99	$mmHg$
PAP_{min}	20	33	35	49	$mmHg$
PAP_{mean}	30	55	35	70	$mmHg$
PWP_{mean}	17	30	33	11	$mmHg$
p_{LV}^{max}	98	–	–	117	$mmHg$
p_{LV}^{min}	17	–	–	7	$mmHg$
SAP_{max}	98	75	75	102	$mmHg$
SAP_{min}	70	48	48	72	$mmHg$
SAP_{mean}	85	55	68	86	$mmHg$
Q_P	7.86	2.44	5.96	5.48	$l \times min^{-1}$
Q_S	3.09	2.44	1.53	5.48	$l \times min^{-1}$
PVR	1.65	10.25	5.2	10.76	WU

In ASD presence the affected equations are the two regulating the atrial volumes. By defining the shunting blood flow as positive if moving from the left to the right atrium, the equations become:

$$\begin{cases} \dfrac{dV_{RA}}{dt} = Q_{VEN}^{SYS} - Q_{TV}(p_{RA}, p_{RV}) - Q_{ASD}(p_{LA}, p_{RA}) \\ \dfrac{dV_{LA}}{dt} = Q_{VEN}^{PUL} - Q_{MV}(p_{LA}, p_{LV}) + Q_{ASD}(p_{LA}, p_{RA}) \end{cases} \tag{3.15}$$

In the same fashion in VSD presence the affected equations are the two involving the ventricular volumes, they result:

$$\begin{cases} \dfrac{dV_{RV}}{dt} = Q_{TV}(p_{RA}, p_{RV}) - Q_{PV}(p_{RV}, p_{AR}^{PUL}) + Q_{VSD}(p_{LV}, p_{RV}) \\ \dfrac{dV_{LV}}{dt} = Q_{MV}(p_{LA}, p_{LV}) - Q_{PV}(p_{LV}, p_{AR}^{SYS}) - Q_{VSD}(p_{LV}, p_{RV}) \end{cases} \tag{3.16}$$

When the patient presents both ASD and VSD all the four chamber volume equations must be modified according to 3.15 and 3.16.

In the Figure 3.4, the introduction of the two resistances modeling septal defects is depicted. Depending on the patient under study, it can be added either or both the atrial and the ventricular resistances.

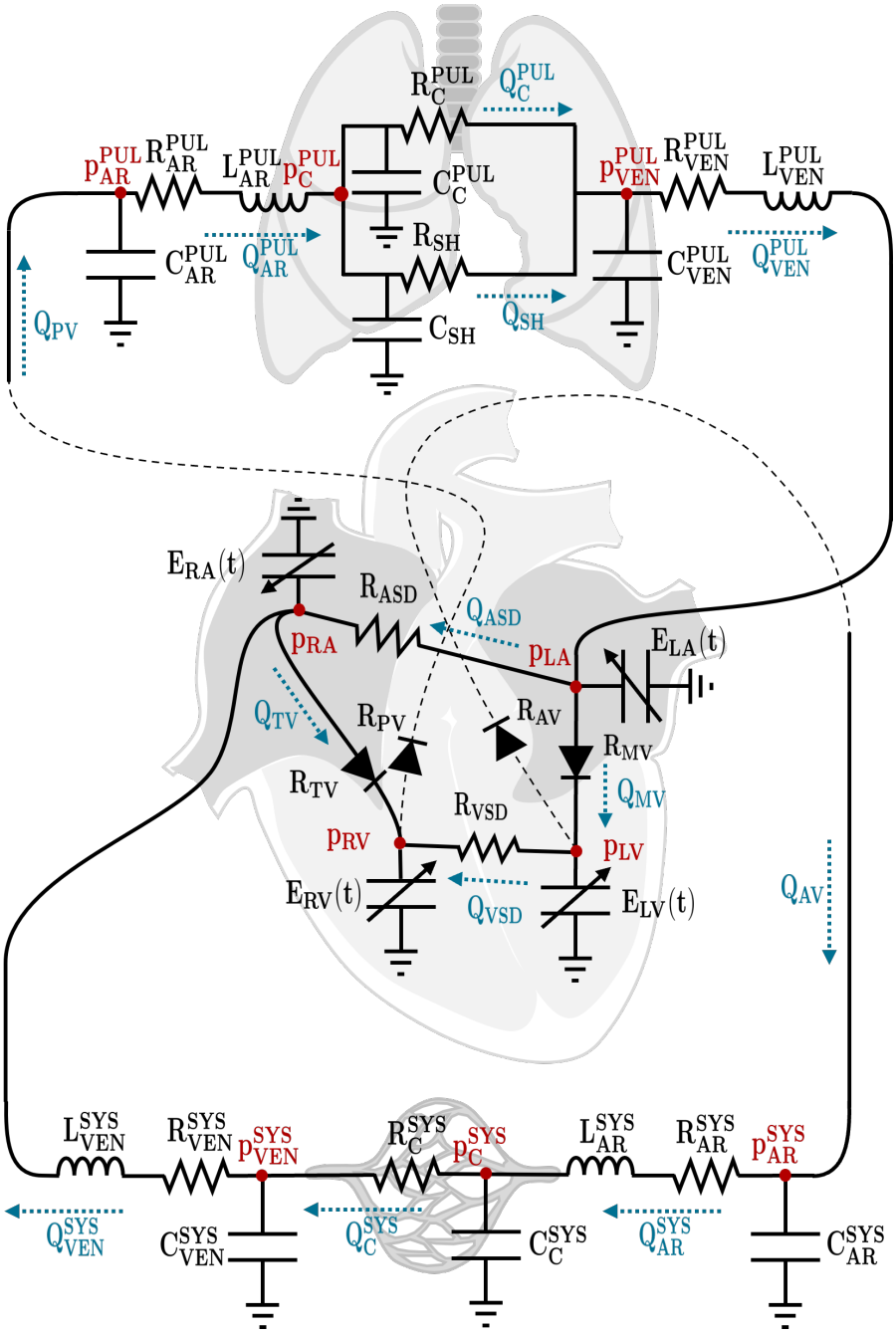

Figure 3.4: ASD and VSD addition to the 0D lumped-parameters model. The systemic and pulmonary arterial compartments were dashed for a better readability.

The total Sobol' indices were used to pinpoint the model parameters allowed to vary in the patient calibration. Setting a threshold of 0.1 we identified E_{LV}^{A}, E_{LV}^{V}, E_{RV}^{A}, E_{RV}^{B},

R_{AR}^{SYS}, C_{AR}^{SYS}, R_{VEN}^{SYS}, R_{VEN}^{PUL}. In addition, also R_{AR}^{PUL} was allowed to vary by computing it at each step as the difference between the measured Pulmonary Vascular Resistance PVR and the sum of the pulmonary venous resistance with the equivalent capillary resistance. The healthy range parameters contained in Table 3.3 were used as initial guess of the calibration process.

	p_{RA}^{mean}	p_{RV}^{max}	p_{RV}^{min}	p_{PA}^{max}	p_{PA}^{min}	p_{PA}^{mean}	p_{VEN}^{PUL}	p_{LV}^{max}	p_{LV}^{min}	p_{AO}^{max}	p_{AO}^{min}
E_{LA}^{A}	$1.8 \cdot 10^{-5}$	$1.9 \cdot 10^{-4}$	$7.8 \cdot 10^{-5}$	$2.0 \cdot 10^{-4}$	$3.8 \cdot 10^{-4}$	$2.9 \cdot 10^{-4}$	$2.1 \cdot 10^{-4}$	$4.0 \cdot 10^{-4}$	$1.6 \cdot 10^{-4}$	$4.0 \cdot 10^{-4}$	$2.8 \cdot 10^{-4}$
E_{LA}^{B}	$8.8 \cdot 10^{-5}$	$2.2 \cdot 10^{-3}$	$7.8 \cdot 10^{-4}$	$2.3 \cdot 10^{-3}$	$4.3 \cdot 10^{-3}$	$3.3 \cdot 10^{-3}$	$2.3 \cdot 10^{-2}$	$1.5 \cdot 10^{-3}$	$4.5 \cdot 10^{-3}$	$1.5 \cdot 10^{-3}$	$1.0 \cdot 10^{-3}$
V_{LA}^{0}	$1.1 \cdot 10^{-7}$	$8.3 \cdot 10^{-7}$	$4.1 \cdot 10^{-7}$	$8.2 \cdot 10^{-7}$	$8.3 \cdot 10^{-7}$	$8.6 \cdot 10^{-7}$	$8.7 \cdot 10^{-7}$	$1.2 \cdot 10^{-6}$	$4.3 \cdot 10^{-7}$	$1.2 \cdot 10^{-6}$	$1.0 \cdot 10^{-6}$
E_{LV}^{A}	$1.3 \cdot 10^{-3}$	$7.9 \cdot 10^{-3}$	$2.9 \cdot 10^{-3}$	$8.3 \cdot 10^{-3}$	$1.7 \cdot 10^{-2}$	$1.2 \cdot 10^{-2}$	$1.2 \cdot 10^{-1}$	$4.5 \cdot 10^{-2}$	$5.2 \cdot 10^{-1}$	$4.5 \cdot 10^{-2}$	$2.9 \cdot 10^{-2}$
E_{LV}^{B}	$3.8 \cdot 10^{-4}$	$1.0 \cdot 10^{-2}$	$3.5 \cdot 10^{-3}$	$1.1 \cdot 10^{-2}$	$2.0 \cdot 10^{-2}$	$1.5 \cdot 10^{-2}$	$1.2 \cdot 10^{-1}$	$1.4 \cdot 10^{-2}$	$2.9 \cdot 10^{-1}$	$1.4 \cdot 10^{-2}$	$9.8 \cdot 10^{-3}$
V_{LV}^{0}	$4.5 \cdot 10^{-7}$	$2.0 \cdot 10^{-6}$	$1.2 \cdot 10^{-6}$	$2.0 \cdot 10^{-6}$	$1.9 \cdot 10^{-6}$	$2.0 \cdot 10^{-6}$	$2.1 \cdot 10^{-6}$	$2.8 \cdot 10^{-6}$	$1.1 \cdot 10^{-6}$	$2.8 \cdot 10^{-6}$	$2.5 \cdot 10^{-6}$
E_{RA}^{A}	$8.9 \cdot 10^{-4}$	$7.1 \cdot 10^{-4}$	$1.3 \cdot 10^{-3}$	$7.2 \cdot 10^{-4}$	$6.5 \cdot 10^{-4}$	$7.1 \cdot 10^{-4}$	$5.5 \cdot 10^{-4}$	$4.1 \cdot 10^{-4}$	$3.5 \cdot 10^{-4}$	$4.1 \cdot 10^{-4}$	$3.4 \cdot 10^{-4}$
E_{RA}^{B}	$6.4 \cdot 10^{-3}$	$2.6 \cdot 10^{-3}$	$4.8 \cdot 10^{-3}$	$2.5 \cdot 10^{-3}$	$2.3 \cdot 10^{-3}$	$2.5 \cdot 10^{-3}$	$1.6 \cdot 10^{-3}$	$1.4 \cdot 10^{-3}$	$2.7 \cdot 10^{-4}$	$1.4 \cdot 10^{-3}$	$7.9 \cdot 10^{-4}$
V_{RA}^{0}	$3.7 \cdot 10^{-7}$	$2.5 \cdot 10^{-6}$	$1.6 \cdot 10^{-6}$	$2.5 \cdot 10^{-6}$	$2.8 \cdot 10^{-6}$	$2.7 \cdot 10^{-6}$	$3.2 \cdot 10^{-6}$	$4.5 \cdot 10^{-6}$	$1.6 \cdot 10^{-6}$	$4.5 \cdot 10^{-6}$	$3.9 \cdot 10^{-6}$
E_{RV}^{A}	$2.3 \cdot 10^{-2}$	$4.9 \cdot 10^{-2}$	$4.2 \cdot 10^{-1}$	$4.9 \cdot 10^{-2}$	$4.5 \cdot 10^{-2}$	$4.8 \cdot 10^{-2}$	$3.9 \cdot 10^{-2}$	$3.2 \cdot 10^{-2}$	$1.7 \cdot 10^{-2}$	$3.2 \cdot 10^{-2}$	$2.4 \cdot 10^{-2}$
E_{RV}^{B}	$2.7 \cdot 10^{-2}$	$1.5 \cdot 10^{-2}$	$2.6 \cdot 10^{-1}$	$1.5 \cdot 10^{-2}$	$1.2 \cdot 10^{-2}$	$1.3 \cdot 10^{-2}$	$8.9 \cdot 10^{-3}$	$7.2 \cdot 10^{-3}$	$1.9 \cdot 10^{-3}$	$7.2 \cdot 10^{-3}$	$4.5 \cdot 10^{-3}$
V_{RV}^{0}	$1.7 \cdot 10^{-6}$	$1.5 \cdot 10^{-5}$	$8.0 \cdot 10^{-6}$	$1.5 \cdot 10^{-5}$	$1.7 \cdot 10^{-5}$	$1.6 \cdot 10^{-5}$	$2.0 \cdot 10^{-5}$	$2.6 \cdot 10^{-5}$	$1.1 \cdot 10^{-5}$	$2.6 \cdot 10^{-5}$	$2.3 \cdot 10^{-5}$
R_{min}	$3.6 \cdot 10^{-4}$	$2.0 \cdot 10^{-3}$	$5.1 \cdot 10^{-4}$	$1.4 \cdot 10^{-4}$	$1.2 \cdot 10^{-4}$	$1.3 \cdot 10^{-4}$	$5.4 \cdot 10^{-4}$	$2.8 \cdot 10^{-4}$	$8.9 \cdot 10^{-4}$	$4.2 \cdot 10^{-4}$	$2.3 \cdot 10^{-4}$
R_{max}	$2.0 \cdot 10^{-9}$	$9.1 \cdot 10^{-10}$	$2.8 \cdot 10^{-10}$	$2.6 \cdot 10^{-10}$	$2.0 \cdot 10^{-10}$	$2.2 \cdot 10^{-10}$	$1.3 \cdot 10^{-9}$	$6.8 \cdot 10^{-10}$	$5.4 \cdot 10^{-10}$	$1.1 \cdot 10^{-9}$	$4.9 \cdot 10^{-10}$
R_{AR}^{SYS}	$1.8 \cdot 10^{-3}$	$6.2 \cdot 10^{-3}$	$2.9 \cdot 10^{-3}$	$6.1 \cdot 10^{-3}$	$6.3 \cdot 10^{-3}$	$6.4 \cdot 10^{-3}$	$2.2 \cdot 10^{-2}$	$4.6 \cdot 10^{-1}$	$1.1 \cdot 10^{-1}$	$4.6 \cdot 10^{-1}$	$6.7 \cdot 10^{-1}$
C_{AR}^{SYS}	$3.1 \cdot 10^{-4}$	$2.2 \cdot 10^{-3}$	$6.6 \cdot 10^{-4}$	$2.2 \cdot 10^{-3}$	$2.7 \cdot 10^{-3}$	$2.5 \cdot 10^{-3}$	$8.6 \cdot 10^{-3}$	$1.2 \cdot 10^{-1}$	$2.5 \cdot 10^{-2}$	$1.2 \cdot 10^{-1}$	$1.0 \cdot 10^{-1}$
L_{AR}^{SYS}	$6.6 \cdot 10^{-12}$	$2.9 \cdot 10^{-11}$	$1.2 \cdot 10^{-11}$	$3.0 \cdot 10^{-11}$	$5.5 \cdot 10^{-11}$	$4.2 \cdot 10^{-11}$	$3.9 \cdot 10^{-10}$	$3.8 \cdot 10^{-8}$	$1.3 \cdot 10^{-9}$	$3.7 \cdot 10^{-8}$	$2.8 \cdot 10^{-9}$
R_{C}^{SYS}	$2.5 \cdot 10^{-6}$	$1.0 \cdot 10^{-5}$	$4.5 \cdot 10^{-6}$	$9.8 \cdot 10^{-6}$	$9.5 \cdot 10^{-6}$	$9.7 \cdot 10^{-6}$	$3.1 \cdot 10^{-5}$	$6.3 \cdot 10^{-4}$	$1.4 \cdot 10^{-4}$	$6.3 \cdot 10^{-4}$	$9.2 \cdot 10^{-4}$
C_{C}^{SYS}	$1.8 \cdot 10^{-6}$	$5.5 \cdot 10^{-6}$	$3.7 \cdot 10^{-6}$	$5.4 \cdot 10^{-6}$	$5.8 \cdot 10^{-6}$	$5.9 \cdot 10^{-6}$	$5.1 \cdot 10^{-6}$	$6.5 \cdot 10^{-6}$	$2.0 \cdot 10^{-6}$	$6.5 \cdot 10^{-6}$	$5.4 \cdot 10^{-6}$
R_{VEN}^{SYS}	$6.4 \cdot 10^{-2}$	$8.2 \cdot 10^{-1}$	$3.4 \cdot 10^{-1}$	$8.1 \cdot 10^{-1}$	$7.4 \cdot 10^{-1}$	$8.0 \cdot 10^{-1}$	$5.6 \cdot 10^{-1}$	$4.0 \cdot 10^{-1}$	$1.2 \cdot 10^{-1}$	$4.0 \cdot 10^{-1}$	$2.5 \cdot 10^{-1}$
C_{VEN}^{SYS}	$6.1 \cdot 10^{-3}$	$3.8 \cdot 10^{-2}$	$1.8 \cdot 10^{-2}$	$3.8 \cdot 10^{-2}$	$3.5 \cdot 10^{-2}$	$3.8 \cdot 10^{-2}$	$3.0 \cdot 10^{-2}$	$4.4 \cdot 10^{-2}$	$1.2 \cdot 10^{-2}$	$4.4 \cdot 10^{-2}$	$4.1 \cdot 10^{-2}$
L_{VEN}^{SYS}	$1.6 \cdot 10^{-10}$	$5.7 \cdot 10^{-11}$	$3.0 \cdot 10^{-11}$	$5.8 \cdot 10^{-11}$	$5.1 \cdot 10^{-11}$	$5.5 \cdot 10^{-11}$	$4.9 \cdot 10^{-11}$	$5.2 \cdot 10^{-11}$	$7.8 \cdot 10^{-12}$	$5.2 \cdot 10^{-11}$	$4.1 \cdot 10^{-11}$
R_{AR}^{PUL}	$2.3 \cdot 10^{-3}$	$7.8 \cdot 10^{-2}$	$2.8 \cdot 10^{-2}$	$8.7 \cdot 10^{-2}$	$9.6 \cdot 10^{-2}$	$9.8 \cdot 10^{-2}$	$6.9 \cdot 10^{-3}$	$8.0 \cdot 10^{-3}$	$2.1 \cdot 10^{-3}$	$8.0 \cdot 10^{-3}$	$5.9 \cdot 10^{-3}$
C_{AR}^{PUL}	$1.4 \cdot 10^{-3}$	$5.2 \cdot 10^{-2}$	$1.0 \cdot 10^{-2}$	$6.1 \cdot 10^{-2}$	$4.1 \cdot 10^{-2}$	$3.5 \cdot 10^{-3}$	$3.0 \cdot 10^{-3}$	$3.2 \cdot 10^{-3}$	$8.2 \cdot 10^{-4}$	$3.2 \cdot 10^{-3}$	$2.5 \cdot 10^{-3}$
L_{AR}^{PUL}	$3.39 \cdot 10^{-10}$	$1.87 \cdot 10^{-08}$	$1.02 \cdot 10^{-09}$	$9.05 \cdot 10^{-09}$	$6.72 \cdot 10^{-10}$	$1.40 \cdot 10^{-10}$	$1.44 \cdot 10^{-10}$	$9.82 \cdot 10^{-11}$	$2.27 \cdot 10^{-11}$	$9.72 \cdot 10^{-11}$	$5.06 \cdot 10^{-11}$
R_{C}^{PUL}	$4.96 \cdot 10^{-04}$	$1.78 \cdot 10^{-02}$	$5.56 \cdot 10^{-03}$	$1.85 \cdot 10^{-02}$	$3.32 \cdot 10^{-02}$	$2.61 \cdot 10^{-02}$	$4.85 \cdot 10^{-03}$	$5.15 \cdot 10^{-03}$	$1.34 \cdot 10^{-03}$	$5.12 \cdot 10^{-03}$	$4.09 \cdot 10^{-03}$
C_{C}^{PUL}	$9.43 \cdot 10^{-05}$	$1.10 \cdot 10^{-03}$	$4.38 \cdot 10^{-04}$	$1.09 \cdot 10^{-03}$	$1.71 \cdot 10^{-03}$	$1.12 \cdot 10^{-03}$	$1.57 \cdot 10^{-03}$	$2.23 \cdot 10^{-03}$	$5.47 \cdot 10^{-04}$	$2.22 \cdot 10^{-03}$	$1.95 \cdot 10^{-03}$
R_{SH}	$6.14 \cdot 10^{-04}$	$2.34 \cdot 10^{-02}$	$7.23 \cdot 10^{-03}$	$2.43 \cdot 10^{-02}$	$4.35 \cdot 10^{-02}$	$3.43 \cdot 10^{-02}$	$4.64 \cdot 10^{-03}$	$5.58 \cdot 10^{-03}$	$1.60 \cdot 10^{-03}$	$5.55 \cdot 10^{-03}$	$4.76 \cdot 10^{-03}$
C_{SH}	$9.71 \cdot 10^{-09}$	$1.25 \cdot 10^{-07}$	$3.95 \cdot 10^{-08}$	$1.31 \cdot 10^{-07}$	$1.43 \cdot 10^{-07}$	$8.38 \cdot 10^{-08}$	$1.16 \cdot 10^{-07}$	$1.52 \cdot 10^{-07}$	$3.76 \cdot 10^{-08}$	$1.51 \cdot 10^{-07}$	$1.26 \cdot 10^{-07}$
R_{VEN}^{PUL}	$5.11 \cdot 10^{-04}$	$1.33 \cdot 10^{-02}$	$4.37 \cdot 10^{-03}$	$1.39 \cdot 10^{-02}$	$2.73 \cdot 10^{-02}$	$2.02 \cdot 10^{-02}$	$1.61 \cdot 10^{-01}$	$1.36 \cdot 10^{-02}$	$3.44 \cdot 10^{-03}$	$1.35 \cdot 10^{-02}$	$1.02 \cdot 10^{-02}$
C_{VEN}^{PUL}	$7.07 \cdot 10^{-04}$	$2.73 \cdot 10^{-03}$	$1.79 \cdot 10^{-03}$	$2.73 \cdot 10^{-03}$	$3.11 \cdot 10^{-03}$	$2.99 \cdot 10^{-03}$	$5.53 \cdot 10^{-03}$	$8.08 \cdot 10^{-03}$	$2.23 \cdot 10^{-03}$	$8.04 \cdot 10^{-03}$	$7.24 \cdot 10^{-03}$
L_{VEN}^{PUL}	$4.69 \cdot 10^{-10}$	$1.34 \cdot 10^{-09}$	$2.77 \cdot 10^{-10}$	$1.42 \cdot 10^{-09}$	$3.53 \cdot 10^{-09}$	$2.32 \cdot 10^{-09}$	$2.37 \cdot 10^{-08}$	$8.32 \cdot 10^{-09}$	$4.47 \cdot 10^{-08}$	$8.31 \cdot 10^{-09}$	$6.87 \cdot 10^{-09}$

Table 3.7: Total Sobol' indices for the model lumped-parameters by considering the available clinical data as model outputs.

4 | Numerical simulations

4.1. Patent foramen ovale results

In this subsection we review the results obtained by introducing the patent foramen ovale in the lumped-parameter model.
According to the pulmonary compartment constriction introduced, the pulmonary arterial resistance and inductance increase, whereas its capacitance decreases.
All these three parameter changes make the right heart struggle more to pump blood. As a consequence, its chamber pressures increase and in particular the right atrium pressure exceeds the left one during the atrial relaxation, opening the foramen, Figure 4.1.

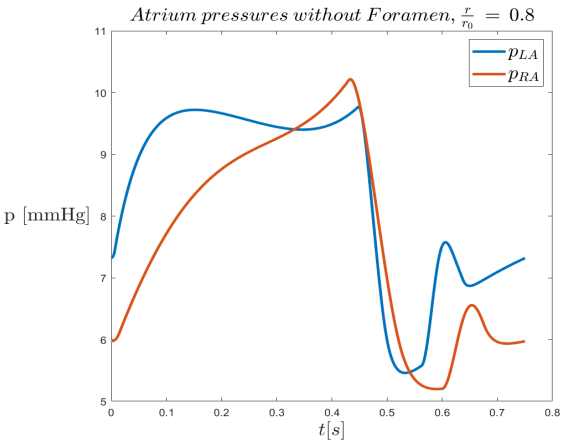

Figure 4.1: Pulmonary arterial constriction simulated in an adult male without the foramen.

As it can be seen from the Figure 4.2(a), increasing the radius of the foramen leads to an increase in the right-to-left shunt phenomenon. More blood is pushed from the right atrium to the left atrium within each cardiac cycle. The blood volume passed to the left ventricle, which is subsequently pumped into the systemic circulation, increases. In contrast the right ventricle lose more blood as the orifice gets bigger and, as a direct consequence pumps less blood into the pulmonary circulation. Less blood is getting

oxygenated in the lungs.
The ratio between the medium flow of the pulmonary circulation and that of the systemic circulation Q_P/Q_S, decreases accordingly (Table 4.1). The two circulation medium flows are calculated as:

$$\begin{cases} Q_P = \dfrac{\int_0 T_{HB} Q_{PV}(t)dt}{T_{HB}} \\ Q_S = \dfrac{\int_0 T_{HB} Q_{AV}(t)dt}{T_{HB}} \end{cases} \tag{4.1}$$

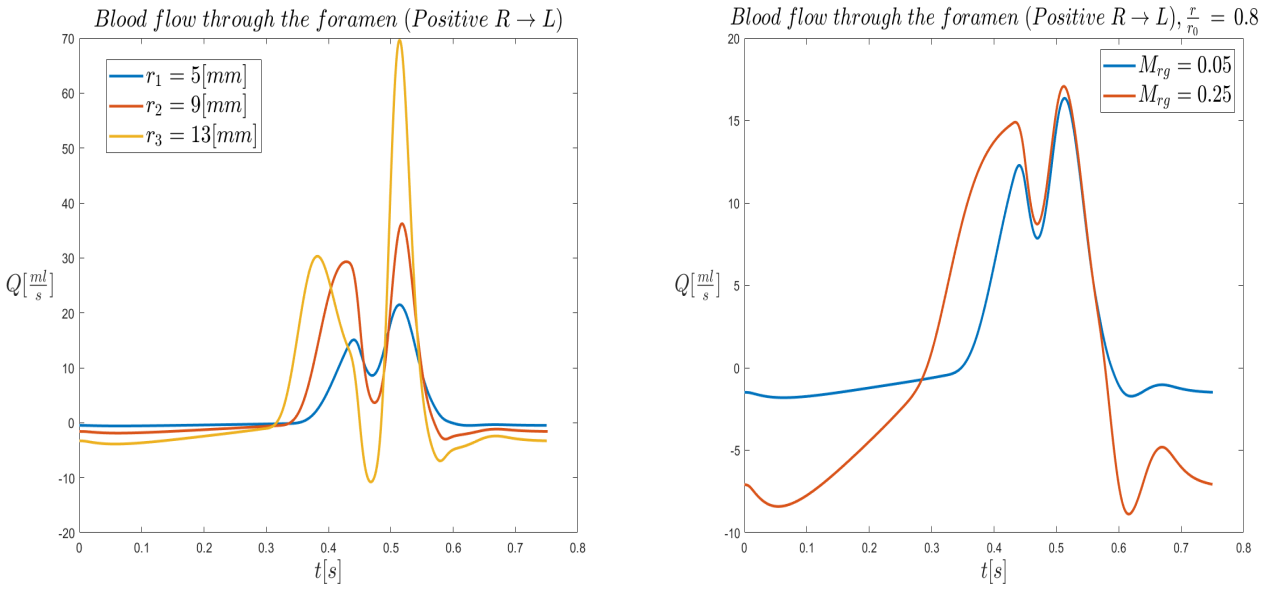

(a) (b)

Figure 4.2: Foramen model simulations: (a) Shunting blood flow curve varying the orifice radius; (b)Shunting blood flow curve varying the regurgitation factor

Table 4.1: Foramen model results

Foramen radius	$\frac{Q_P}{Q_S}$
$r_{small} = 5.0\ mm$	0.9598
$r_{medium} = 9.0\ mm$	0.9442
$r_{large} = 13.0\ mm$	0.9438

By increasing the regurgitation factor M_{REG} the backflow shunt (left to right) expands, Figure 4.2(b). The one directionality nature of the valve is preserved. In fact, left to right pressure gradients (during different parts of the heartbeat) are considerably bigger than right to left ones, but in the prediction of the model the regurgitating backflow (left to right) keeps smaller than the right to left allowed normally by the foramen.

4.2. PAPVR: atrium case results

In this subsection we review the results of the model implementing the PAPVR for the atrium case. The curves of the flowing blood through the anomalous veins are almost identical in single and double anomalous veins cases.
By integrating these curves it results that the blood volume flowed in a heartbeat through the anomalous veins V^{HB}_{VEIN} slightly decreases moving from the single to the doubles case. In contrast with this behaviour, both the blood flow and the volume passed through the anomalous veins increase a lot in the three anomalous veins scenario, Figure 4.3.

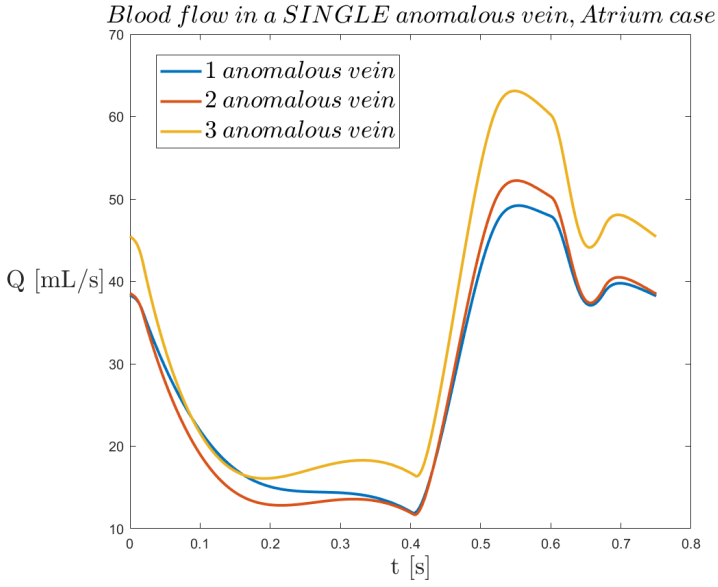

Figure 4.3: Anomalous vein blood flow curves.

As a direct consequence, if the passing volumes in the anomalous veins are only increasing or just slightly decreasing, the shunting phenomenon to the right atrium escalates with the growing number of anomalous veins.
This can be confirmed by the different shunt measures reported in the Table 4.2. Q_{SHUNT} represents the total blood flow moving from the lungs to the right atrium through the

anomalous veins:

$$Q_{SHUNT} = \sum_{j=1}^{Nj} Q_{VEIN,j}^{PUL} \tag{4.2}$$

Table 4.2: PAPVR: atrium case shunt measures

Case	$\frac{Q_P}{Q_S}$	$\frac{Q_{SHUNT}}{CO}$	$V_{VEIN}^{HB}\ [ml]$
1 *anomalous vein*	1.3362	0.3451	20.83
2 *anomalous veins*	1.7276	0.7380	20.7
3 *anomalous veins*	2.5696	1.5756	25.1

The right ventricle gets progressively overloaded by increasing the anomalous veins number. It gets filled by more blood, received by the lungs, and as a consequence its pressure rises.
In contrast the left ventricle is deprived of the blood it should receive, and consequently its blood volume and pressure decrease, Figure 4.4.

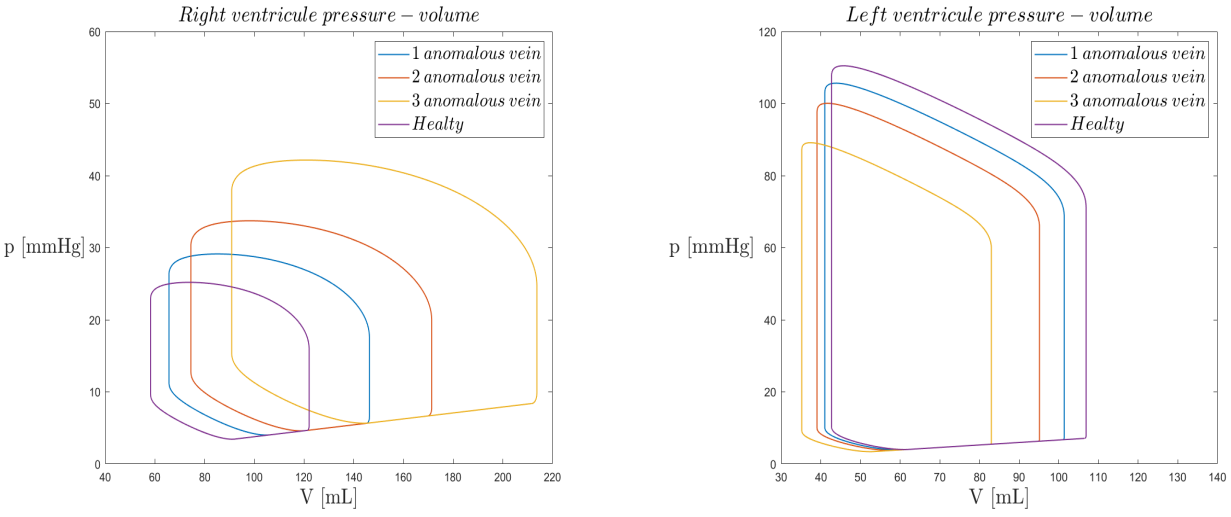

(a) (b)

Figure 4.4: PAPVR atrium case simulation: (a) right ventricular pressure volume loop; (b)left ventricular pressure volume loop

The increased blood volume coming from the right ventricle puts under stress all the pulmonary circulation vessels, straining them and potentially, damaging them.

4.3. PAPVR: superior vena cava case results

In this subsection we review the results of the model implementing the PAPVR for the superior vena cava case. As in the atrium case the curves of the flowing blood through the anomalous veins are almost identical in single and double anomalous veins cases.
In this case, however, the blood volume flowed in a heartbeat through the anomalous veins, obtained by integrating over a heartbeat the blood flow curves, slightly increase moving from the single to the double case.
As in the atrium case, both the blood flow and the volume passed through the anomalous veins increase a lot in the three anomalous veins scenario.

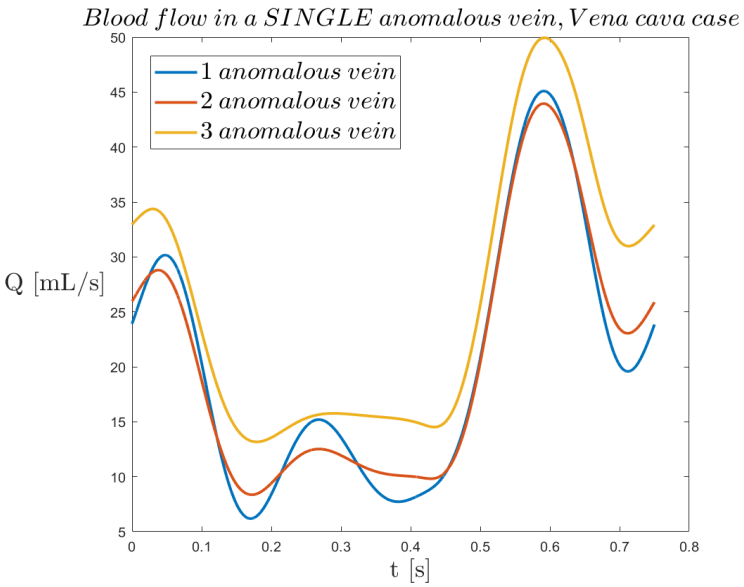

Figure 4.5: Anomalous vein blood flow curves.

The shunting measures globally decreases with respect to the atrium case, Tables 4.2 4.3. This result was expected because by ascending the systemic venous system the pressure is naturally higher.

Case	$\frac{Q_P}{Q_S}$	$\frac{Q_{SHUNT}}{CO}$	V^{HB}_{VEIN} $[ml]$
1 *anomalous vein*	1.2475	0.2568	15.16
2 *anomalous veins*	1.5467	0.5576	15.34
3 *anomalous veins*	2.2241	1.2329	19.31

Table 4.3: PAPVR: superior vena cava case shunt measures

As in the atrium case, by increasing the anomalous veins number, the right ventricle gets progressively overloaded, whereas the left ventricle receives less blood, Figure 4.6.

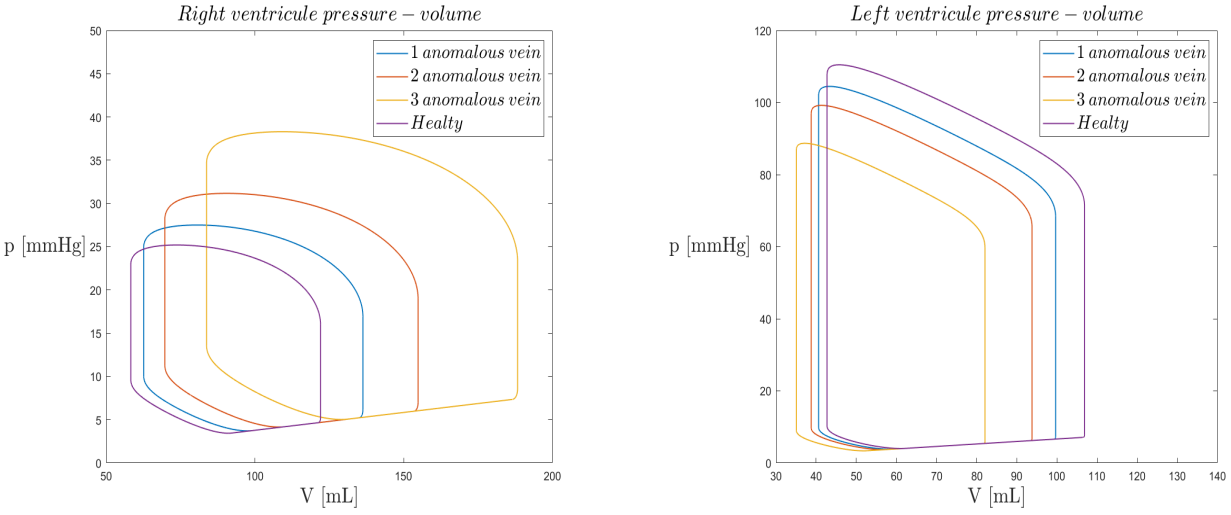

(a) (b)

Figure 4.6: PAPVR superior vena cava case simulation: (a) right ventricular pressure volume loop; (b)left ventricular pressure volume loop

4.4. ASD patient

In this subsection we review the results of the model calibration for the ASD patient. The obtained calibrated model for the ASD patient has a mean squared relative error of 9.8×10^{-3}. Although the calibrated model correctly gauges all the pressure, it slightly overestimates the circulation blood fluxes, Table 4.4.

Table 4.4: Output comparison for ASD model calibration

Acronym	*Clinical value*	*Model output*	*Units of measure*
p_{RA}^{mean}	15	18.36	$mmHg$
p_{RV}^{max}	45	49.15	$mmHg$
p_{RV}^{min}	15	12.26	$mmHg$
PAP_{max}	50	47.0	$mmHg$
PAP_{min}	20	19.63	$mmHg$
PAP_{mean}	30	30.83	$mmHg$
PWP_{mean}	17	18.76	$mmHg$
p_{LV}^{max}	98	98.56	$mmHg$
p_{LV}^{min}	17	14.07	$mmHg$
SAP_{max}	97	98.07	$mmHg$
SAP_{min}	70	69.9	$mmHg$
SAP_{mean}	85	83.89	$mmHg$
Q_P	7.86	9.44	$l \times min^{-1}$
Q_S	3.09	3.73	$l \times min^{-1}$

Table 4.5: ASD patient: model parameters significant changes

Acronym	*Healty reference*	*ASD patient*	*Units of measure*
R_{AR}^{PUL}	0.0714	0.079	$mmHg\ s\ ml^{-1}$
R_{VEN}^{PUL}	0.0375	0.003	$mmHg\ s\ ml^{-1}$
C_{AR}^{PUL}	6.004	3.095	$ml\ mmHg^{-1}$
R_{VEN}^{SYS}	0.3596	0.2956	$ml\ mmHg^{-1}$
E_{LV}^{A}	2.70	1.50	ml^{-1}
E_{LV}^{B}	0.069	0.14	ml^{-1}
E_{RV}^{A}	0.43	0.6	ml^{-1}
E_{RV}^{B}	0.041	0.08	ml^{-1}

It can be inferred from the measured PVR and from the calibrated pulmonary resistances (Table 4.5) that the patient has small to none significant damage to the pulmonary circulation vessels.
The high ventricular maximal pressures are probably achieved in the calibration process by increasing the passive and active ventricular elastances, Table 4.5.
The resulting atrial septal resistance is quite small, $R_{ASD} = 1.25 \times 10^{-4}$.
As a consequence the septal defect offer no resistance and the atrial pressures match. The two atria works as one common chamber that receive blood from the two circulation venous systems and move it to the ventricles.
Right ventricle receives additional blood coming from the right atrium and as a consequence its maximum pressure is outside its normal healthy range ($15 - 28\ mmHg$).

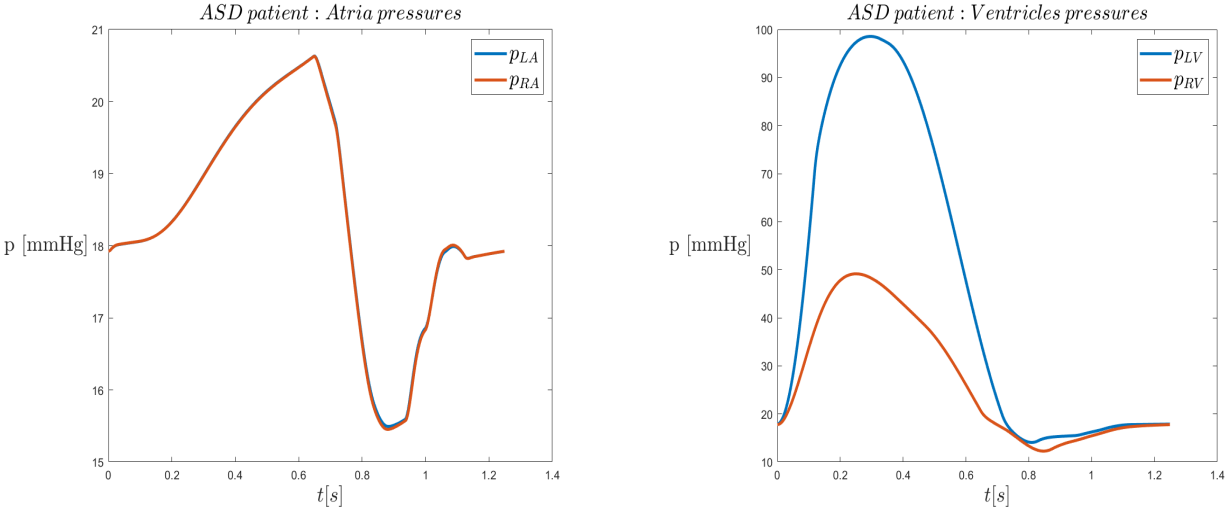

(a) (b)

Figure 4.7: ASD patient chamber pressures: (a) atrial pressures; (b)ventricular pressures

The ventricular volumes estimations are both particularly big, this can be explained by the patient's high rightt ventricular Stroke Volume obtainable from the clinical data:

$$RV_{SV} = \frac{Q_P}{HR} = \frac{7.86l \cdot min^{-1}}{48min^{-1}} = 163.75ml \tag{4.3}$$

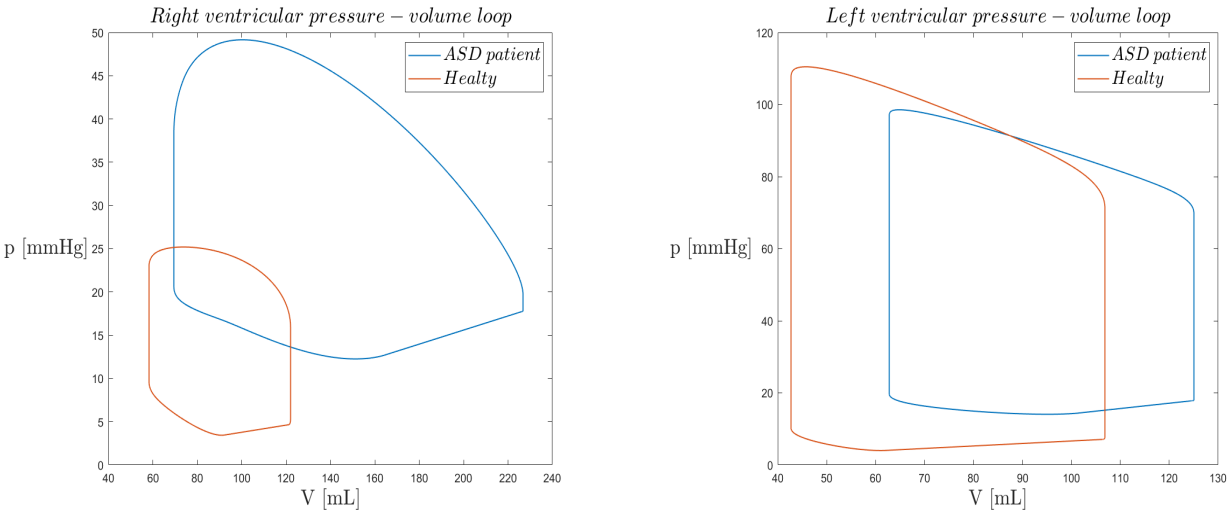

(a) (b)

Figure 4.8: ASD patient ventricular P-V loops: (a) Right ventricle; (b) Left ventricle

The calibrated model predicts some pulmonary venous blood flow return,Figure 4.9. This is a consequence of the low pulmonary venous resistance. Once the pulmonary venous capacitance has gave back the accumulated pressure in the systolic phase, the pulmonary venous pressure starts to drop. Meanwhile the left atrium gets filled with blood and as a consequence its pressure starts to rise. Once this pressure exceeds the pulmonary venous one, if the pulmonary venous resistance is low the blood can flow back into the lungs (Figure 4.11).

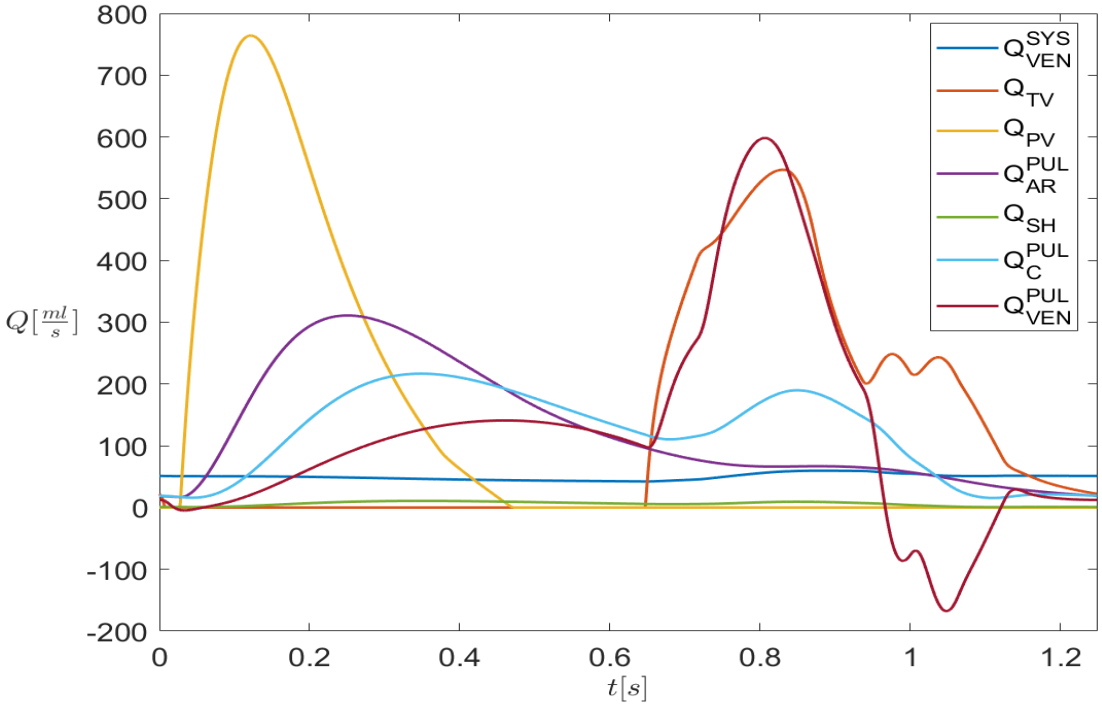

Figure 4.9: ASD patient pulmonary flows.

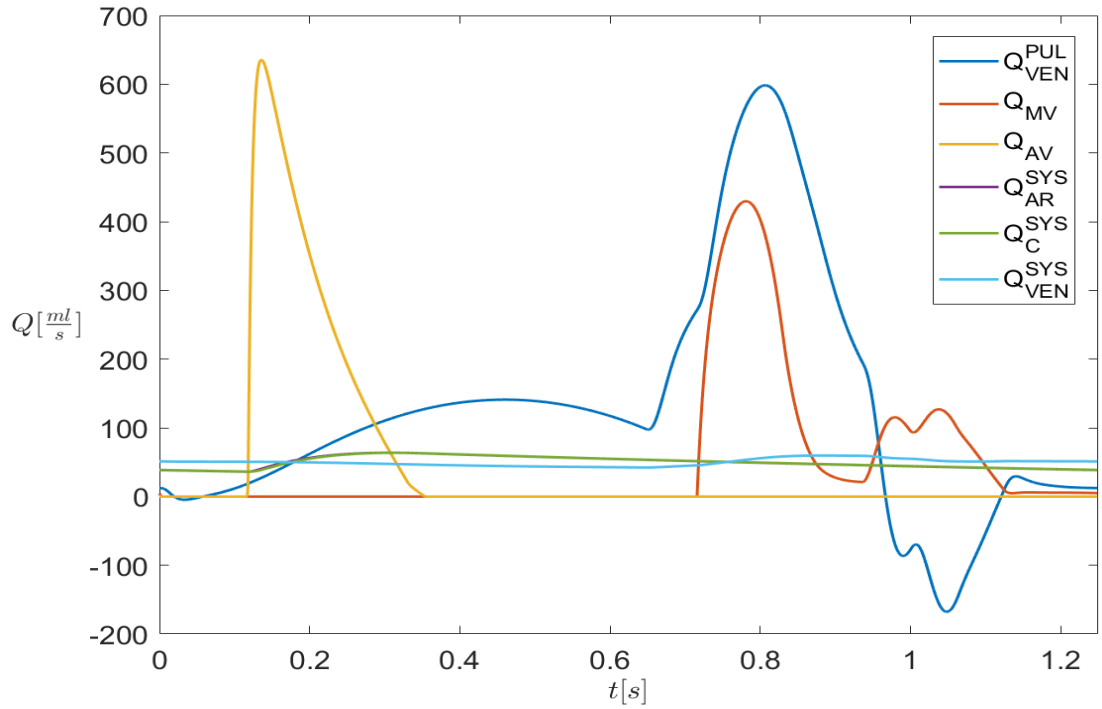

Figure 4.10: ASD patient systemic flows.

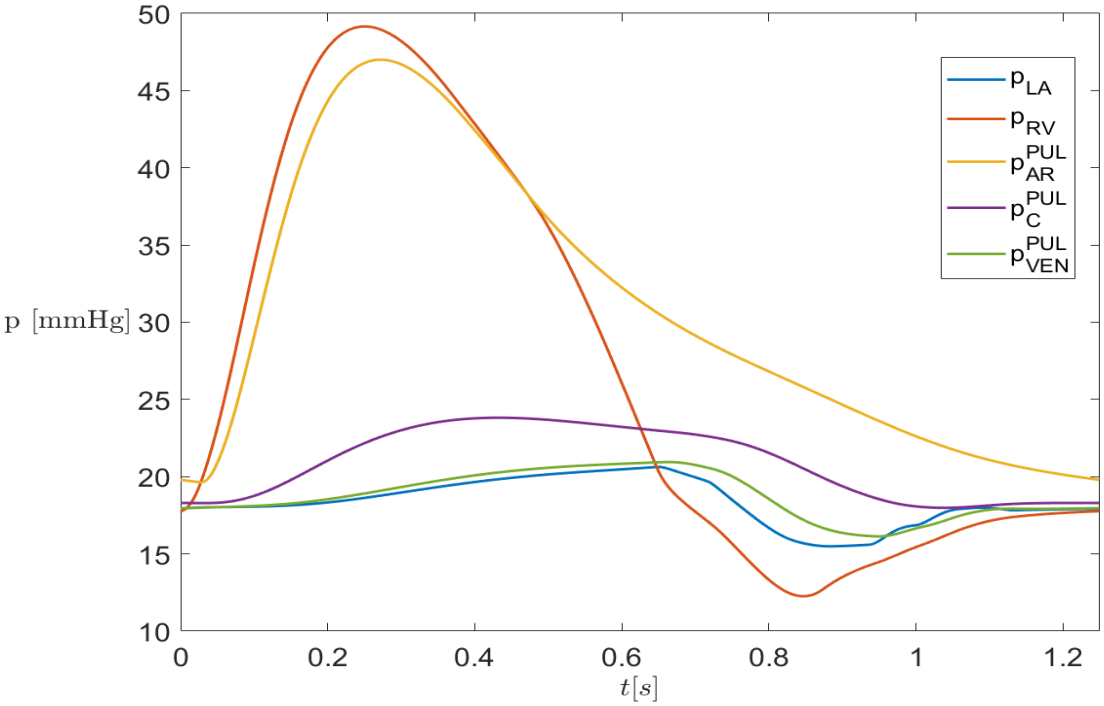

Figure 4.11: ASD patient pulmonary pressures. The now common atria pressure was reported as p_{LA} to highlight the pressures involved in the pulmonary venous return

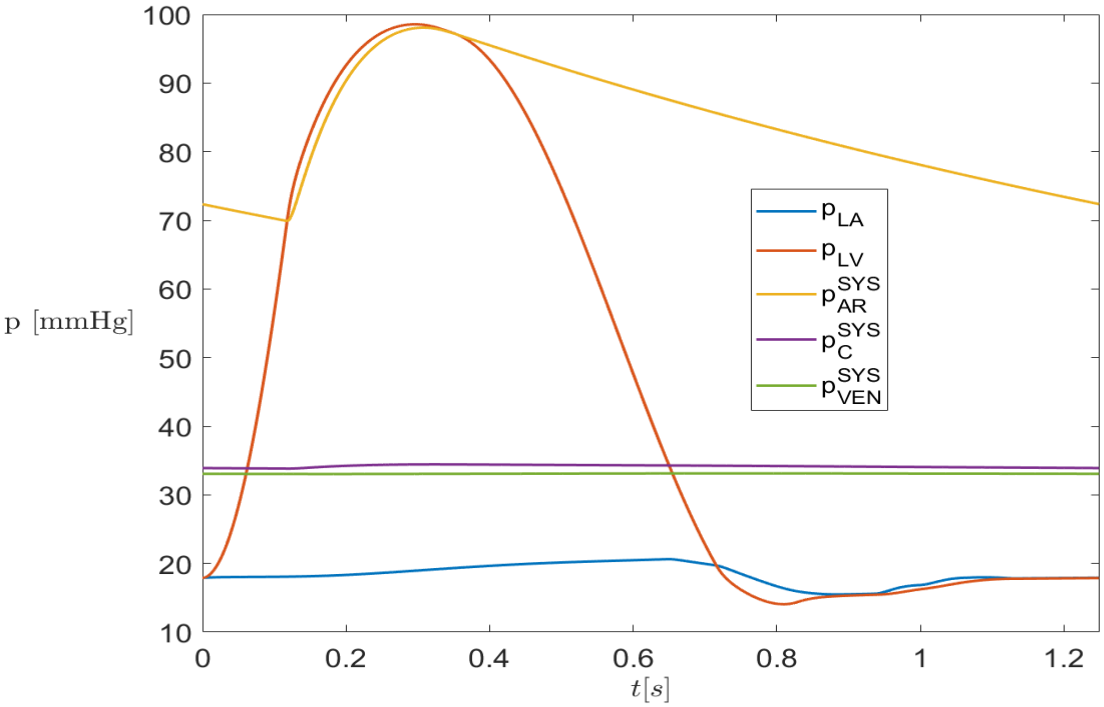

Figure 4.12: ASD patient systemic pressures.

4.5. VSD patient

In this subsection we review the results of the model calibration for the VSD patient. The obtained calibrated model for the VSD patient has a mean squared relative error of 2.77×10^{-2}. Although the model has almost correctly guessed all the pressures and the systemic flux, it has failed to correctly reproduce the pulmonary flux, Table 4.6.

Table 4.6: Output comparison for VSD model calibration

Acronym	*Clinical value*	*Model output*	*Units of measure*
p_{RA}^{mean}	15	13.84	$mmHg$
PAP_{max}	88	82.12	$mmHg$
PAP_{min}	33	37.52	$mmHg$
PAP_{mean}	55	67.29	$mmHg$
PWP_{mean}	30	29.3	$mmHg$
SAP_{max}	75	82	$mmHg$
SAP_{min}	48	45.23	$mmHg$
SAP_{mean}	55	62.34	$mmHg$
Q_P	2.44	3.37	$l \times min^{-1}$
Q_S	2.44	2.52	$l \times min^{-1}$

Table 4.7: VSD patient: model parameters significant changes

Acronym	*Healty reference*	*VSD patient*	*Units of measure*
R_{AR}^{PUL}	0.0714	0.382	$mmHg\ s\ ml^{-1}$
R_{VEN}^{PUL}	0.0375	0.216	$mmHg\ s\ ml^{-1}$
C_{AR}^{PUL}	6.004	0.8124	$ml\ mmHg^{-1}$
R_{VEN}^{SYS}	0.3596	0.3408	$ml\ mmHg^{-1}$
E_{LV}^{A}	2.70	2.569	ml^{-1}
E_{LV}^{B}	0.069	0.086	ml^{-1}
E_{RV}^{A}	0.43	0.716	ml^{-1}
E_{RV}^{B}	0.041	0.35	ml^{-1}

The resulting ventricular septal resistance is again quite small, $R_{VSD} = 8.75 \times 10^{-3}$. As in the atrial case the septal defect offer no resistance and the ventricular pressures match (Figure 4.13). The two ventricles works as a single chamber that receive blood

from the atria and push it in the systemic and pulmonary arterial compartments
Consequently the left ventricular pressure is lower than usual, whereas the right one is higher. This result could be inquired by the available high PAP_{max} clinical data.
Due to the high minimal right ventricular pressure, increased by the VSD, blood struggles to move downward from the right atrium to the right ventricle. As a consequence the right atrial mean pressure P_{RA}^{mean} is higher than in healthy patients ($-1,8\ mmHg$). The left to right ventricular shunt overloads the pulmonary circulation and as a consequence the left atrium.

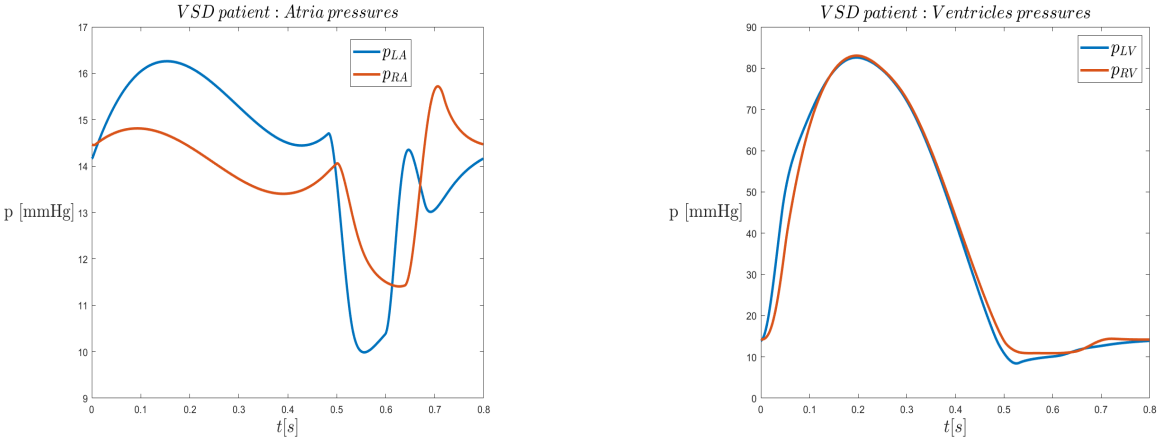

(a) (b)

Figure 4.13: VSD patient chamber pressures: (a) atrial pressures; (b)ventricular pressures

From the pressure-volume loops it can be clearly seen that the right ventricular minimal pressure is higher than in a normal healthy patient.
As soon as the passive filling phase starts blood flows through the septal defect. This make the right ventricular pressure rise faster than in a healthy patient.
In the same fashion in the ventricular contraction blood continues to move through the ventricles.
The (almost) isobaric passive filling and the isovolumetric contraction, typical of the ventricular pressure volume, are no longer visible, especially in the right one.
The right ventricle and pulmonary circulation overload, stimulate over time the body remodeling to rebalance the systemic and the pulmonary blood flows.
As explained in Section 1.5 this is achieved through cellular proliferation in the pulmonary vessels, making them narrower and, as a consequence, increasing their resistance.
The PVR clinical data and the calibrated pulmonary resistances are in fact, several times higher than the healthy ones.

Another important consequence of this body adaptation is probably the important reduction on C_{AR}^{PUL}. The overload repeatedly strained the pulmonary circulation vessels, making them lose their ability to stretch and dilate to store pressure as potential elastic energy. This could explain the big difference between the patient clinical data of maximal and minimal pulmonary arterial pressure.
Due to the high blood volume moving to the right ventricle, it would be expected an important increase in the right ventricular end diastolic volume.
From the pressure-volume loop, however, it is not possible to appreciate this expected behavior. The reason may lie in the opening time of the pulmonary valve. By comparing the flows through the pulmonary valves, it is possible to observe that, given the faster increase in pressure in the right ventricle due to blood shunting, the pulmonary valve opens earlier, effectively relieving the right ventricle and preventing overload , Figure 4.15.

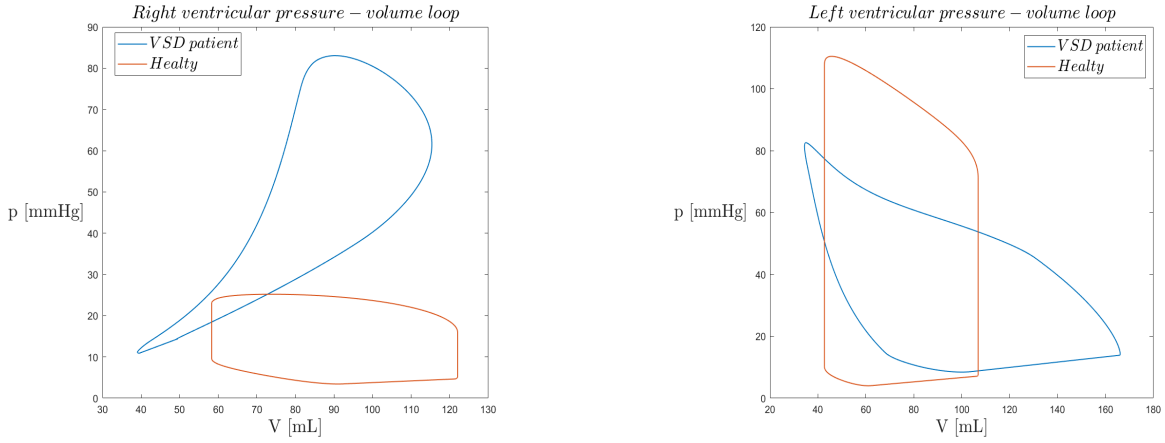

(a) (b)

Figure 4.14: VSD patient ventricular P-V loops: (a) Right ventricle; (b) Left ventricle

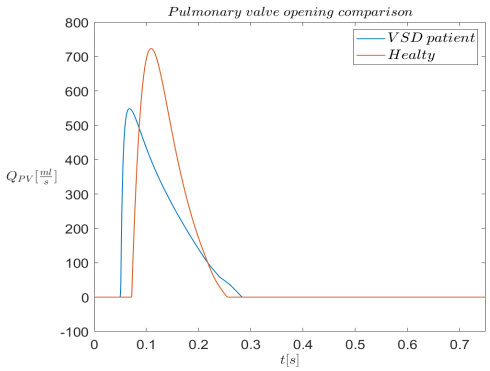

Figure 4.15: Flow through pulmonary valve comparison between VSD patient and healthy reference

Due to the high minimal left and right atrial pressures for the reasons explained before, the distinction between ventricular passive filling and atrial contraction is more visible in the blood flows through the atrioventricular valves (PV and AV), (Figure 4.16, 4.17).

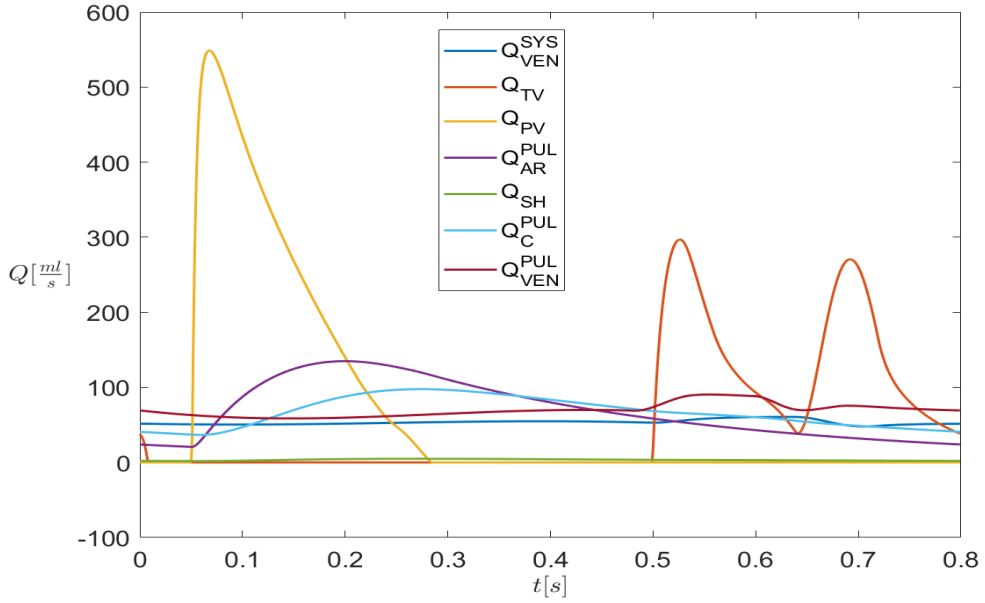

Figure 4.16: VSD patient pulmonary flows.

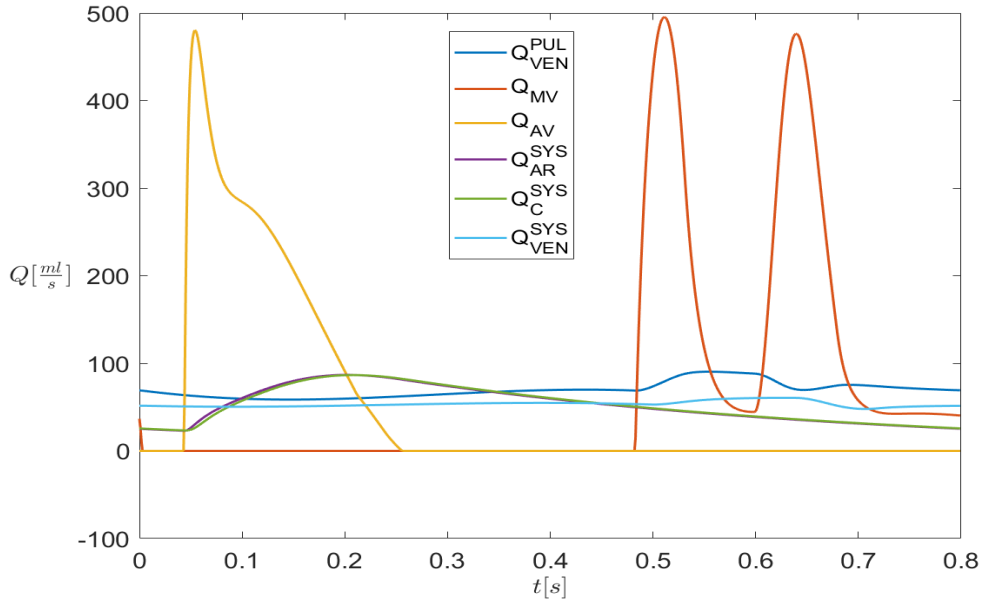

Figure 4.17: VSD patient systemic flows.

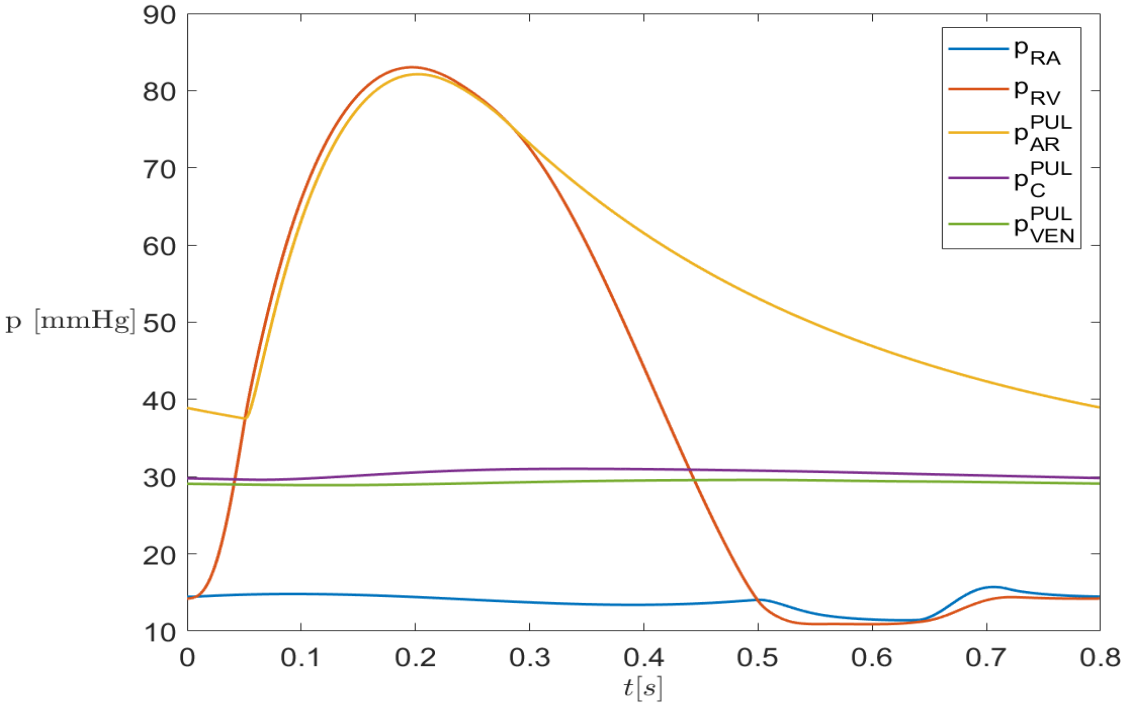

Figure 4.18: VSD patient pulmonary pressures.

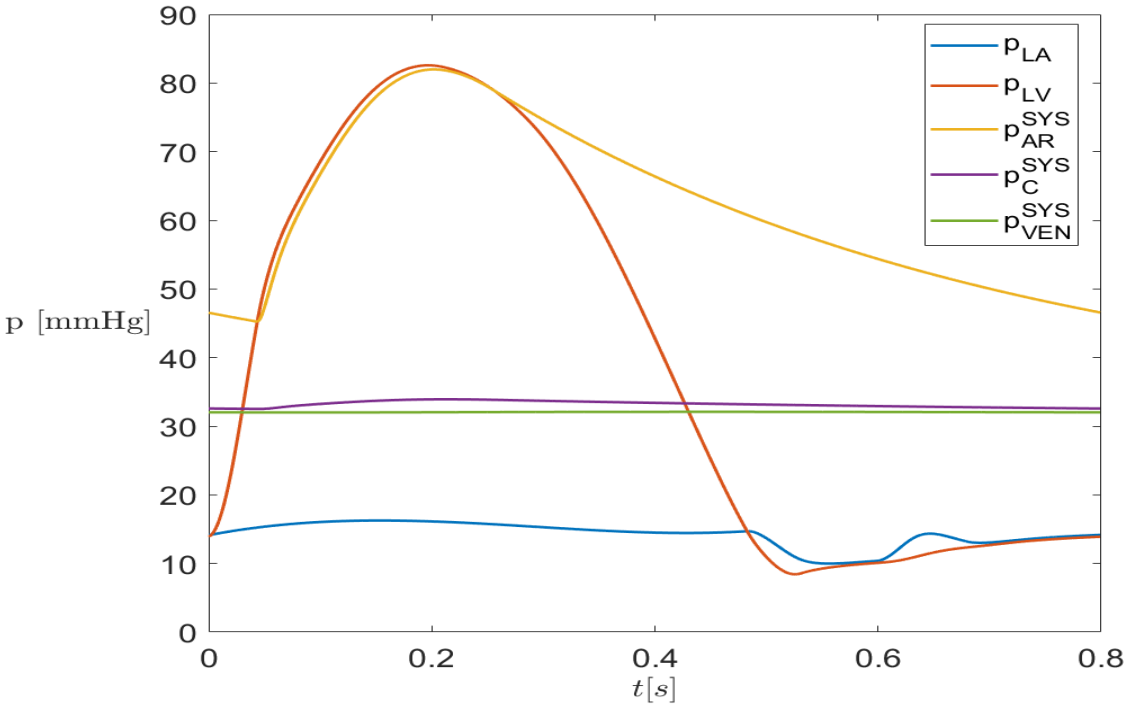

Figure 4.19: VSD patient systemic pressures.

4.6. VSD patient: VD administration (VSD/VD)

In this subsection we review the results obtained in the model calibration for the VSD patient under vasodilatators administration. In this condition the obtained calibrated model for the VSD patient has a mean squared relative error of 1.10×10^{-2}. Fixing the ventricular septal defect resistance obtained in the VSD patient model calibration, a second calibration using the available clinical data of the same patient under vasodilatators administration was performed.

The calibrated model correctly guesses all the pressures except the maximum and mean pulmonary arterial ones, Table 4.8. The pulmonary circulation flow is lower that the available clinical data, but it is still more than two times higher than in the reference healthy condition ($2.09l \cdot min^{-1}$).

The increase in pulmonary blood flow is probably due to the effect of vasodilators, which have significantly reduced pulmonary resistances, Table 4.9.

Table 4.8: Output comparison for VSD/VD model calibration

Acronym	*Clinical value*	*Model output*	*Units of measure*
p_{RA}^{mean}	15	15.41	$mmHg$
PAP_{max}	90	77.56	$mmHg$
PAP_{min}	35	33.73	$mmHg$
PAP_{mean}	64	49.85	$mmHg$
PWP_{mean}	33	32.60	$mmHg$
SAP_{max}	75	79.48	$mmHg$
SAP_{min}	48	43.41	$mmHg$
SAP_{mean}	68	59.84	$mmHg$
Q_P	5.96	4.60	$l \times min^{-1}$
Q_S	1.53	1.29	$l \times min^{-1}$

The passive elastance of the left ventricle greatly increased, meanwhile the passive elastance of the right ventricle increased several times. These result will be discussed in the Section 4.7.

Table 4.9: VSD/VD patient: model parameters significant changes

Acronym	*Healty reference*	*VSD/VD patient*	*Units of measure*
R_{AR}^{PUL}	0.0714	0.152	$mmHg\ s\ ml^{-1}$
R_{VEN}^{PUL}	0.0375	0.143	$mmHg\ s\ ml^{-1}$
C_{AR}^{PUL}	6.004	0.81	$ml\ mmHg^{-1}$
R_{VEN}^{SYS}	0.3596	0.493	$ml\ mmHg^{-1}$
E_{LV}^{A}	2.70	1.92	ml^{-1}
E_{LV}^{B}	0.069	0.109	ml^{-1}
E_{RV}^{A}	0.43	0.575	ml^{-1}
E_{RV}^{B}	0.041	0.336	ml^{-1}

The increased pulmonary blood flow overloads the left atrium, considerably increasing its pressure Figure 4.20.
As a consequence, the blood flow through the mitral valve increases, Figure 4.25.

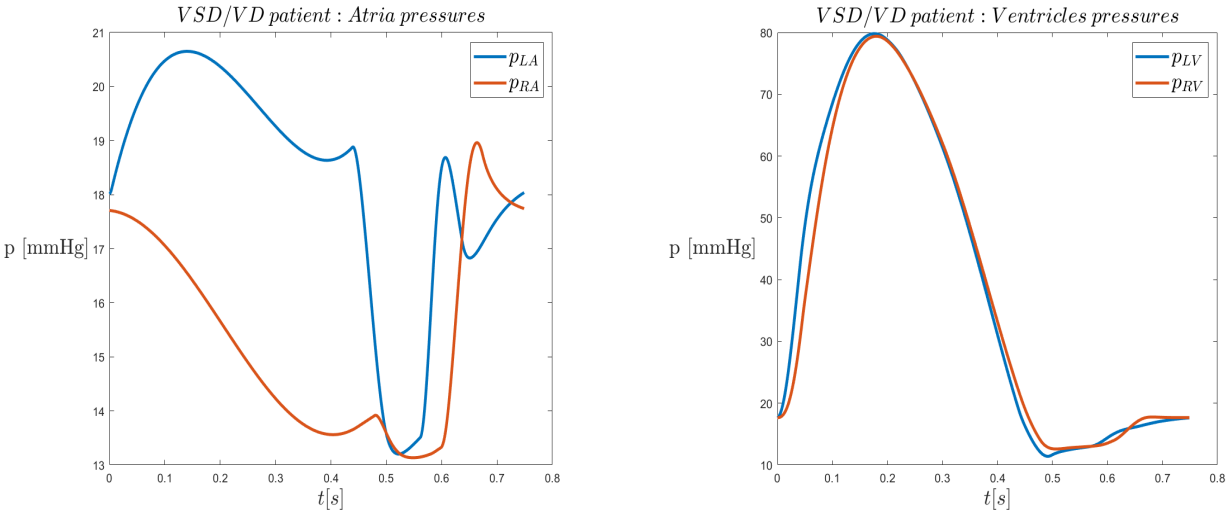

(a) (b)

Figure 4.20: VSD/VD patient chamber pressures: (a) atrial pressures; (b)ventricular pressures

The additional blood moved to the left atrium and subsequently to the left ventricle, is not visible on the left ventricular pressure-volume loop. In fact the left ventricular end diastolic volume is equal to the normal condition.
The blood is probably moved immediately to the right ventricle through the septal defect, increasing the right ventricular end diastolic volume.

Table 4.10: VSD patient: end diastolic volumes comparison

	$VSD\ patient$	$VSD/VD\ patient$	$Unit$
LV_{EDV}	166.13	165.65	ml
RV_{EDV}	115.37	120.30	ml

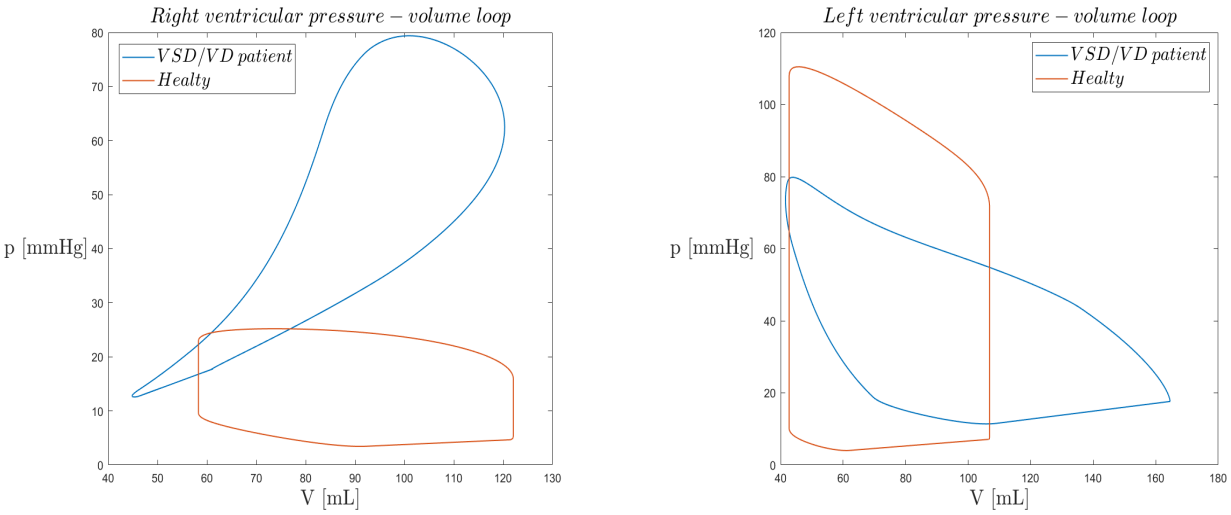

(a) (b)

Figure 4.21: VSD/VD patient ventricular P-V loops: (a) Right ventricle; (b) Left ventricle

The arterial pulmonary blood flow clearly increased due to the lower pulmonary resistance under vasodilatators administration.

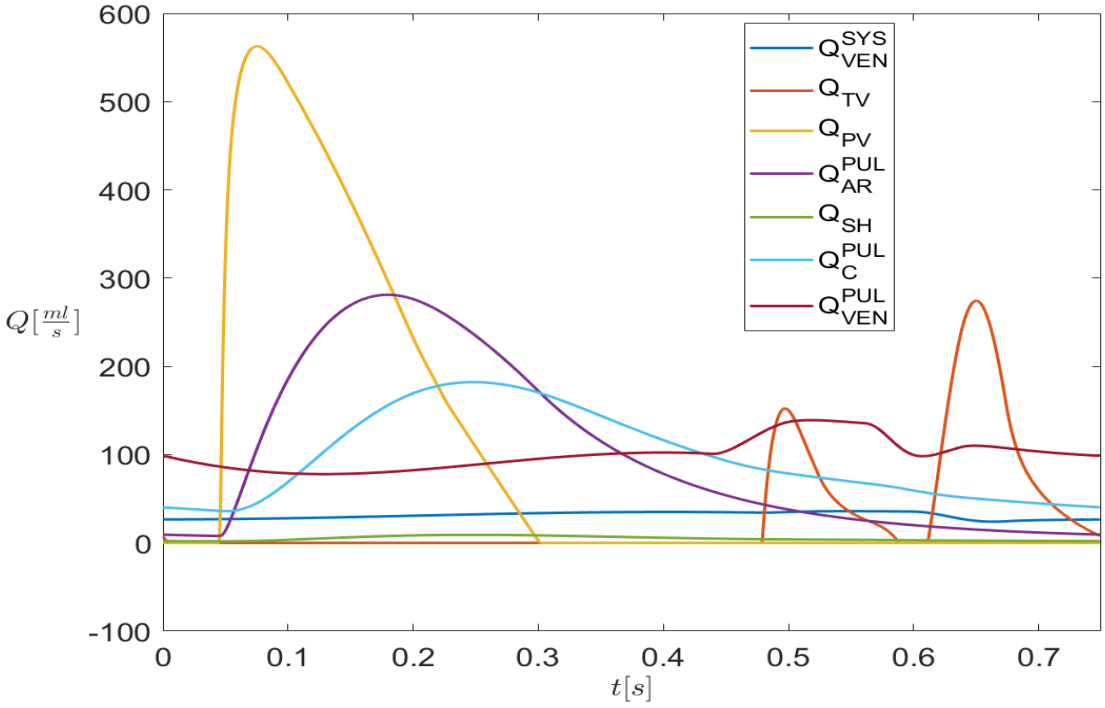

Figure 4.22: VSD/VD patient pulmonary flows.

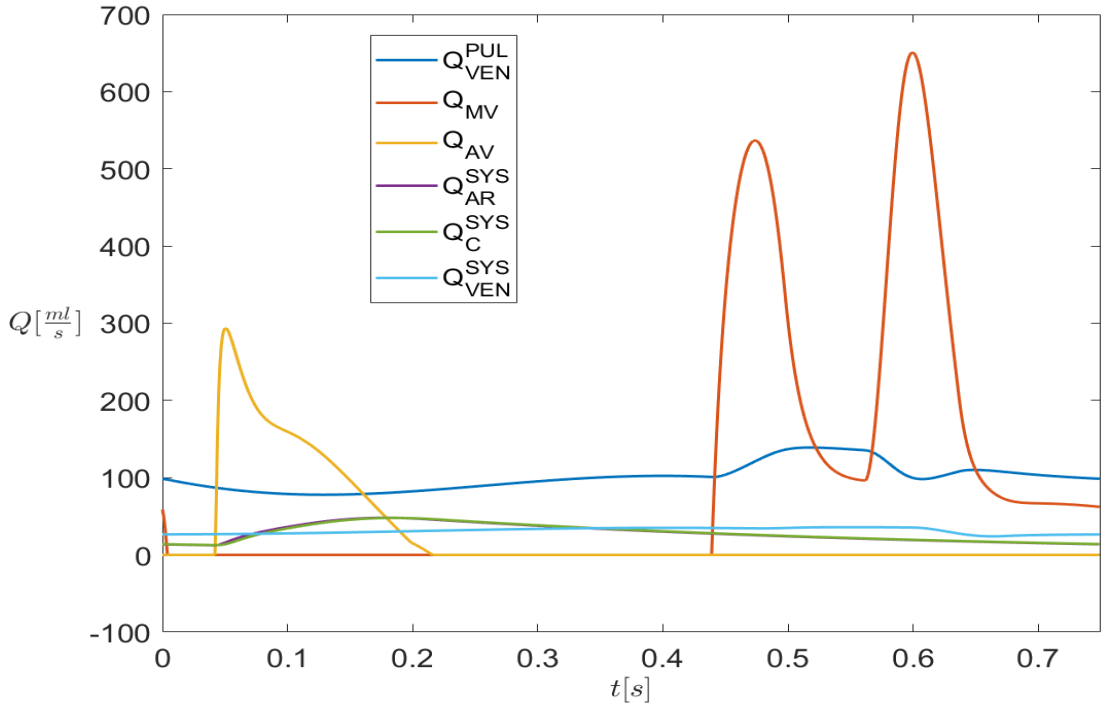

Figure 4.23: VSD/VD patient systemic flows.

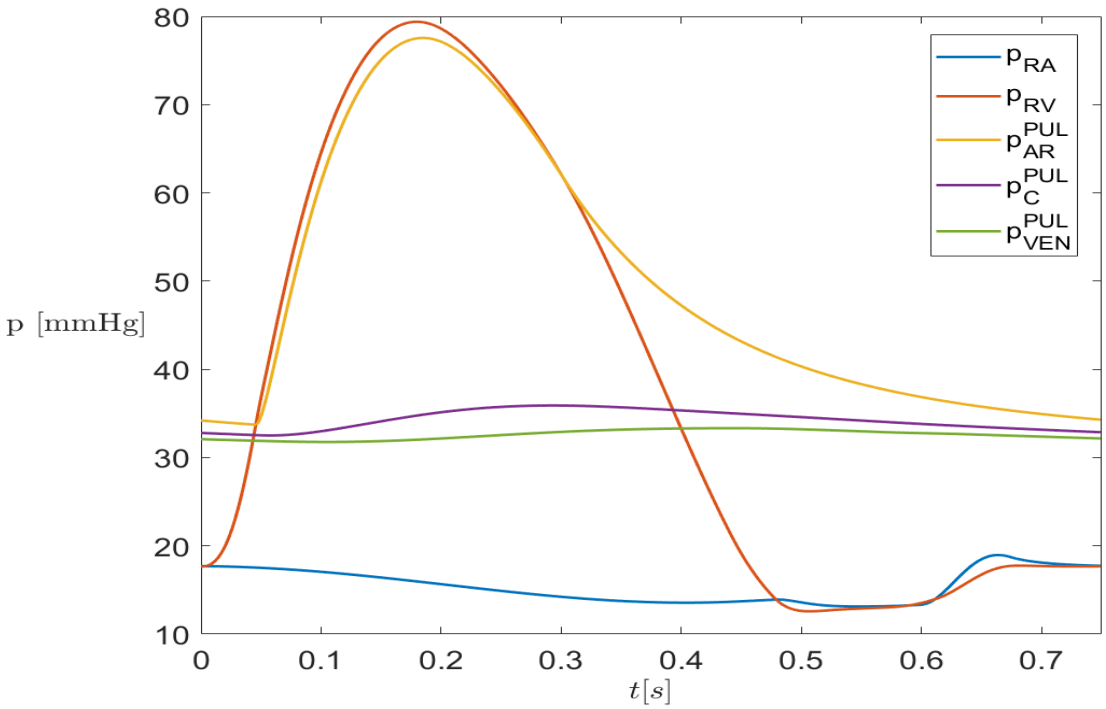

Figure 4.24: VSD/VD patient pulmonary pressures.

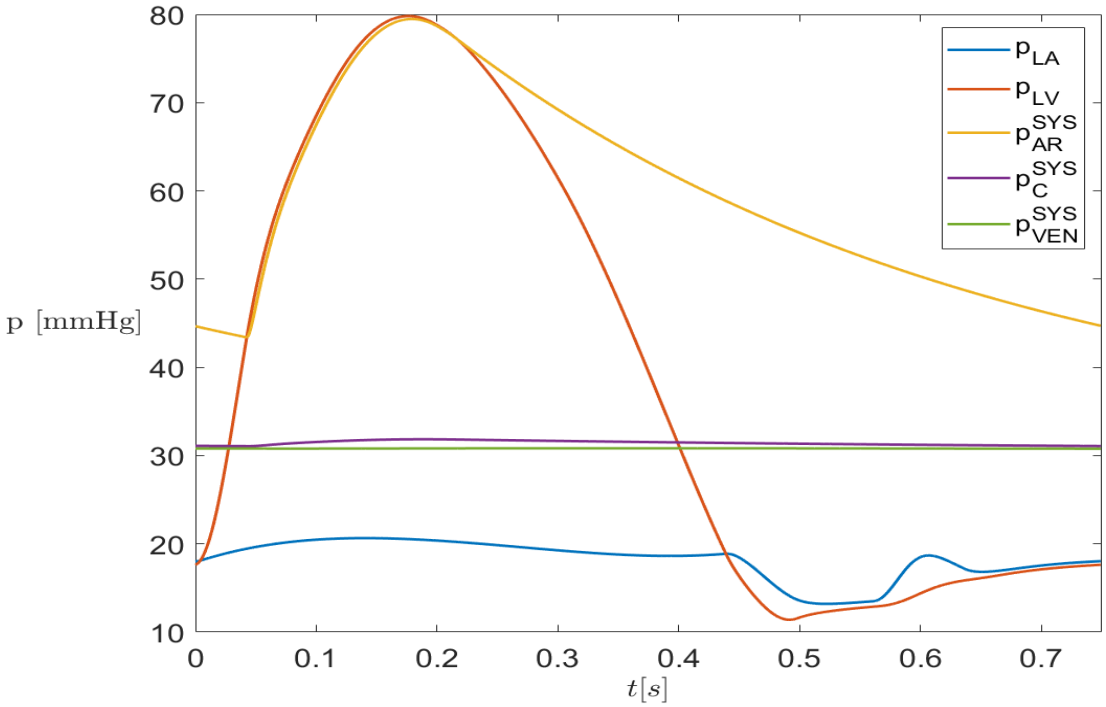

Figure 4.25: VSD/VD patient systemic pressures.

4.7. ASD/VSD patient

In this subsection we review the results of the model calibration for the ASD/VSD patient. The obtained calibrated model for the ASD/VSD patient has a mean squared relative error of 4.81×10^{-2}. As in the VSD calibration the model correctly estimate almost all the pressure except the mean pulmonary wedge pressure, which is clearly overestimated. In this case the right atrial mean pressure is also overestimated. The model also fails to correctly estimate the blood flows of the pulmonary and systemic circulation ,Table 4.11.

Again, as in the VSD patient, it can be inferred from the measured PVR and from the calibrated pulmonary resistances that the patient has significant damage to the pulmonary circulation vessels.

C_{AR}^{PUL} is again severely decreased, following the VSD patient reasoning, it can explain the difference of 50 $mmHg$ between the maximum and minimum pulmonary arterial pressure. The resulting septal defects resistances are $R_{ASD} = 0.052\ mmHg\ s\ ml^{-1}$ and $R_{ASD} = 0.0011\ mmHg\ s\ ml^{-1}$. The ventricular pressure almost match, whereas the atrial one slightly differ. The ventricles work together as a common chamber receiving blood from the atria and pumping it into the systemic and pulmonary circulation. The right atrial pressure exceeds the left one, probably as a consequence of the incorrect estimation by the model of the circulation flows. Indeed, an higher systemic circulation implies more blood going to the right atrium, increasing, as a consequence, its pressure.

Acronym	*Clinical value*	*Model output*	*Units of measure*
p_{RA}^{mean}	13	19.23	$mmHg$
p_{RV}^{max}	100	110.24	$mmHg$
p_{RV}^{min}	12	12.37	$mmHg$
PAP_{max}	99	109.00	$mmHg$
PAP_{min}	49	48.85	$mmHg$
PAP_{mean}	70	74.86	$mmHg$
PWP_{mean}	11	22	$mmHg$
p_{LV}^{max}	117	106.85	$mmHg$
p_{LV}^{min}	7	7.92	$mmHg$
SAP_{max}	102	105.16	$mmHg$
SAP_{min}	72	71.53	$mmHg$
SAP_{mean}	86	88.39	$mmHg$
Q_P	5.48	3.50	$l \times min^{-1}$
Q_S	5.48	6.13	$l \times min^{-1}$

Table 4.11: Output comparison for ASD/VSD model calibration

Table 4.12: ASD/VSD patient: model parameters significant changes

Acronym	*Healty reference*	*ASD/VSD patient*	*Units of measure*
R_{AR}^{PUL}	0.0714	0.351	$mmHg\ s\ ml^{-1}$
R_{VEN}^{PUL}	0.0375	0.05	$mmHg\ s\ ml^{-1}$
C_{AR}^{PUL}	6.004	0.586	$ml\ mmHg^{-1}$
R_{VEN}^{SYS}	0.3596	0.081	$ml\ mmHg^{-1}$
E_{LV}^{A}	2.70	9.29	ml^{-1}
E_{LV}^{B}	0.069	0.121	ml^{-1}
E_{RV}^{A}	0.43	2.78	ml^{-1}
E_{RV}^{B}	0.041	0.375	ml^{-1}

The elastance parameters all increased several times.
It is unclear if this is a consequence of the body remodelling caused by the abnormal cardiac circulation over the years or if it is a shortcut the calibration process used to correctly predict the maximal ventricular pressures. Indeed, both maximal ventricular pressures of the patient are considerably high, even more if considering that the pressure match achieved should have lowered the maximal left ventricular pressure.
This pressure however is still perfectly in the healthy range (90-140 $mmHg$) for both VSD

and ASD/VSD patients.

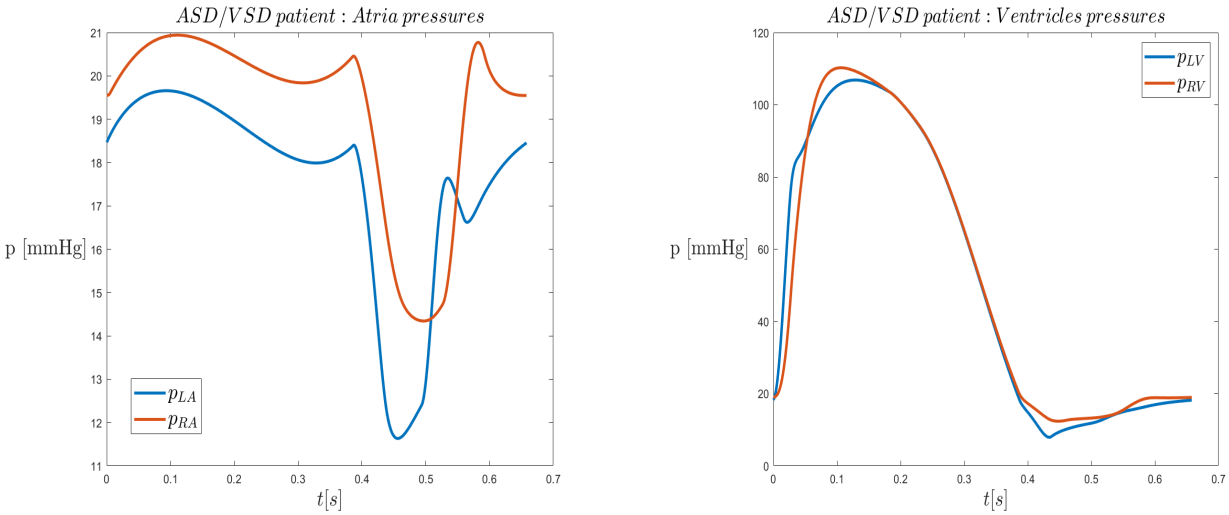

(a) (b)

Figure 4.26: ASD/VSD patient chamber pressures: (a) atrial pressures; (b)ventricular pressures

In the right ventricular pressure-volume loop it can be clearly noted how the normally straight isovolumetric contraction is curved by the blood influx from the left ventricle.

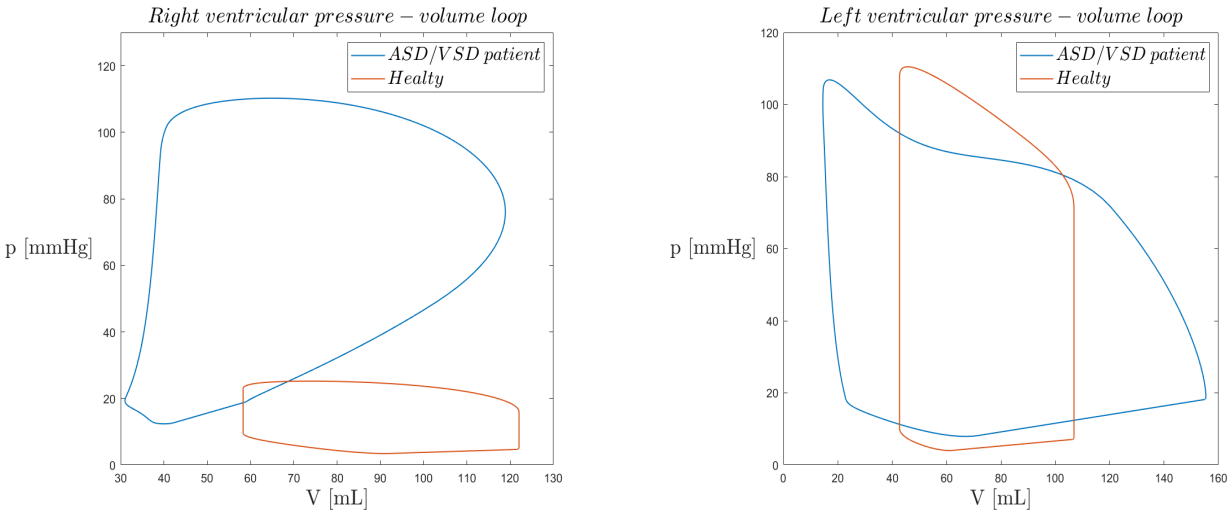

(a) (b)

Figure 4.27: ASD/VSD patient ventricular P-V loops: (a) Right ventricle; (b) Left ventricle

As in the VSD patient the right ventricular end diastolic volume doesn't exceed the healthy one. Again the additional blood influx increase the right ventricular pressure, opening earlier the pulmonary valve and discharging a considerable blood flow in the pulmonary trunk.

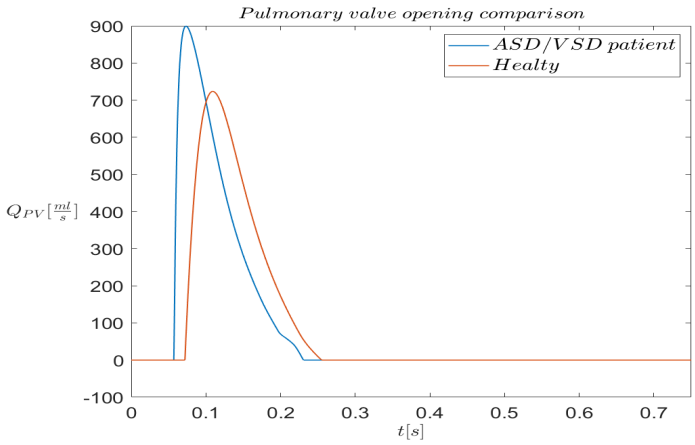

Figure 4.28: Flow through pulmonary valve comparison between ASD/VSD patient and healthy reference patient

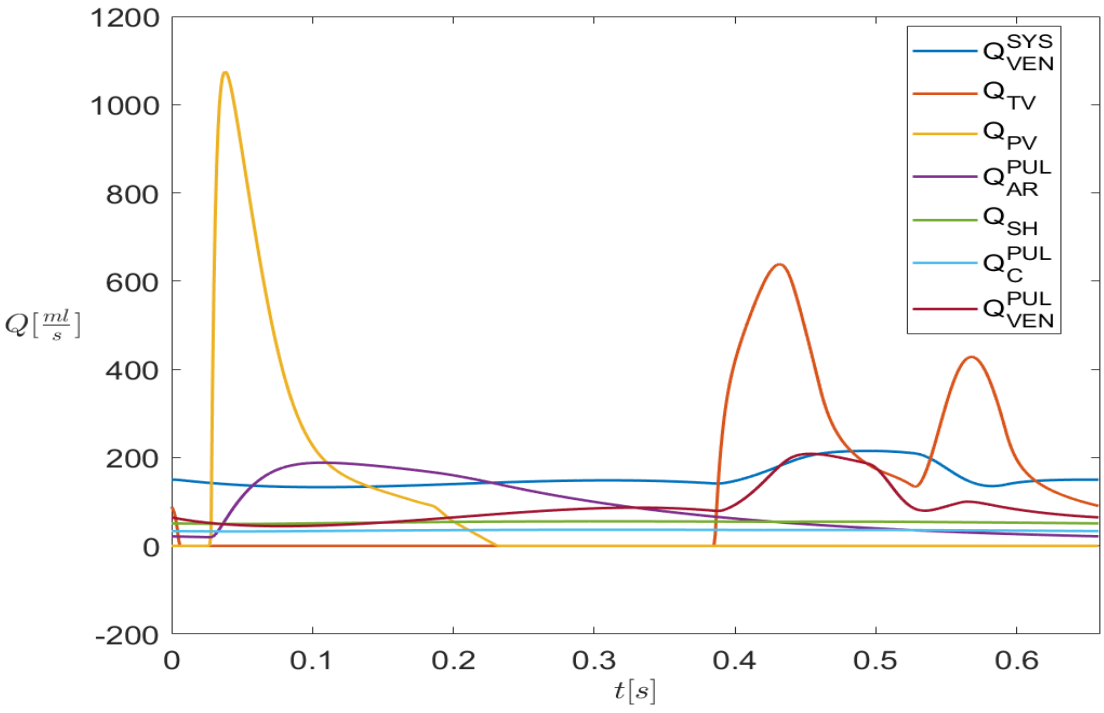

Figure 4.29: ASD/VSD patient pulmonary flows.

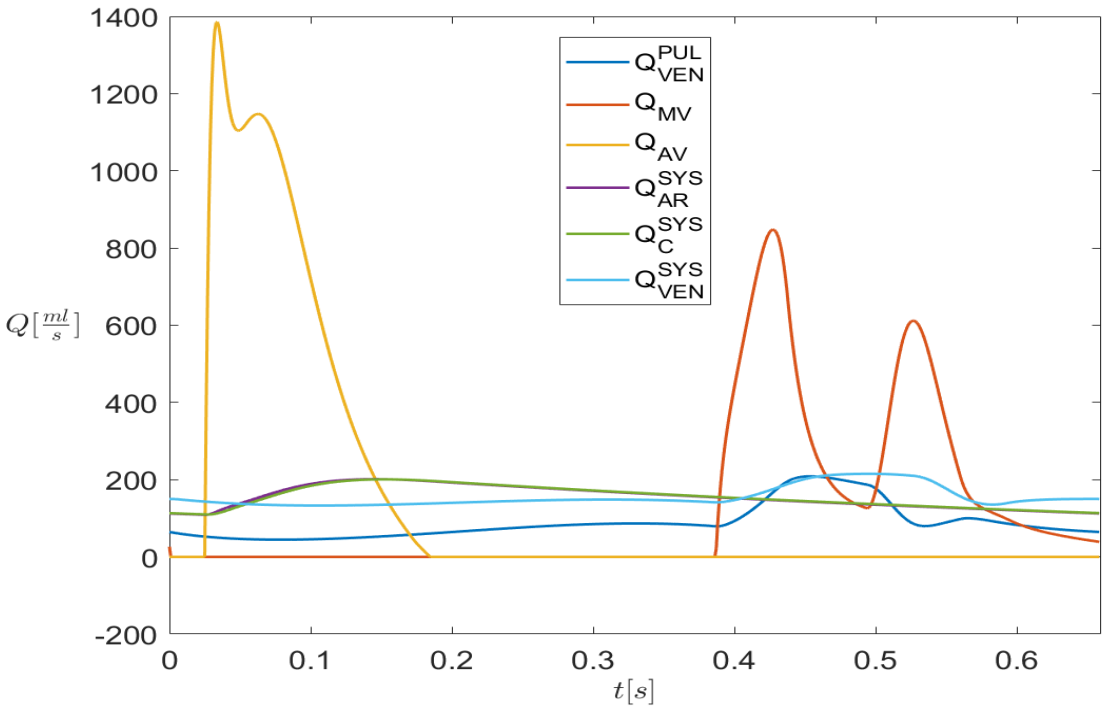

Figure 4.30: ASD/VSD patient systemic flows.

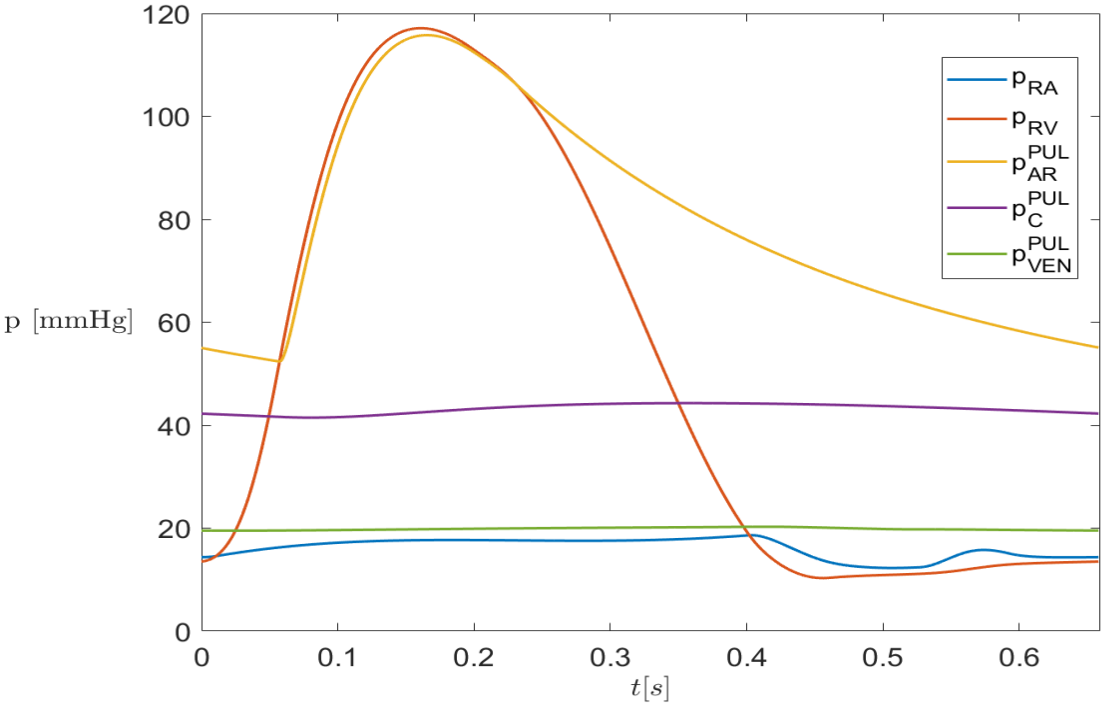

Figure 4.31: ASD/VSD patient pulmonary pressures.

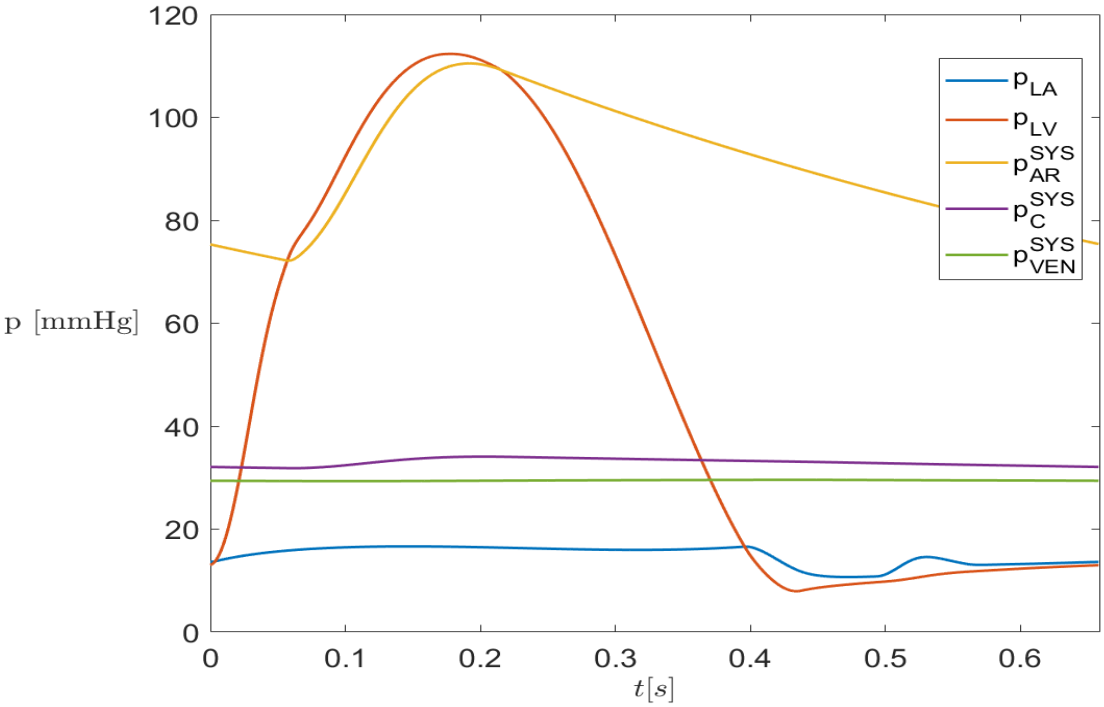

Figure 4.32: ASD/VSD patient systemic pressures.

5 | Conclusions and future developments

We implemented a model for the patent foramen ovale which correctly predicts the increasing shunt behaviour for larger orifice radius.
The predicted shunt ratios are considerably close to the healthy reference value of 1, in which systemic and pulmonary circulation are perfectly balanced, suggesting a low impact on the cardiocirculatory system.
In agreement with this result is the fact that a quarter of the world population present this condition and seem unaffected in their daily lives.
As mentioned in the Section 1.2 the problems associated with this defect instead stem from the potential for paradoxical emboli to pass through it, thereby risking occlusion of systemic vessels and giving rise to a series of consequences.
Considering the numerous patients affected by this disease, this model can be associated with the available data to improve the knowledge and data quality provided to a machine learning model, studying the patent foramen ovale, during its training phase.

For the PAPVR, the implemented model correctly estimates the increasing shunt ratios by increasing the anomalous veins number and correctly see a shunt phenomenon decrease by considering attachment spot (such as the superior vena cava) placed upstream with respect to the right atrium.
However, the model appears static, not allowing for other types of PAPVR or specific considerations regarding the individual case, such as the exact point of anomalous connection in the vessel or the type of connection itself. The model could be improved by a more thorough division of the pulmonary and systemic venous systems. This could involve considering the anatomical differences among the pulmonary veins, acknowledging their varying origin pressures due to the respective lungs they drain, and ultimately introducing more possibilities for anomalous connections, such as the brachiocephalic veins or the azygos vein.

Calibrating the model that incorporates the septal defects resistances, allows for a fairly accurate reproduction of the patient's cardiovascular system under treatment. Indeed the computed mean relative squared errors for the different patients are considerably small. This enables important estimations and considerations about their clinical conditions without resorting to highly invasive measurements. In particular, from the obtained resistances and capacitances we identified a significant damage on the pulmonary vessels in the two patients with the ventricular septal defect.

However, the drawback of this implementation is the extremely lengthy calibration process (approx. 20 days), which is not compatible with the promptness and speed required in treating a patient. The calibration process took a considerable amount of time because the parameters can vary significantly, even by orders of magnitude, effectively enlarging the domain in which the method seeks a solution.

A potential future development is the integration of a software or a trained machine learning model into this calibration process. By taking the patient's clinical data as input, this software/model could automatically provide a better initial guess for the calibration process. By studying the clinical data, as discussed retrospectively for the maximal and minimal pulmonary pressure in the Sections 4.4, 4.5, 4.6, 4.7, it becomes possible to investigate the patient's physical condition and, consequently, gather prior information about their related lumped parameters.

From the mathematical point of view, this procedure would make the starting point of the loss function closer to the relevant minima, consequently speeding up the calibration process and potentially making the minimization method avoid other incorrect local minima, now further away from the starting point

Bibliography

[1] P. J. Blanco and R. A. Feijóo, "A 3d-1d-0d computational model for the entire cardiovascular system," *Mecánica Computacional*, vol. 29, no. 59, pp. 5887–5911, 2010.

[2] M. Hirschvogel, M. Bassilious, L. Jagschies, S. M. Wildhirt, and M. W. Gee, "A monolithic 3d-0d coupled closed-loop model of the heart and the vascular system: experiment-based parameter estimation for patient-specific cardiac mechanics," *International journal for numerical methods in biomedical engineering*, vol. 33, no. 8, p. e2842, 2017.

[3] F. Regazzoni, M. Salvador, P. C. Africa, M. Fedele, L. Dedè, and A. Quarteroni, "A cardiac electromechanical model coupled with a lumped-parameter model for closed-loop blood circulation," *Journal of Computational Physics*, vol. 457, p. 111083, 2022.

[4] J. Mynard, M. Davidson, D. Penny, and J. Smolich, "A simple, versatile valve model for use in lumped parameter and one-dimensional cardiovascular models," *International Journal for Numerical Methods in Biomedical Engineering*, vol. 28, no. 6-7, pp. 626–641, 2012.

[5] X. Zhang, H. Haneishi, and H. Liu, "Impact of ductus arteriosus constriction and restrictive foramen ovale on global hemodynamics for term fetuses with d-tga," *International Journal for Numerical Methods in Biomedical Engineering*, vol. 37, no. 11, p. e3231, 2021.

[6] C. F. Babbs, J. C. Weaver, S. H. Ralston, and L. A. Geddes, "Cardiac, thoracic, and abdominal pump mechanisms in cardiopulmonary resuscitation: studies in an electrical model of the circulation," *The American journal of emergency medicine*, vol. 2, no. 4, pp. 299–308, 1984.

[7] A. Di Molfetta, G. Ferrari, R. Iacobelli, S. Filippelli, L. Fresiello, P. Guccione, A. Toscano, and A. Amodeo, "Application of a lumped parameter model to study the feasibility of simultaneous implantation of a continuous flow ventricular assist device (vad) and a pulsatile flow vad in bivad patients," *Artificial organs*, vol. 41, no. 3, pp. 242–252, 2017.

[8] H. Tang, Z. Dai, M. Wang, B. Guo, S. Wang, J. Wen, and T. Li, "Lumped-parameter circuit platform for simulating typical cases of pulmonary hypertensions from point of hemodynamics," *Journal of cardiovascular translational research*, vol. 13, pp. 826–852, 2020.

[9] M. Korurek, M. Yildiz, A. Yüksel, and A. Şahin, "Simulation of eisenmenger syndrome with ventricular septal defect using equivalent electronic system," *Cardiology in the Young*, vol. 22, no. 3, pp. 301–306, 2012.

[10] S. Shimizu, D. Une, T. Shishido, A. Kamiya, T. Kawada, S. Sano, and M. Sugimachi, "Norwood procedure with non-valved right ventricle to pulmonary artery shunt improves ventricular energetics despite the presence of diastolic regurgitation: a theoretical analysis," *The journal of physiological sciences*, vol. 61, pp. 457–465, 2011.

[11] A. Jalali, G. F. Jones, D. J. Licht, C. Nataraj, *et al.*, "Application of mathematical modeling for simulation and analysis of hypoplastic left heart syndrome (hlhs) in pre-and postsurgery conditions," *BioMed research international*, vol. 2015, 2015.

[12] Wikipedia, "Conduction system of the hear." https://commons.wikimedia.org/w/index.php?curid=10197958.

[13] Wikipedia, "Diagram of the human heart." https://commons.wikimedia.org/w/index.php?curid=830253.

[14] Wikipedia, "Phases of the cardiac cycle." https://commons.wikimedia.org/w/index.php?curid=30148227.

[15] C. Contaldi, M.-A. Losi, A. Rapacciuolo, M. Prastaro, R. Lombardi, V. Parisi, L. S. Parrella, C. Di Nardo, A. Giamundo, R. Puglia, *et al.*, "Percutaneous treatment of patients with heart diseases: selection, guidance and follow-up. a review," *Cardiovascular ultrasound*, vol. 10, no. 1, pp. 1–18, 2012.

[16] L. Guo, "Partial anomalous pulmonary venous return." https://www.osmosis.org/answers/interventricular-septum.

[17] E. J. Schroeckenstein RF, Wasenda GJ, "Valvular competent patent foramen ovale in adults.," *Minn Med.*, vol. 55, p. 11–13, 1972 Jan.

[18] R. Clarke, L. Daly, K. Robinson, E. Naughten, S. Cahalane, B. Fowler, and I. Graham, "Hyperhomocysteinemia: an independent risk factor for vascular disease," *New england journal of medicine*, vol. 324, no. 17, pp. 1149–1155, 1991.

[19] B. Miranda, A. C. Fonseca, and J. M. Ferro, "Patent foramen ovale and stroke," *Journal of Neurology*, vol. 265, pp. 1943–1949, 2018.

[20] A. Selzer and W. H. Carnes, "The role of pulmonary stenosis in the production of chronic cyanosis," *American Heart Journal*, vol. 45, no. 3, pp. 382–395, 1953.

[21] G. Kronik and H. Mösslacher, "Positive contrast echocardiography in patients with patent foramen ovale and normal right heart hemodynamics," *The American Journal of Cardiology*, vol. 49, no. 7, pp. 1806–1809, 1982.

[22] A. A. Alsheikh-Ali, D. E. Thaler, and D. M. Kent, "Patent foramen ovale in cryptogenic stroke: incidental or pathogenic?," *Stroke*, vol. 40, no. 7, pp. 2349–2355, 2009.

[23] H. Hara, T. K. Jones, E. R. Ladich, R. Virmani, D. C. Auth, J. E. Eichinger, R. J. Sommer, R. A. Van Tassel, and R. S. Schwartz, "Patent foramen ovale closure by radiofrequency thermal coaptation: first experience in the porcine model and healing mechanisms over time," *Circulation*, vol. 116, no. 6, pp. 648–653, 2007.

[24] H. Healtcare, "Patent foramen ovale." https://hartfordhealthcare.org/services/heart-vascular/departments/structural-heart-disease-program/patent-foramen-ovale.

[25] C. point foundation, "Partial anomalous pulmonary venous return." http://www.pted.org/id=papvr.

[26] B. F. Laya, M. J. Goske, S. Morrison, J. R. Reid, L. Swischuck, E. H. Ey, D. J. Murphy, M. Lieber, and N. Obuchowski, *The accuracy of chest radiographs in the detection of congenital heart disease and in the diagnosis of specific congenital cardiac lesions*, vol. 36. Springer, 2006.

[27] P. M. Steele, V. Fuster, M. Cohen, D. Ritter, and D. McGoon, "Isolated atrial septal defect with pulmonary vascular obstructive disease–long-term follow-up and prediction of outcome after surgical correction.," *Circulation*, vol. 76, no. 5, pp. 1037–1042, 1987.

[28] N. C. on Birth Defects, C. f. D. C. Developmental Disabilities, and Prevention., "Facts about atrial septal defect." https://www.cdc.gov/ncbddd/heartdefects/atrialseptaldefect.html.

[29] D. E. Spicer, H. H. Hsu, J. Co-Vu, R. H. Anderson, and F. J. Fricker, "Ventricular septal defect," *Orphanet journal of rare diseases*, vol. 9, no. 1, pp. 1–16, 2014.

[30] N. C. on Birth Defects, C. f. D. C. Developmental Disabilities, and Prevention., "Facts about ventricular septal defect." https://www.cdc.gov/ncbddd/heartdefects/ventricularseptaldefect.html.

[31] A. Tonini, C. Vergara, F. Regazzoni, L. Dede, R. Scrofani, C. Cogliati, and A. Quarteroni, "A mathematical model to assess the effects of covid-19 on the cardiocirculatory system," 2023.

[32] K. Sunagawa, K. Sagawa, and W. L. Maughan, "Ventricular interaction with the loading system," *Annals of biomedical engineering*, vol. 12, pp. 163–189, 1984.

[33] L. F. Shampine and M. W. Reichelt, "The matlab ode suite," *SIAM journal on scientific computing*, vol. 18, no. 1, pp. 1–22, 1997.

[34] R. H. Byrd, P. Lu, J. Nocedal, and C. Zhu, "A limited memory algorithm for bound constrained optimization," *SIAM Journal on scientific computing*, vol. 16, no. 5, pp. 1190–1208, 1995.

[35] Y. Sun, B. Sjoberg, P. Ask, D. Loyd, and B. Wranne, "Mathematical model that characterizes transmitral and pulmonary venous flow velocity patterns," *American Journal of Physiology-Heart and Circulatory Physiology*, vol. 268, no. 1, pp. H476–H489, 1995.

[36] C. Lee and L. Talbot, "A fluid-mechanical study of the closure of heart valves," *Journal of Fluid Mechanics*, vol. 91, no. 1, pp. 41–63, 1979.

[37] F. Wippermann, "On the fluid dynamics of the aortic valve," *Journal of Fluid Mechanics*, vol. 159, pp. 487–501, 1985.

[38] A. P. Yoganathan, Z. He, and S. Casey Jones, "Fluid mechanics of heart valves," *Annu. Rev. Biomed. Eng.*, vol. 6, pp. 331–362, 2004.

[39] G. Falanga, S. Carerj, G. Oreto, B. K. Khandheria, and C. Zito, "How to understand patent foramen ovale clinical significance: Part i," *Journal of Cardiovascular Echography*, vol. 24, no. 4, p. 114, 2014.

[40] V. C. Rideout, "Mathematical and computer modeling of physiological systems," 1991.

List of Figures

List of Tables

Acknowledgements

I want to sincerely express my gratitude to my Advisor Luca Dedè for the gratifying and stimulating opportunity to work with him on this thesis project. Your encouragement was of upmost importance in completing this work in time. That "keep on going like this, Giulio" message was perhaps the only moment when i felt truly gratified for my efforts by the university environment.

I would also like to deeply thanks my Co-advisor Andrea Tonini, your assistance, promptness, and invaluable advice have been indispensable throughout the working process. Your willingness to help, even during evenings and weekends, was really appreciated. Thank you so much.

Lastly, I would also like to express my gratitude to my co-advisor, Paolo Ferrero, who took time out of its schedule, shortly after the birth of a child, to assist me and provide insightful tips.